E.O. Paton Electric Welding Institute of the National Academy of Sciences of Ukraine

International Scientific-Technical and Production Journal

The Paton WELDING JOURNAL

January 2016
No. 1

Published since 2000

English translation of the monthly «Avtomaticheskaya Svarka» (Automatic Welding) journal published in Russian since 1948

Founders
E.O. Paton Electric Welding Institute, NASU
International Association «Welding»

Publisher
International Association «Welding»

Translators
A.A. Fomin, O.S. Kurochko, I.N. Kutianova
Editor
N.A. Dmitrieva
Electron galley
D.I. Sereda, T.Yu. Snegiryova

Address
E.O. Paton Electric Welding Institute,
International Association «Welding»
11 Kazimir Malevich Str. (former Bozhenko Str.),
03680, Kiev, Ukraine
Tel.: (38044) 200 60 16, 200 82 77
Fax: (38044) 200 82 77, 200 81 45
E-mail: journal@paton.kiev.ua
www.patonpublishinghouse.com

State Registration Certificate
KV 4790 of 09.01.2001
ISSN 0957-798X

Subscriptions
$348, 12 issues per year,
air postage and packaging included.
Back issues available.

CONTENTS

SCIENTIFIC AND TECHNICAL

INDUSTRIAL

INFORMATION

CHARACTERISTICS OF NON-EQUILIBRIUM ARC PLASMA IN PLASMATRON NOZZLE CHANNEL

A.V. IGNATOV[1, 2]**, I.V. KRIVTSUN**[1] and **I.L. SEMENOV**[3]
[1]Guangdong General Research Institute of Industrial Technology
(Guangzhou Research Institute of Non-Ferrous Metals), Guangzhou, PRC
[2]E.O. Paton Electric Welding Institute, NASU
11 Kazimir Malevich Str., 03680, Kiev, Ukraine. E-mail: office@paton.kiev.ua
[3]German Aerospace Center (DLR)
Munich, Germany. E-mail: igor_semenov@list.ru

A mathematical model was developed for processes of energy, pulse, mass and discharge transfer in non-equilibrium plasma of electric arc, burning in cylindrical channel with water-cooled walls being blown out by laminar flow of plasma inert gas. The model is based on multi-fluid equations for nonisothermal, ionization non-equilibrium arc plasma, considering double ionization of atoms of the plasma gas written in a drift-diffusion approximation. Such an approach allows uniform description of the processes taking place in central region of the channel (in arc column plasma) as well as near-wall region (in plasma ionization layer) up to interface of space charge layer directly adjacent to channel wall. Consideration of the processes taking place in collisionless layer of space discharge and determination of characteristics of thermal and electric interaction of arc plasma with channel wall is carried out using corresponding boundary conditions on interface of the indicated layer. Besides, if presence of doubly charged ions in arc plasma is taken into account, it is possible to calculate its characteristics in a wide range of values of arc current and channel radius. Numerical solution of equations of the proposed model is carried out by finite volume method. Corresponding software is developed for computer realization. Detailed numerical analysis is given to radial distribution of characteristics of argon arc plasma in the cylindrical channels of direct plasmatron nozzle as well as intensity of longitudinal electric field in arc plasma and heat flow from plasma to channel wall at different values of arc current, channel radius and consumption of plasma gas. It is shown that in contrast to the central regions of the channel, where arc plasma is virtually equilibrium, a significant thermal and ionization non-equilibrium of plasma is realized in the near-wall region. It is also shown that increase of arc current and reduction of channel radius requires consideration of the doubly charge ions present in arc plasma. Comparison of results of modelling of characteristics of the non-equilibrium argon arc plasma in the plasmatron nozzle channel with available experimental data was carried out. 11 Ref., 1 Table, 9 Figures.

Keywords: *arc plasmatron, plasma-shaping channel, electric arc in channel, non-equilibrium plasma, mathematical modelling*

Development of new and improvement of existing plasma technologies, such, for example, as plasma welding, cutting, powder surfacing and coating deposition require reliable information on integral and distributed characteristics of plasma, generated by direct and indirect arc plasmatrons depending on type and structural peculiarities of the plasmatron, mode of its operation and composition of plasma gas. Thermal, gas-dynamic and electromagnetic characteristics of arc plasma flow, generated by such devices, are mainly determined by its interaction with a wall of plasmatron plasma-shaping channel. Besides, specified interaction determines the characteristics of heat and electric effect of arc plasma on the channel wall. They allow optimizing plasmatron design and increase its operation life. Experimental determination of the characteristics of arc plasma in the plasmatron channel as well as characteristics of its interaction with the channel wall is complicated due to small geometrical dimensions of the channel, high values of plasma and wall temperature.

Therefore, aim of the present work is a development of mathematical model and accurate numerical research of the processes of energy, pulse, mass and discharge transfer in non-equilibrium plasma of electric arc, burning in plasmatron cylindrical channel, as well as determination of heat and electric characteristics of its interaction with the channel wall.

The model based on multi-fluid equations for thermal and ionization non-equilibrium plasma [1] can be used for theoretical description of the processes of energy, mass and electric transfer in arc plasma volume, containing electrons, ions and neutral atoms. An approach, similar to one proposed in works [2–6] for investigation of cathode and anode processes in the electric arc, including with doubly and triply charged ions, can be used for consideration of the processes of interaction of such a plasma with the channel wall.

Corresponding approaches were earlier used for numerical analysis of distributed characteristics of arc plasma in nozzle channel of the direct plasmatron [7, 8]. However, used in these works channel wall boundary conditions were model ones without consideration of real structure of plasma near-wall region. It did not allow adequate description of the processes of heat and electric interaction of arc plasma with the channel wall. It should be noted that work [8] is one of the several publications, where the results of measurements of concentration distribution and electrons temperature as well as intensity of electric field for arc plasma in channel at different current values are provided together with calculation data.

Problem statement and applied approximations. Let's consider plasma of a stationary electric arc in asymptotic region [7] of extended (segmented) cylindrical channel of radius R, blown out by lamellar flow of inert gas at volume velocity G (under normal conditions). Arc current is denoted as I, gas pressure in studied region of the channel p is atmospheric, temperature of water-cooled (non-evaporating) channel wall is termed T_w. Assuming that given plasma system is an axisymmetric, we are going to use a cylindrical system of coordinates (r, z), axis OZ of which matches with the channel axis and directed as shown in Figure 1. It is supposed under these conditions that plasma gas moves along the indicated axis and electric current has an opposite direction.

Studied arc plasma can be conventionally divided on three regions [3]. The first of them is a layer of space charge directly attached to the channel wall (see Figure 1), where condition of quasineutral plasma is violated and significant part of potential drop between arc column plasma and channel surface is formed. This layer can be considered as collisionless, since thickness of this layer $R - r_s$, being comparable with Debye radius $r_D \sim 10^{-8} - 10^{-7}$ m, is significantly less than typical lengths of free path of plasma particle $l \sim 10^{-6} - 10^{-4}$ m under atmospheric pressure and typical values of temperature of arc plasma electrons $T_e \sim 1.5$ eV [8] (corresponding typical lengths for argon plasma of atmospheric pressure are given in Figure 2).

The second region (see Figure 1) is an ionization region of nonisothermal quasineutral plasma (pre-layer), where generation of charged particles takes place due to ionizing by plasma electrons of atoms of plasma gas being desorbed from the channel wall. Ions formed here are accelerated aside to the wall by electric field created by more movable electrons, and being recombinated on its surface. Thus, conditions of local ionization equilibrium are violated in the pre-layer limits. Besides, the rest of potential drop between arc column and channel wall is formed here, which can exceed corresponding drop in the space charge layer.

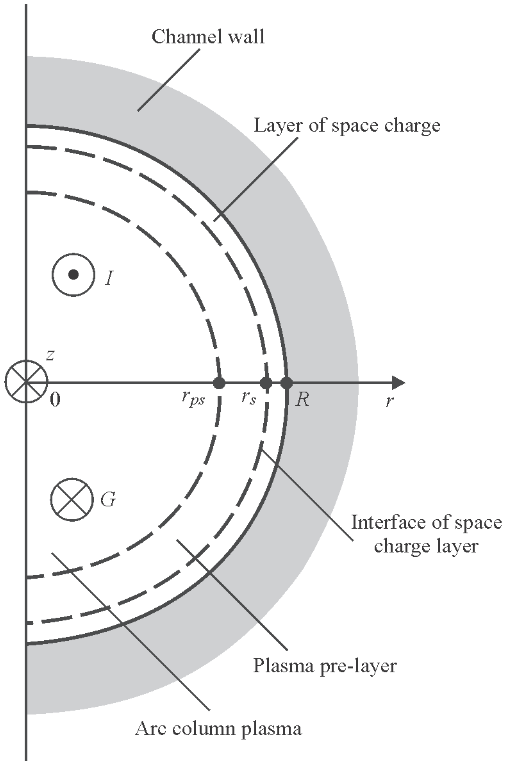

Figure 1. Scheme of arc plasma in plasmatron nozzle channel

Ionization region interface goes at $R - r_{ps}$ distance from the wall, being equal several length of free path of plasma particles. It will be matched with outer interface of plasma near-wall layer, and from it the third zone, namely arc column, will originate (see Figure 1). It is the zone, where local thermodynamic, including ionization, equilibrium takes place.

Due to the fact that present work studies arc plasma in asymptotic region of the channel, the description of processes of energy, mass and electric transfer in such a system will neglect the changes of plasma characteristics in axial direction (along the channel axis) in comparison with their radial changes. Also, taking into account the fact that studied arc is stationary, the changes of characteristics of arc plasma

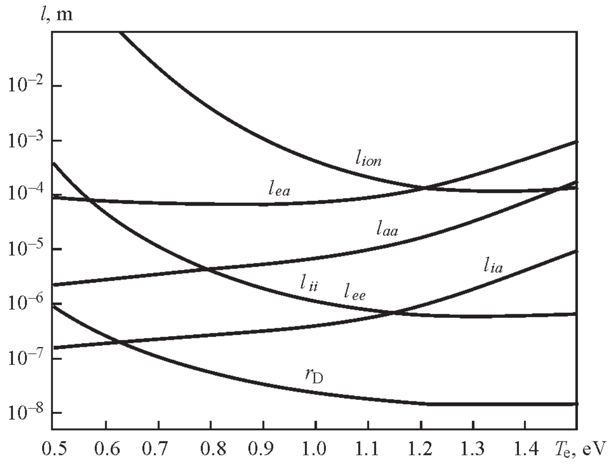

Figure 2. Typical lengths of free path of particles in atmospheric pressure argon plasma

in time are neglected likewise. These speculations allow considering that axial component of electric field and axial gradient of plasma pressure are constant on channel section, and electric current on channel wall equals zero. A model of nonisothermal (two-temperature) ionization non-equilibrium plasma, including double ionization of atoms of the plasma gas (four-component plasma), is used in writing of the multi-fluid equations for the column and ionization region of arc plasma in the channel. The equitations of movement of plasma components in radial direction are written in a drift-diffusion approximation [5] and equality of axial velocities of heavy components is supposed in writing of corresponding equations in axial direction. Consideration of the processes taking place, the space charge layer and determination of characteristics of heat and electric interaction of arc plasma with channel wall is carried out by means of application of corresponding boundary conditions on this layer interface [3].

Mathematical model. *Basic equations.* For analysis of the physical processes, taking place in the studied plasma system, it is assumed that arc plasma is characterized by the following parameters: n_e is the electrons concentration; n_n, n_i, n_{i++} are the concentration of atoms of singly and doubly charged ions of the plasma gas, respectively; v_e^r, v_n^z are the radial and axial components of electrons velocity; v_n^r, v_n^z v_{i+}^r, v_{i+}^z, v_{i++}^r, v_{i++}^z are the radial and axial components of velocities of atoms and corresponding ions; T_e is the temperature of electrons; T_h is the temperature of heavy particles of plasma, being supposed similar for atoms and ions, but different from T_e. Then set of equations, describing stationary processes of mass, pulse and energy transfer in column plasma and ionization arc layer in asymptotic region of the cylindrical channel, can be written in the following way:

- Continuity equation for electrons, atoms, singly and doubly charged ions of arc plasma taking into account non-equilibrium ionization:

$$\frac{1}{r}\frac{\partial}{\partial r}\left(rn_e v_e^r\right) = k_{i0}n_n n_e - k_{r0}n_e^2 n_{i+} + \\ + k_{i1}n_{i+}n_e - k_{r1}n_e^2 n_{i++}; \qquad (1)$$

$$\frac{1}{r}\frac{\partial}{\partial r}\left(rn_n v_n^r\right) = -k_{i0}n_n n_e + k_{r0}n_e^2 n_{i+}; \qquad (2)$$

$$\frac{1}{r}\frac{\partial}{\partial r}\left(rn_{i+} v_{i+}^r\right) = k_{i0}n_n n_e - k_{r0}n_e^2 n_{i+} - \\ - k_{i1}n_{i+}n_e + k_{r1}n_e^2 n_{i++}; \qquad (3)$$

$$\frac{1}{r}\frac{\partial}{\partial r}\left(rn_{i++} v_{i++}^r\right) = k_{i1}n_{i+}n_e - k_{r1}n_e^2 n_{i++}, \qquad (4)$$

where $k_{i\alpha}$, $k_{r\alpha}$ are the coefficients of ionization and recombination of atoms (α = 0) and singly charged ions (α = 1) [4]. Summing equations (2)–(4) and taking into account that particles of the plasma gas, assumed as inert one, do not accumulate on channel wall, the following is written:

$$n_{i+}v_{i+}^r + n_{i++}v_{i++}^r + n_n v_n^r = 0. \qquad (5)$$

Multiplying equations (1), (3) and (4) by charge of corresponding particle and summing, by considering assumption on absence of electric current on channel wall, we receive

$$j_r = en_{i+}v_{i+}^r + 2en_{i++}v_{i++}^r - en_e v_e^r = 0, \qquad (6)$$

where j_r is the radial component of current density in arc plasma; e is the electron charge. Thus, instead of equations (1)–(4) only two of them can be used by adding to them conditions (5) and (6).

Taking into account that plasma of column and ionization region of the arc is quasineutral, complete these equations by quasineutral condition, which in the case of four-component plasma is written as

$$n_e = n_{i+} + 2n_{i++}. \qquad (7)$$

Besides, let's use condition of stability of total pressure of plasma along the channel section

$$p = k\left[n_e T_e + (n_n + n_{i+} + n_{i++})T_h\right], \qquad (8)$$

where k is the Boltzmann constant;

- Equation of radial movement of electrons, atoms, singly and doubly charged ions, written in the drift-diffusion approximation (at convection members being neglected), but taking into account viscous members:

$$\frac{\partial(n_e kT_e)}{\partial r} = \frac{2}{r}\frac{\partial}{\partial r}\left(r\eta_e\frac{\partial v_e^r}{\partial r}\right) - \\ - \frac{2}{3}\frac{\partial}{\partial r}\left(\frac{\eta_e}{r}\frac{\partial(rv_e^r)}{\partial r}\right) - \\ - \frac{2\eta_e v_e^r}{r^2} + P_{en}^r + P_{ei+}^r + P_{ei++}^r - eE_r n_e; \qquad (9)$$

$$\frac{\partial(n_n kT_h)}{\partial r} = \frac{2}{r}\frac{\partial}{\partial r}\left(r\eta_n\frac{\partial v_n^r}{\partial r}\right) - \frac{2}{3}\frac{\partial}{\partial r}\left(\frac{\eta_n}{r}\frac{\partial(rv_n^r)}{\partial r}\right) - \\ - \frac{2\eta_n v_n^r}{r^2} + P_{ni+}^r + P_{ne}^r + P_{ni++}^r + R_n^r; \qquad (10)$$

$$\frac{\partial(n_{i+} kT_h)}{\partial r} = \frac{2}{r}\frac{\partial}{\partial r}\left(r\eta_{i+}\frac{\partial v_{i+}^r}{\partial r}\right) - \\ - \frac{2}{3}\frac{\partial}{\partial r}\left(\frac{\eta_{i+}}{r}\frac{\partial(rv_{i+}^r)}{\partial r}\right) - \frac{2\eta_{i+} v_{i+}^r}{r^2} + \\ + P_{i+n}^r + P_{i+e}^r + P_{i+i++}^r + R_{i+}^r - R_{i++}^r + eE_r n_{i+}; \qquad (11)$$

$$\frac{\partial(n_{i++} kT_h)}{\partial r} = \frac{2}{r}\frac{\partial}{\partial r}\left(r\eta_{i++}\frac{\partial v_{i++}^r}{\partial r}\right) - \\ - \frac{2}{3}\frac{\partial}{\partial r}\left(\frac{\eta_{i++}}{r}\frac{\partial(rv_{i++}^r)}{\partial r}\right) - \frac{2\eta_{i++} v_{i++}^r}{r^2} + \\ + P_{i++n}^r + P_{i++e}^r + P_{i++i+}^r + R_{i++}^r + 2eE_r n_{i++}; \qquad (12)$$

- Equation of electron axial movement and resulting equation of axial movement of heavy particles:

$$\frac{1}{r}\frac{\partial}{\partial r}(rm_e n_e v_e^z v_e^r)=\frac{1}{r}\frac{\partial}{\partial r}\left(r\eta_e\frac{\partial v_e^z}{\partial r}\right)+ \\ +P_{en}^z+P_{ei+}^z+P_{ei++}^z-eE_z n_e; \tag{13}$$

$$\frac{\partial\sum\limits_\alpha n_\alpha kT_\mathrm{h}}{\partial z}+\frac{1}{r}\frac{\partial}{\partial r}(r\sum_\alpha m_\alpha n_\alpha v_h^z v_\alpha^r)= \\ =\frac{1}{r}\frac{\partial}{\partial r}\left(r\sum_\alpha\eta_\alpha\frac{\partial v_h^z}{\partial r}\right)+P_{ne}^z+P_{i+e}^z+P_{i++e}^z+ \\ +eE_z(n_{i+}+2n_{i++}),\qquad \alpha=n,i+,i++. \tag{14}$$

The following designations are used in equations (9)–(14): η_α, m_α are the coefficients of dynamic viscosity and mass of particles of plasma component (α = *e*, *n*, *i*+, *i*++); $R_{\alpha\beta}^r, R_{\alpha\beta}^z$ is the radial and axial components of exchange terms ($\alpha \neq \beta$ = *e*, *n*, *i*+, *i*++) corresponding to elastic collision of particles [1]; R_α^r are the radial components of exchange terms (α = *n*, *i*+, *i*++), corresponding to inelastic collisions [1]; E_r, E_z are the radial and axial components of electric field in arc plasma;

- Movement equation shall be completed by conditions of arc total current conservation

$$I=2\pi\int_0^R|j_z|rdr, \tag{15}$$

where $j_z=en_{i+}v_{i+}^z+2en_{i++}v_{i++}^z-en_e v_e^z$ is the axial component of density of electric current in plasma as well as condition of conservation of mass consumption of plasma gas through channel cross section

$$G_M=\rho_0 G=2\pi\int_0^R r\sum_{\alpha=n,i+,i++}m_\alpha n_\alpha v_\alpha^z dr, \tag{16}$$

where ρ_0 is the density of plasma gas under normal conditions;

- Equation of electron energy transfer and total equation of energy of heavy particles are written in the following way:

$$\frac{1}{r}\frac{\partial}{\partial r}\left(v_e^r\frac{5}{2}n_e kT_\mathrm{e}\right)=\frac{1}{r}\frac{\partial}{\partial r}\left(r\lambda_e\frac{\partial T_\mathrm{e}}{\partial r}\right)+ \\ +\sum_\alpha(Q_{e\alpha}+G_{e\alpha})-e(E_z v_e^z+E_r v_e^r)n_e-Q_r, \tag{17} \\ \alpha=n,i+,i++;$$

$$\frac{1}{r}\frac{\partial}{\partial r}\sum_\alpha\left(v_\alpha^r\left(\frac{5}{2}n_\alpha kT_\mathrm{h}+\frac{1}{2}m_\alpha n_\alpha v_\alpha^2\right)\right)= \\ =\frac{1}{r}\frac{\partial}{\partial r}\left(r\sum_\alpha\lambda_\alpha\frac{\partial T_\mathrm{h}}{\partial r}\right)+\sum_\alpha Q_{\alpha e}+ \tag{18} \\ +e(E_z v_{i+}^z+E_r v_{i+}^r)n_{i+}+2e(E_z v_{i++}^z+E_r v_{i++}^r)n_{i++}, \\ \alpha=n,i+,i++.$$

where λ_α are the coefficients of heat conduction of plasma component (α = *e*, *n*, *i*+, *i*++); $Q_{\alpha\beta}$ are the exchange terms ($\alpha \neq \beta$ = *e*, *n*, *i*+, *i*++) corresponding to particle elastic collisions [1]; $Q_{e\alpha}$ are the exchange terms (α = *i*+, *i*++) corresponding to non-elastic collisions of electrons with heavy particles [1]; Q_r is the electron energy loss for heat irradiation.

Work [9] gives the formulae for calculation of coefficients of ionization and recombination, collision frequency, transportation coefficients and radiation losses of electron energy, being included in equations (1)–(4), (9)–(14), (17) and (18) for further studied atmospheric (high-pressure) plasma. Explicit form of the exchange elements, included in (9)–(14), (17) and (18), are also given there.

Boundary conditions. Taking into account used approximation on axial symmetry of studied plasma system, the following can be assumed on channel axis:

$$\left.\frac{\partial n_\alpha}{\partial r}\right|_{r=0}=0,\quad \alpha=i+,i++; \tag{19}$$

$$\left.v_\alpha^r\right|_{r=0}=0,\quad \alpha=i+,i++; \tag{20}$$

$$\left.\frac{\partial v_\alpha^z}{\partial r}\right|_{r=0}=0,\quad \alpha=n,i+,i++; \tag{21}$$

$$\left.\frac{\partial T_\mathrm{e}}{\partial r}\right|_{r=0}=\left.\frac{\partial T_\mathrm{h}}{\partial r}\right|_{r=0}=0. \tag{22}$$

In order to set boundary conditions on channel wall, to be more accurate on interface of ionization region under the layer of space charge, the following is done. Using equations (5), (6), (9)–(11), the flow of singly charged ions on indicated interface can be written in form of

$$\left.n_{i+}v_{i+}^r\right|_{r=r_s}=D_{i+i+}^T\left.\frac{\partial(T_\mathrm{e}+T_\mathrm{h})}{\partial r}\right|_{r=r_s}+ \\ +D_{i+i+}\left.\frac{\partial n_{i+}}{\partial r}\right|_{r=r_s}+D_{i+i++}^T\left.\frac{\partial(2T_\mathrm{e}+T_\mathrm{h})}{\partial r}\right|_{r=r_s}+D_{i+i++}\left.\frac{\partial n_{i++}}{\partial r}\right|_{r=r_s}, \tag{23}$$

where $D_{a\beta}$, $D_{\alpha\beta}^T$, α = *i*+, β = *i*+, *i*++ are the transportation coefficients, explicit form of which is given in appendix. At that, velocity of singly charged ions on interface of space charge layer can be taken equal to Bohm velocity, which has the following form in the case of three-component plasma [10]:

$$\left.v_{i+}^r\right|_{r=r_s}=\left.\sqrt{\frac{k(T_\mathrm{e}+T_\mathrm{h})}{m_{i+}}}\right|_{r=r_s}. \tag{24}$$

Assuming that gradient of concentration of doubly charged ions on indicated interface equals zero:

$$\left.\frac{\partial n_{i++}}{\partial r}\right|_{r=r_s}=0, \tag{25}$$

their flow can be determined, assuming, for example, the velocity of doubly charged ions on external interface of pre-layer being equal

$$\left.v_{i++}^r\right|_{r=r_s}=\left.\sqrt{\frac{k(2T_\mathrm{e}+T_\mathrm{h})}{m_{i++}}}\right|_{r=r_s},$$

that together with relationship (24) corresponds to Bohm criterion in the case of four-component plasma.

Let's write the following for axial components of velocities of plasma heavy particles close to channel wall, taking into account «adhesion» condition:

$$v_\alpha^z\Big|_{r=r_s} = 0,\ \ \alpha = n, i+, i++. \tag{27}$$

Boundary condition for electron temperature is set in from of [3]

$$\left(v_e^r \frac{5}{2} n_e k T_\mathrm{e} + \lambda_e \frac{\partial T_\mathrm{e}}{\partial r}\right)_{r=r_s} = \\ = j_e^r (2kT_\mathrm{e} + e\Delta\phi_s)\Big|_{r=r_s}, \tag{28}$$

where

$$\Delta\phi_s = -\frac{kT_\mathrm{e}}{2e}\ln\frac{2\pi m_e (T_\mathrm{e} + T_\mathrm{h})}{m_{i+} T_\mathrm{e}}\Bigg|_{r=r_s} \tag{29}$$

of potential drop in space charge layer [3]. Temperature of plasma heavy particles close to wall can be set with sufficient accuracy equal to the temperature of wall channel:

$$T_\mathrm{h}\Big|_{r=r_s} = T_\mathrm{w}. \tag{30}$$

The important characteristic of the processes of heat and electric interaction of arc plasma with plasmatron channel wall are heat flow from plasma on channel wall (see, for example [3]):

$$q_\mathrm{w} = \left\{\begin{array}{l} j_{i+}^r\left[k\left(2T_\mathrm{h} + \frac{1}{2}T_\mathrm{e}\right) + e\Delta\phi_s + E_1\right] + \\ + j_{i++}^r\left[k(2T_\mathrm{h} + T_\mathrm{e}) + 2e\Delta\phi_s + E_2\right] + \\ + 2 j_e^r k (T_\mathrm{e} - T_\mathrm{w}) \end{array}\right\}\Bigg|_{r=r_s}, \tag{31}$$

as well as potential drop between arc plasma and wall, which consists of voltage drop in column and ionization region of arc plasma as well as potential drop in space charge layer, determined by expression (29).

Described above mathematical model of the four-component plasma of electric arc in asymptotic region of plasmatron channel wall can be easily reduced for arc modelling in the channel under those modes of its arcing when formation of the doubly charged ions in arc plasma can be neglected (three-component plasma). For this, in the model equations, corresponding to boundary conditions, and expressions for determination of transportation coefficients of plasma component as well as radiation loss of electron energy, it is enough to set $n_{i++} = 0$, coefficient of ionization of singly charged ions in continuity equations equate to zero and drop the exchange terms, corresponding to collisions at participation or appearance of the doubly charged ions, in the equations of movement and energy transfer.

Procedure and algorithm of problem solving. Stationary solution (relaxation) method is used in numerical solution of the stated problem. For this reason the indicial equations (1)–(4), (9)–(14), (17), (18) are completed with corresponding non-stationary members and written in dimensionless form. The following values are taken as scales of temperature, concentration, length, velocity and time:

$$\bar{T} = 1\ \mathrm{eV};\ \bar{n} = 10^{23}\ \mathrm{m}^{-3};\ \bar{L} = 10^{-4}\ \mathrm{m};$$

$$\bar{v} = 10^3\ \mathrm{m/s};\ \bar{t} = 10^{-7}\ \mathrm{s}.$$

Obtained equations are solved numerically by finite element method. At that an implicit scheme with secondary approximation on nonlinear finite-volumetric mesh [11], taking into account linear approximation of the boundary conditions (19–28) and (30) written in dimensionless form, is used. Uniform of channel section distributions of temperature, velocities and concentrations of plasma component as well as electric field, corresponding to equations (1)–(18) at neglect of radial nonuniformity of the system, are used as initial conditions.

Computer realization of the described algorithm is carried out in two steps, namely: 1 — pre-processor, realized in software package Matlab, provides for set of system initial parameters and determination of corresponding to them characteristics of arc plasma in the nozzle channel being assumed as radially uniform, and 2 — post-processor, realized in software environment Fortran, provides for numerical solution of a set of algebraic equations approximating differential equations (3), (4), (9), (10)–(14), (17), and (18). Method of paralleling for four cores by means of program setting of corresponding part of calculation region to each core (processor) is used in computations. It significantly increases speed of numerical results obtaining.

Modelling results. The following system parameters were used for calculation of characteristics of arc plasma in the plasmatron nozzle channel: arc current I = 50, 100, 200 A; channel radius R = = 1.2 mm; volumetric consumption of plasma gas (Ar) G = 2.5 l/min; temperature of channel wall T_w = = 1160 K. Figures 3–8 show the results of calculation of radial distributions of characteristics in studied plasma.

Firstly, let's study effect of arc current and channel radius on distributions of electron temperature and temperature of plasma heavy components without notice of doubly charged ions (three-component plasma) in it. As follows from calculation results in Figure 3, the temperatures of electrons and plasma heavy particles in arc column are virtually matched, i.e. arc plasma in central region of the channel is

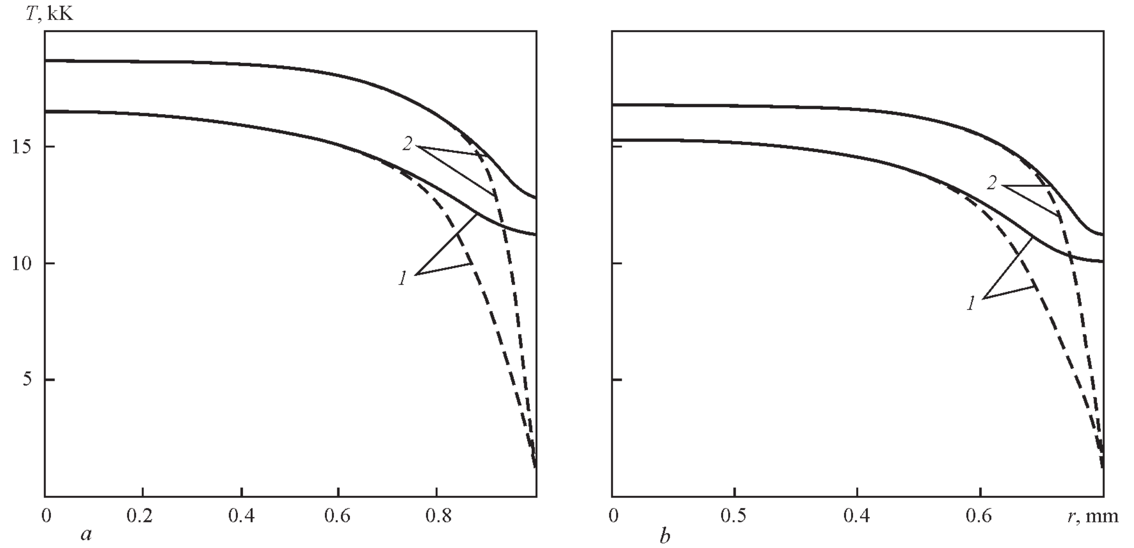

Figure 3. Radial distributions of temperature of electrons (*solid curves*) and heavy particles (*dashed*) of arc plasma in plasmatron nozzle channel: *a* — $R = 1$ mm, $G = 2$ l/min; *1* – $I = 50$ A; *2* — 100 A; *b* — $R = 2$ mm, $G = 5$ l/min; *1* — $I = 100$ A; *2* – 200 A

thermally equilibrium, besides its temperature rises at increase of arc current and decrease of channel radius (see also [7, 8]). T_e significantly exceeds T_h in the vicinity to channel wall, at that size of region of thermally non-equilibrium plasma, determining pre-layer thickness, is vice versa reduced at rise of I and decrease of R (see Figure 3). The reason for higher in comparison with T_h values of temperature of electrons in the near-wall region of arc is a reduction of efficiency of energy exchange between electron component and heavy particles, resulting in temperature equalization.

Figure 4 shows calculation distributions of level of ionization non-equilibrium of arc plasma on the channel wall, determined as $\delta = n_e / n_e^{\mathrm{Saha}}$ (where n_e^{Saha} is the equilibrium concentration of electrons, calculated based on Saha equation with electron temperature, quasilinearity condition and partial pressure law). Calculation data indicate that arc column plasma with high level of accuracy has not only thermal (see Figure 3), but also ionization equilibrium. Arc plasma in the pre-layer is significantly non-equilibrium, moreover δ value, characterizing level of non-equilibrium ionization, firstly somewhat increases and then rapidly drops as far as approaching to channel wall (concentration of electrons on interface of space charge is two-three order lower than equilibrium one). An important circumstance in this case is the fact that the regions of ionization and thermal plasma non-equilibrium are virtually matched under studied parameters of the system, and their sizes reduce with increase of I and decease of R (see Figures 3 and 4). It should be noted here that the size of region of thermal and ionization non-equilibrium of arc plasma in the plasmatron nozzle channel makes 20–35 % of R value.

Doubly charged ions, presence of which can be considered in scope of the four-component plasma

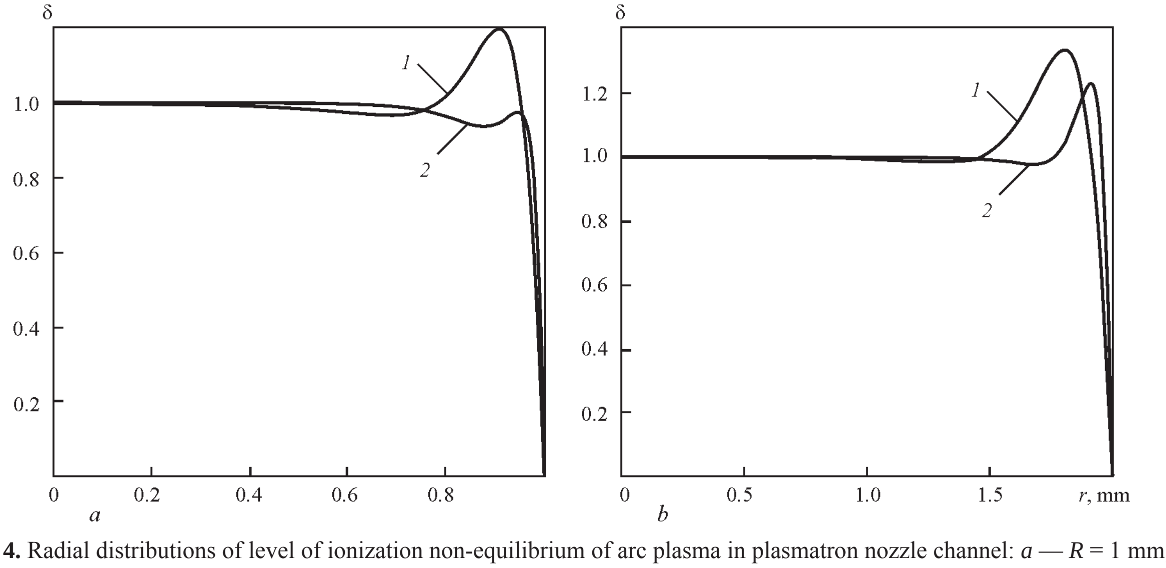

Figure 4. Radial distributions of level of ionization non-equilibrium of arc plasma in plasmatron nozzle channel: *a* — $R = 1$ mm, $G =$ = 2 l/min; *1* — $I = 50$ A; *2* — 100 A; *b* — $R = 2$ mm, $G = 5$ l/min; *1* — $I = 100$ A; *2* — 200 A

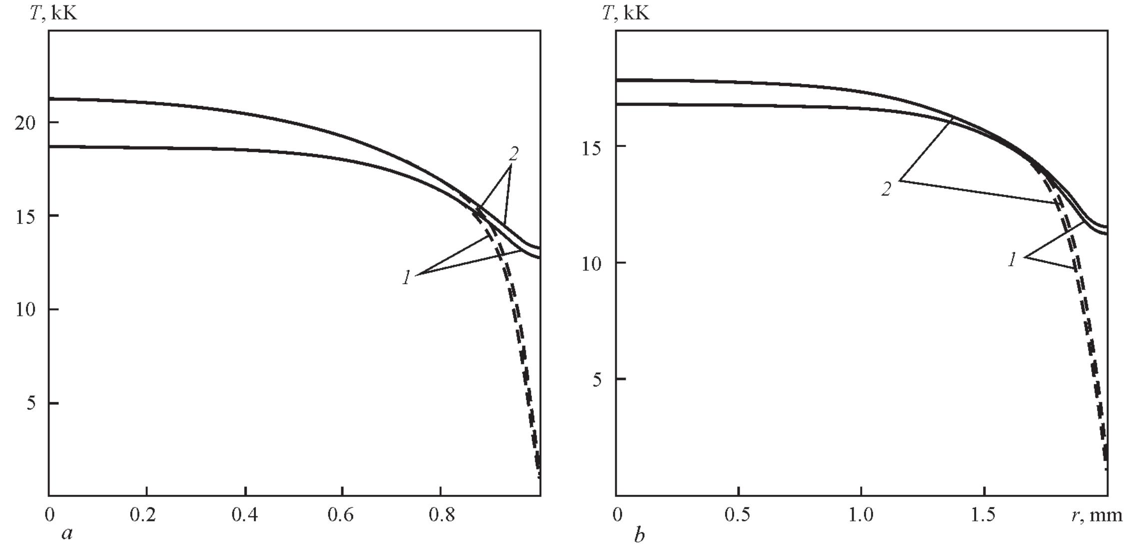

Figure 5. Radial distributions of temperature of electrons (*solid curves*) and heavy particles (*dashed*) of arc plasma in plasmatron nozzle channel: *a* — $R = 1$ mm, $G = 2$ l/min, $I = 100$ A; *b* — $R = 2$ mm, $G = 5$ l/min, $I = 200$ A; *1* — three-; *2* — four-component plasma

model, make significant contribution in formation of arc plasma characteristics with rise of their temperature in the nozzle channel at I increase. Figure 5 shows comparison of calculation distribution of temperature of electrons and arc plasma heavy particles on nozzle section, obtained using the models of three- and four-component plasma. As it follows from presented results, the temperatures of plasma component in the arc column, calculated taking into account doubly charged ions, significantly exceed corresponding values of three-component plasma. At that, arc column plasma is virtually equilibrium. Indicated difference reduces in the near-wall region, up to virtually complete matching of temperatures (separately for electrons and for heavy plasma component). The reason for this is reduction of role of doubly charged ions in the vicinity to channel wall, concentration of which here is negligibly small.

Figure 6 represents the calculation dependencies of radial distributions of absolute values of axial component of electric current density for arc in channel. Local increase of $|j_z|$ in the vicinity to channel wall can be noted together with obvious increase of current density at I rise and R decrease (see also [7, 8]). It becomes very vividly apparent at large currents and small radiuses of the channel (see solid curves in Figure 6, *a*) and is caused by increase of axial component of electron velocity in the plasma pre-layer due to reduction of frequency of their collision with heavy particles. Difference of calculation results of electric current density in scope of models for three- and four-component plasma seems to be virtually unessential.

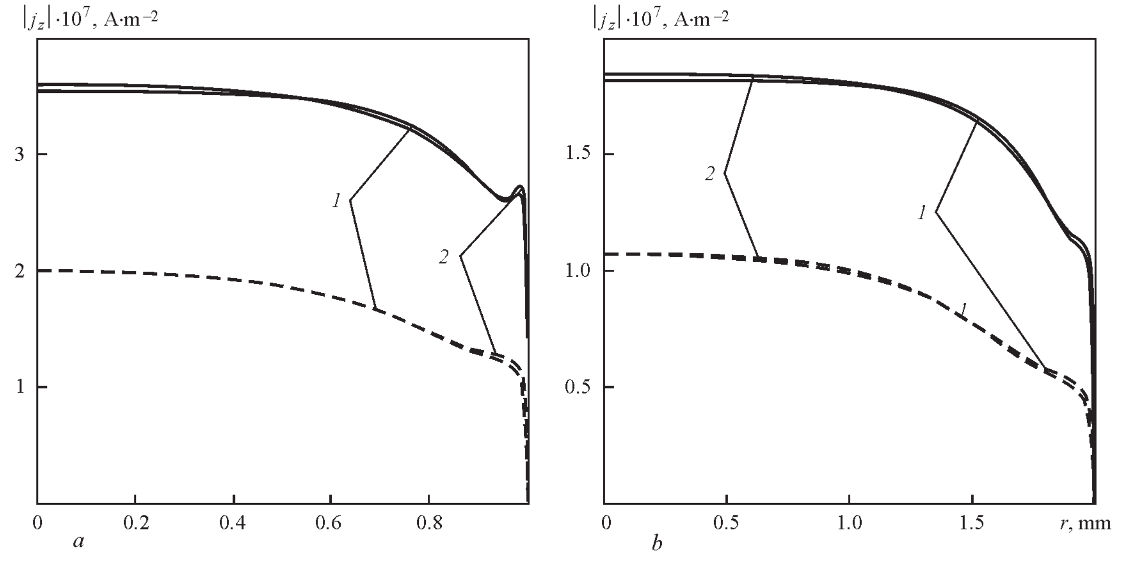

Figure 6. Radial distributions of density of electric current for arc in plasmatron nozzle channel: *a* — $R = 1$ mm, $G = 2$ l/min, I — 50 (*dashed curves*) and 100 A (*solid*); *b* — $R = 2$ mm, $G = 5$ l/min, $I = 100$ (*dashed*) and 200 A (*solid*); *1* — three-; *2* — four-component plasma

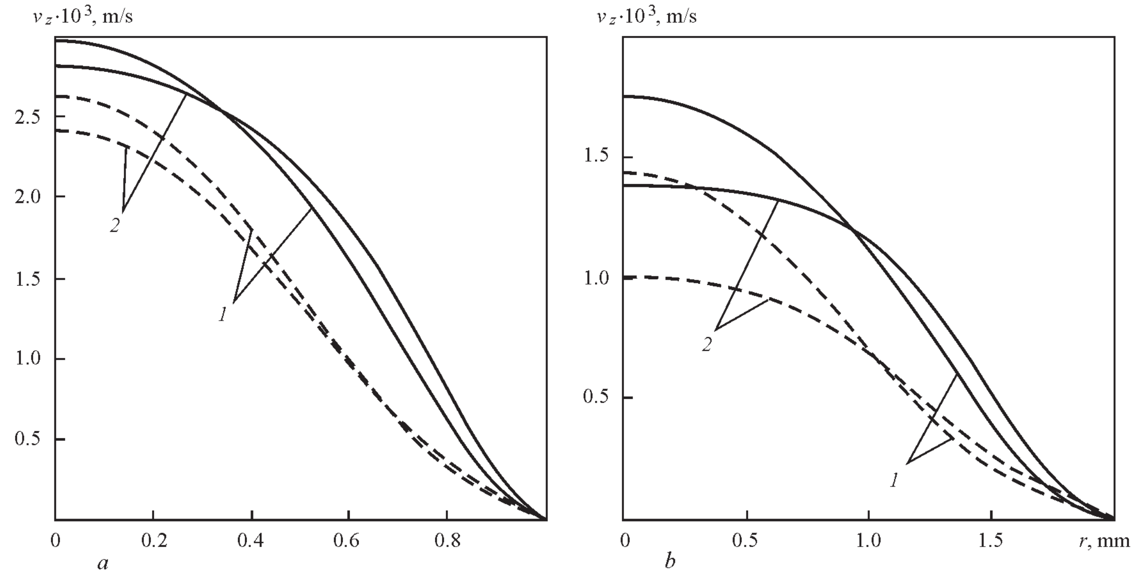

Figure 7. Radial distributions of mass-average velocity of arc plasma in plasmatron nozzle channel: *a* — $R = 1$ mm, $G = 2$ l/min, I — 50 (*dashed*) and 100 A (*solid*); *b* — $R = 2$ mm, $G = 5$ l/min, $I = 100$ (*dashed*) and 200 A (*solid*); *1* — three-; *2* — four-component plasma

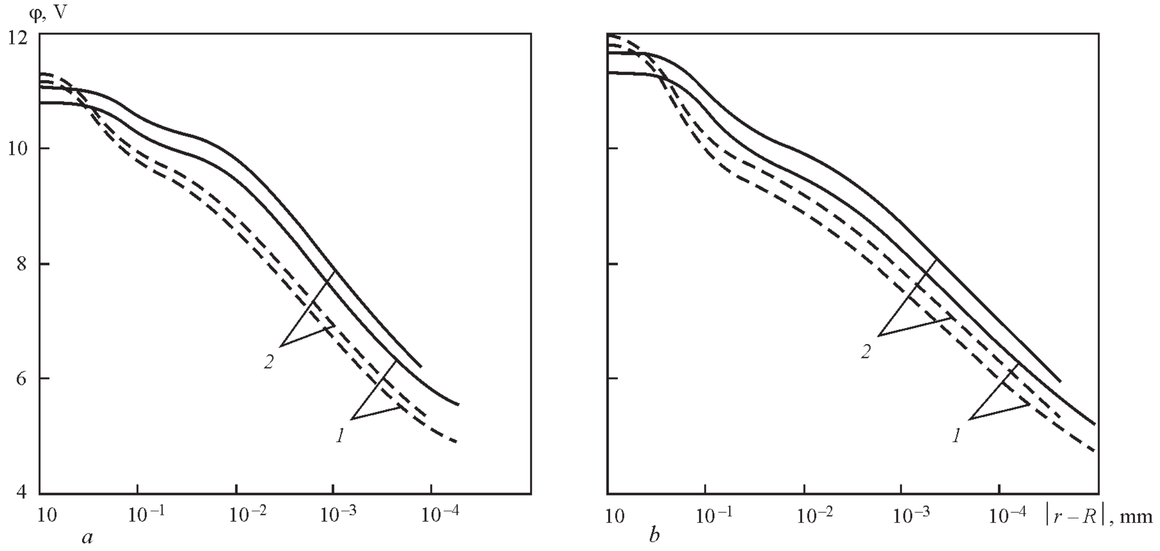

Figure 8. Radial distributions of electric potential of arc plasma in plasmatron nozzle channel: *a* — $R = 1$ mm, $G = 2$ l/min, I – 50 (*dashed*) and 100 A (*solid*); *b* — $R = 2$ mm, $G = 5$ l/min, $I = 100$ (*dashed*) and 200 A (*solid*); *1* — three-; *2* — four-component plasma

Let's study the effect of arc current, channel radius and consumption of plasma gas on radial distribution of axial component of mass-average velocity

$$v_z = \sum_{\alpha=n,i+,i++} m_\alpha n_\alpha v_\alpha^z \Big/ \sum_{\alpha=n,i+,i++} m_\alpha n_\alpha$$

of arc plasma in the channel. Plasma velocity on channel axis has virtually proportional rise at increase of relationship of plasma gas consumption to channel cross-section area (see also [7]) and to less degree at arc current rise. Difference between values of v_z, calculated in scope of models for three- and four-component plasma, in contrast to $|j_z|$, appears to be significant (Figure 7) and mainly developed in the arc column. At that, v_z value for the three-component plasma in near-axis region of the arc column exceeds corresponding values in the case of four-component plasma and it is, vice versa, in near-wall region. This effect is related with higher values of viscosity factor

Heat flow from plasma on wall channel and potential drop in space charge layer

Parameter	Calculation data	$I = 50$ A		$I = 100$ A		$I = 200$ A	
		3-comp.	4-comp.	3-comp.	4-comp.	3-comp.	4-comp.
$R = 1$ mm, $G = 2$ l/min	q_w, MW/m^2	2.115	2.184	11.730	13.140	–	–
	$\Delta\varphi_s$, V	4.46	4.57	5.10	5.31	–	–
$R = 2$ mm, $G = 5$ l/min	q_w, MW/m^2	–	–	0.260	0.221	1.614	1.448
	$\Delta\varphi_s$, V	–	–	4	4.08	4.45	4.60

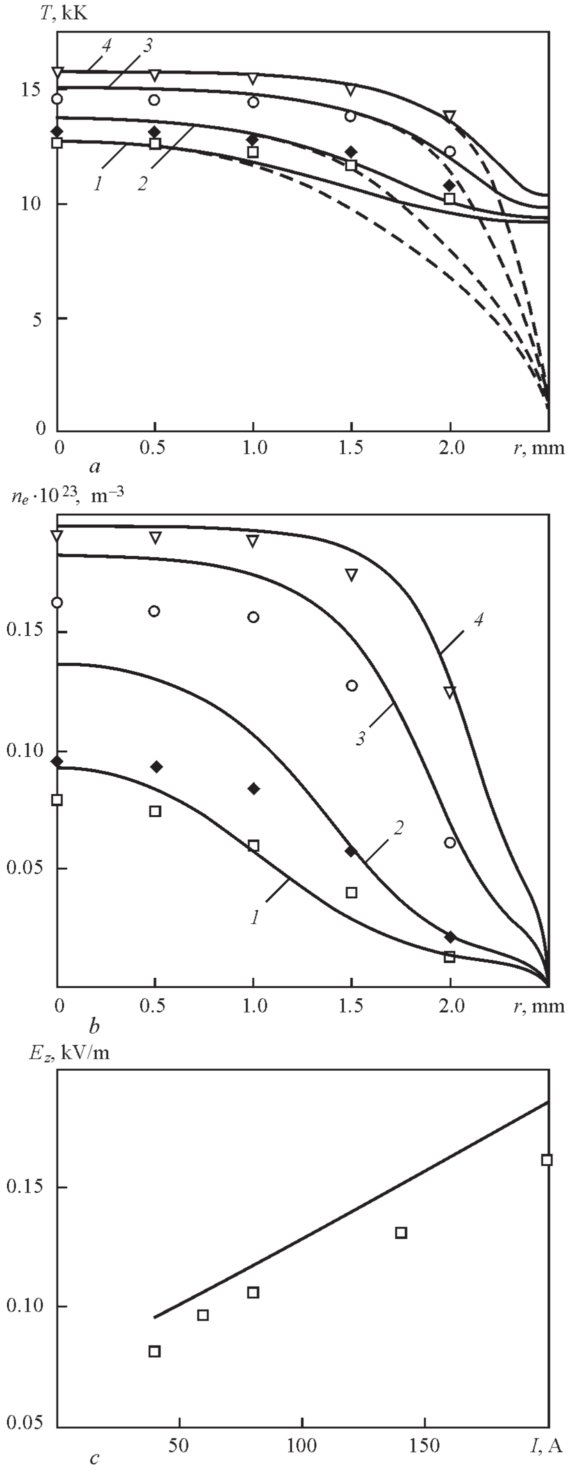

Figure 9. Comparison of calculation data (*solid curves*) with experimental (*markers*) for arc in 2.5 mm radius channel, blown out by argon flow with 0.07 l/min consumption at 60 (–), 80 (+), 140 (o) and 200 A (Δ) currents: *a* — radial distributions of electron temperature; *b* — radial distributions of electron concentration; *c* — dependence of axial component of electric field on arc current

for the four-component plasma in comparison with three-component plasma.

Now let's come to consideration of the distribution of electric potential of arc plasma on channel section (Figure 8). As it follows from calculation data presented, plasma potential on channel axis exceeds wall potential, conventionally taken as zero, by 11–12 V. Moreover, in the case of application of four-component plasma the calculation values of potential on arc column axis appear to be somewhat higher than in use of three-component model. It should be noted that specified values of potential difference between arc axis and channel wall are the sum of voltage drop in the arc column and plasma pre-layer with voltage drop in space charge layer calculated on formula (29), corresponding values of which are given in the Table. It also provides for the values of such important from practical point of view characteristic as heat flow from plasma to channel wall, calculated on formula (31).

Model verification. Adequacy of the developed model of processes of energy, pulse, mass and charge transfer in non-equilibrium plasma of electric arc in the plasmatron nozzle channel is considered by means of comparison of the calculation results, produced in scope of three-component plasma model, with available experimental data [8]. The calculation of characteristics of arc plasma was carried out under system parameters corresponding to experiment conditions [8], namely at arc current I = 40–200 A; channel radius R = 2.5 mm; volumetric consumption of plasma gas (Ar) G = 0.07 l/min; temperature of channel wall T_w = 500 K.

Figure 9 represents the results of calculation of radial distribution of temperature of electrons and heavy particles, concentration of plasma electrons as well as dependence of intensity of longitudinal electric field on arc current. Comparison of the calculation values of temperature and concentration of electrons with given in this Figure experimental data shows their totally satisfactory correspondence (maximum relative errors make 5 and 35 %, respectively). The maximum relative error in comparison of the calculation values of electric field axial component with experimental ones does not exceed 10 %. It indicates sufficiently high accuracy of results, obtained with the help of proposed model.

Conclusions

The mathematical model was proposed for non-equilibrium plasma of electric arc in asymptotic region of the channel, blown out by laminar flow of inert gas. It is used as a basis for numerical analysis of characteristics of arc plasma in the nozzle channel of direct plasmatron at different values of arc current, channel radius and consumption of plasma gas, that allows making the following conclusions:

1. Results of calculation of characteristics of studied plasma in scope of drift-diffusion approximation are virtually matched with the modelling results based

on complete set of multi-fluid equations (taking into account convective terms), that allows recommending such a simplified approach for modelling of processes of energy, pulse, mass and charge transfer in non-equilibrium arc plasma.

2. Calculations of characteristics of argon arc plasma in the plasmatron nozzle channel at arc current and channel radius in $I/R > 50$ A/mm range require taking into account plasma doubly charged ions. Such a consideration allows also calculating characteristics of plasma arc when it is effected by focused beam of CO_2-laser irradiation, propagating along the channel axis, under conditions of laser-plasma welding.

3. The calculations showed that in contrast to channel central regions, where arc plasma is virtually equilibrium, plasma in the near-wall region appears to be non-equilibrium, moreover thermally as well as ionization. Besides, potential of channel wall is significantly lower than existing value of arc plasma potential on channel axis. Corresponding difference of the potentials can make 11–12 V depending on selected values of arc current, channel radius and plasma gas consumption.

4. Comparison of results of modelling of characteristics in non-equilibrium plasma of argon arc in the plasmatron nozzle channel with available experimental data showed their totally satisfactory correspondence, that indicate adequacy of the proposed mathematical model.

This work was carried out under financial support in scope of program for foreign experts in PRC No.WQ20124400119, project of research innovation group of Guangdong province No.201101C0104901263 and international project of Ministry of Science and Technology of PRC No.2013DFR70160.

1. Meier, E.T., Shumlak, U. (2012) A general nonlinear fluid model for reacting plasma-neutral mixtures. *Physics of Plasma*, **19**, 072508.
2. Benilov, M.S. (1995) The ion flux from a thermal plasma to a surface. *J. Phys. D: Appl. Phys*., **28**, 286–294.
3. Benilov, M.S., Marotta, A. (1995) A model of the cathode region of atmospheric pressure arcs. *Ibid*., **28**, 1869–1882.
4. Almeida, N.A., Benilov, M.S., Naidis, G.V. (2000) Simulation of the layer of non-equilibrium ionization in a high-pressure argon plasma with multiply-charged ions. *Ibid*., **33**, 960–967.
5. Almeida, N.A., Benilov, M.S., Naidis, G.V. (2008) Unified modelling of near-cathode plasma layers in high-pressure arc discharges. *Ibid*., **41**, 245201.
6. Almeida, N.A., Benilov, M.S., Hechtfischer, U. (2009) Investigating near-anode plasma layers of very high-pressure arc discharges. *Ibid*., **42**, 045210.
7. Engelsht, V.S., Gurovich, V.Ts., Desyatkov, G.A. et al. (1990) *Low-temperature plasma*. Vol. 1: Theory of electric arc column. Novosibirsk: Nauka.
8. Beulens, J.J., Milojevic, D., Schram, D.C. et al. (1991) A two-dimensional nonequilibrium model of cascaded arc plasma flows. *Phys. Fluids B*, 3(**9**), 2548–2557.
9. Ignatov, A.V., Semenov, I.L. (2015) Characteristics of nonequilibrium arc plasma in channel of plasmatron nozzle. In: *Proc. of 8th Int. Conf. of Junior Scientists on Welding and Related Technologies* (Vorzel, Ukraine, 2015).
10. Benilov, M.S. (1996) Multifluid equations of a plasma with various species of positive ions and the Bohm criterion. *J. Phys. D: Appl. Phys*., **29**, 364–368.
11. Manteuffel, T.A., White, A.B. (1986) The numerical solution of second-order boundary value problems on nonuniform meshes. *Mathematics of Computation*, **47**, 511–535.

Received 24.09.2015

MODELLING OF CHEMICAL COMPOSITION OF WELD POOL METAL IN ARC METHODS OF WELDING

V.V. GOLOVKO and **L.A. TARABORKIN**
E.O. Paton Electric Welding Institute, NASU
11 Kazimir Malevich Str., 03680, Kiev, Ukraine. E-mail: office@paton.kiev.ua

Development of complex calculation algorithm based on system approach for numerical prediction of formation and growth of non-metallic inclusions in a weld metal is one of the important tasks in present time. One of significant blocks of it is a calculation estimation of weld metal chemical composition in arc methods of welding, which is of interest and being studied in present work. A procedure was proposed for calculation of content of weld pool melt in arc welding. The developed procedure is based on modelling of thermodynamics of interface interaction in metal–slag–gas-vapor phase system in a temperature range typical for weld pool existence in arc methods of welding. Predicted content of metal melt can be a basis for modelling of content, size, morphology and chemical composition of non-metallic inclusions in weld metal. 11 Ref., 3 Tables, 3 Figures.

Keywords: *arc welding, weld pool, melt, thermodynamics, inclusions, slag, chemical composition, modelling, prediction*

Development of high-strength low-alloy steels has become an outstanding achievement of ferrous metallurgy. Optimum combination of mechanical properties and efficiency of such steels production promoted their rapid development and wide implementation [1, 2]. Application of processes of refining and sparse alloying [3], in particular, provides for the possibility of achievement of such combination.

The main efforts of metallurgists were directed on production of metal with more refined grain structure, since grain size is one of the most significant factors determining service properties of low-alloy steels [4].

The experience of works on investigation of peculiarities of effect of non-metallic inclusions (NMI) on conditions of formation of structure of low-alloy steels and level of their service properties, which resulted in development of industrial technologies of production of current structural steels, indicate the relevance of investigation of effect of NMI on structure and mechanical properties of metal of welds from low-alloy steels of increased and high strength [5, 6].

In connection with it development of complex calculation algorithm based on system approach for numerical prediction of formation and growth of NMI in a weld metal is important and interesting problem. One of significant blocks of it is a calculation estimation of weld metal chemical composition in arc methods of welding, representing absolute independent interest and being considered in this work.

Submerged arc welding is one of the comprehensive processes for complex description of pattern of cause-and-effect relationship in composition–structure–properties system. All know in present time aggregative states of the material, i.e. solid state, liquid, gas phase and plasma, participate in formation of weld metal. Metallurgical reactions in these phases and at interface take place in the temperature range approximately from 1000 to 10,000 K. Duration of indicated reactions makes from 10^{-6} s to several seconds. Content of components in separate phases can significantly change in process of welding. Presence of high-gradient temperature and concentration field, typical for welding processes, make impact on character of interactions.

Additional difficulties, related with modelling of the processes of NMI formation, are induced by the fact that the main mass of inclusions is formed in molten metal of the weld pool [7], while information on chemical composition of solidified metal is used for calculations of their characteristics. At that, content of alloying and impurity elements in steel, appearing

---

[*] This issue represents several papers (pp. 12–16), prepared by members of the PWI Department «Physical-chemical processes in welding arc» devoted to the memory of developer and permanent chief of the Department Prof. Igor K. Pokhodnya. The papers highlight development of some scientific ideas and technological approaches to solution of problems for providing high quality of welding consumables, which are typical for developments of the PWI. These directions remain priority topics of the Department.

as a result of interaction between metallic and slag phases in a course of melt existence, are not considered. It can significantly effect content and chemical composition of inclusions [8]. Calculation estimation based on data on weld pool, i.e. on content of metal in a temperature range above the temperature of start of its solidification, is necessary in order to get objective information on content, morphology and size of NMI.

Step-by-step method is used to study the metallurgical peculiarities of submerged arc welding for the purpose of simplification of stated problem. Conditional schematic division of weld metal formation process on three zones, namely reaction zone at droplet stage (from iron boiling temperature 3134 to 10000 K); reaction zone in area of high temperatures (from 2500 to 3134 K); and reaction zone in area of low temperatures (from 1800 to 2500 K), is taken for this.

Three main calculation schemes were formed in accordance with this division and used for investigation of metallic, slag and gas phase, respectively.

Today the single generally available method for calculation of activities in metallic phase, which is provided by numerical values of parameters for the most elements applied in metallurgy, is Wagner (decomposition) method [9], therefore it was taken as basic one.

However, Wagner method does not include thermodynamic requirements to state equation. At the same time, a theory of subregular solutions, representing sufficiently simple model, satisfying specific thermodynamic requirements, and having significant advantages in description of multicomponent systems, is not provided with parameter numerical values.

Joint application of theory of subregular solutions with calculation of coefficients of distribution on parameters of Wagner interaction in thermodynamic model of distribution of elements between metal, slag and gaseous phase provides for higher correlation of calculation and experimental data in all area of compositions.

Model of collective electrons of Ponomarenko seems to be the best for calculation of activities in slag phase. It considers slags as a solution, components of which are the Periodic Table elements, that allows calculating their activities independently. Therefore, calculation modelling of metal–slag system uses a procedure for evaluation of thermodynamic functions of the slag as phase with collective electrons (method of collective electrons) [10], provided with all necessary numerical parameters and allowing calculating activity of the slag phase components as well as, in the most general case, taking into account nonstoichiometry of all phases.

Thermodynamic equilibrium reactor (TER) was used for calculation of gaseous phase. It is designed for calculation of chemical equilibrium in multi-component heterogeneous systems [11]. A basis of algorithm of TER program is a general principle of entropy maximum S for calculation of chemical and phase composition and corresponding program works in Chemical WorkBench program package (Kinetic Technologies) Company, Moscow, Russia).

According to indicated principle, an equilibrium state is characterized by uniform distribution of thermodynamic parameters in studied volume, and chemical composition corresponds to maximum of possibility of distribution of energy levels for macroparticles:

$$S = S_{\max} \text{ at } M_j = \text{const}; \ U = \text{const}; \ v = \text{const},$$

where M_j is the weight of j-th chemical element; U is the function of internal energy; v is the specific volume.

Corresponding state equations for calculation parameters of thermodynamic equilibrium are embedded based on the fact that entropy of multicomponent system consists of entropy of different components and phases, i.e. components of neutral gas and ions type, having ideal gas properties, and components which formed pure condensed phases (solid or liquid state) and condensed solutions. In particular, entropy of gaseous phase is determined on formula

$$S_{\mathrm{g}} = \sum_{i=1}^{k} \left(S_i^0 - R \ln \frac{RT}{v} M_i \right) M_i,$$

where S_i^0 is the standard absolute entropy; M_i is the number of moles of i-th component per 1 kg of system; $p = RTM_i/v$ of pressure of i-th component.

Entropy of components, forming separate pure condensed phase in accordance with additivity concept, equals

$$S_{\mathrm{c}} = \sum_{n=1}^{N_{\mathrm{c}}} S_n^0 M_n,$$

where S_n^0 is the entropy of condensed phase on 1 mole of a substance; M_n is the number of moles per 1 kg of the condensed phase; N is the total number of separate condensed phases.

Parameters of equilibrium state are found as values of all variables of the studied system, including number of moles of components, under condition of entropy maximum and additional limitations on parameters imposed by mass conservation law. Procedure for calculation of target parameters is based on method of Lagrange using Newton–Raphson method for solving a set of non-linear equations [11].

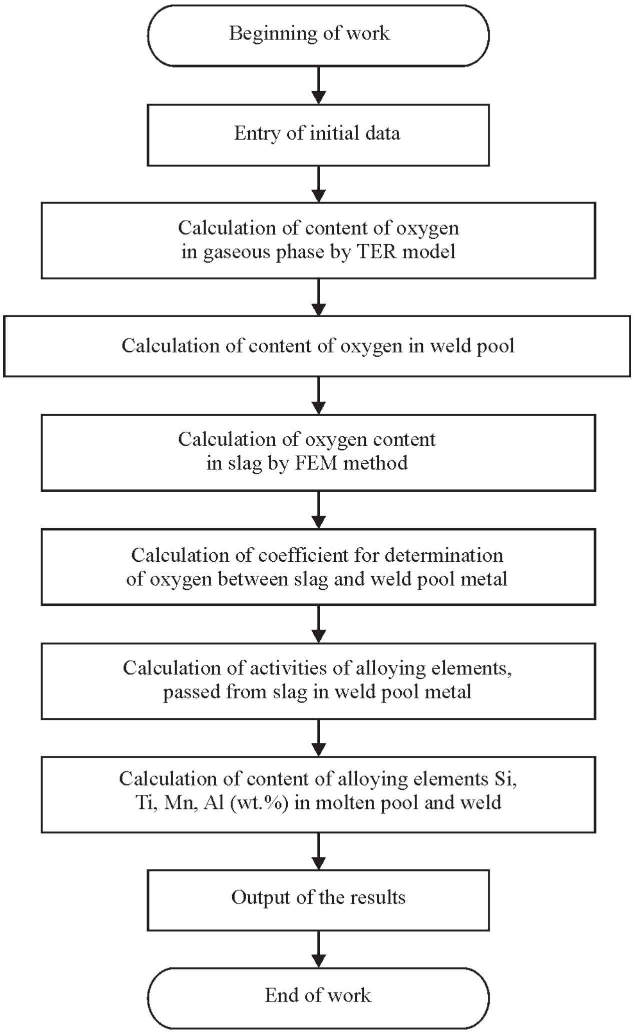

Figure 1. Block-diagram of algorithm of program for calculation of chemical composition of weld pool metal in arc methods of welding

Developed calculation scheme allows numerical evaluation of weight fraction of alloying elements in the weld pool and weld metal in submerged arc welding based on data on chemical composition of flux, wire and steel to be welded.

The following values are used as input parameters:

- chemical composition of flux, presented in oxide-slat form, moreover it is supposed that initial composition of the slag system matches with flux composition and contains all or some of mentioned components: SiO_2, $Al_2O_{3,}$ CaF_2, MgO, MnO, TiO_2, CaO, sum of percent content of which shall equal 100 %;
- weight fractions (%) of alloying components Si, Ti, Mn, Al as well as oxygen in steel and welding wire;
- portion of base metal in weld pool metal;
- temperature characteristics of studied process.

Corresponding output (resultant) variables of calculation are as follows:

- weight fraction of oxygen in weld pool;
- weight fraction of alloying elements Si, Ti, Mn, Al in weld pool;
- weight fraction of alloying elements Si, Ti, Mn, Al in weld metal.

Thus, the algorithm of calculation evaluation includes the following steps (Figure 1):

1. Determination on calculation TER of oxygen content in gaseous phase, which is entered as a result of reaction between slag and welding arc. A peculiarity of this stage is the fact that Chemical WorkBench program, among formally thermodynamically probable products of chemical reactions in droplet stage, provides for significant number of such, which on practice (due to extraordinarily small corresponding contents) can be eliminated in further calculations. Therefore, received list of reaction products is subjected to revisions and corresponding significant reduction;
2. Calculation of content of oxygen [O] in the weld pool, for which purpose to received in item 1 value, firstly, it is necessary to add fraction, coming from wire (obtained intermediate sum corresponds to oxygen content in droplet), and then add to computed value content of oxygen in base metal taking into account portion of base metal in weld pool formation. As a rule, resultant [O] value does not exceed 0.1 wt.% and, therefore, it can be equaled to oxygen activity $[a_O]$ in the weld pool;
3. Calculation of oxygen content in slag, for which it is sufficient to calculate oxygen activity (a_O) in the slag on FEM according to work [10];
4. Determination of coefficient of oxygen distribution L_O between slag and weld pool metal by formula $L_O = (a_O)/[a_O]$;
5. Calculation of activity of alloying elements $[a_{Me}]$, passing from slag in weld pool metal by formula $[a_{Me}] = (a_{Me})/L_{Me}$, where for simplicity it can be taken that coefficients of distribution L_{Me} of alloying elements between slag and weld pool approximately equals to found in item 4 coefficient L_O;
6. Calculation of content of each alloying element Si, Ti, Mn, Al (wt.%) in weld pool and weld as sum of its contents in droplet, in base metal (taking into account its portion) and alloying elements, passing from slag phase (see item 5).

Computer realizing of described algorithm was carried out in object-oriented media for visual programming Delphi 7. Developed computer program works under the operating system Windows XP.

After launching the program displays a form (Figure 2) which contains fields and tables for input and output of data, provided in algorithm description. The program allows carrying out multi-choice calculations for fixed set of values of input variables, since allows performing new calculation without complete cleaning of all form, i.e. after change of some (even

Table 1. Composition of fluxes used in investigations and their basicity, wt.%

Flux number	MgO	Al_2O_3	SiO_2	CaF_2	*BI*
3	40	30	15	15	1.83
9	20	35	20	25	1.20
14	20	40	25	15	0.78
19	35	40	0	25	3
20	35	0	40	25	1.50

one) of entered values. Check of adequacy of the developed calculation evaluation was carried out in arc welding using agglomerated fluxes, content of which was built on $MgO–SiO_2–Al_2O_3–CaF_2$ system. Scheme of weld formation, used for evaluation of portion of base metal in weld pool, is given in Figure 3.

Oxygen potential of fluxes was changed due to change of MgO/SiO_2 relationship for investigation of possibility of prediction of its effect on conditions of NMI formation.

Submerged arc welding was carried out in combination with welding wire Sv-08GA of 4 mm diameter in accordance with the requirements of ISO 14171:2000. Butt joints from low-alloy steel of 10KhSND grade of 25 mm thickness with 60° beveling and 20 mm gap in weld root were produced in course of experiments. Templates for production of mircosections for metallographic investigation were cut out from metal of the last layer, which was located in the middle of the upper layer.

Metallographic investigations were carried out on transverse microsections, cut out from welded joints. Quantitative analysis of NMI and determination of general contamination of the weld with inclusions was performed with the help of optical microscope Neophot-30 (Carl Zeiss Jena, Germany), equipped with high resolution digital camera. In particular, distribution of inclusions on size was determined using images of 2592×1944 pixels size. Calculation of amount of inclusion in each specimen on size group, i.e. from minimum to maximum size, was carried out on set program. Analysis of NMI chemical composition were performed on electron microscope JSM-35 (Japan) with the help of energy dispersion spectrometer INCA-350 (Great Britain) «point by point» with the purpose of elimination of background radiation.

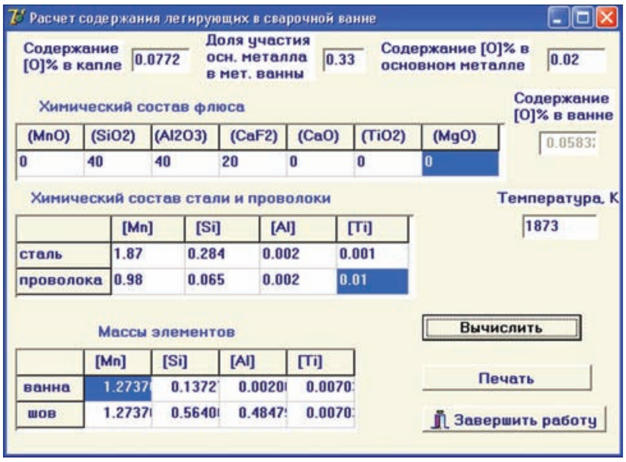

Расчет содержания легирующих в сварочной ванне

Содержание [O]% в капле: 0.0772

Доля участия осн. металла в мет. ванны: 0.33

Содержание [O]% в основном металле: 0.02

Содержание [O]% в ванне: 0.0583

Температура, K: 1873

Химический состав флюса

(MnO)	(SiO2)	(Al2O3)	(CaF2)	(CaO)	(TiO2)	(MgO)
0	40	40	20	0	0	0

Химический состав стали и проволоки

	[Mn]	[Si]	[Al]	[Ti]
сталь	1.87	0.284	0.002	0.001
проволока	0.98	0.065	0.002	0.01

Массы элементов

	[Mn]	[Si]	[Al]	[Ti]
ванна	1.2737	0.1372	0.0020	0.0070
шов	1.2737	0.5640	0.4847	0.0070

Figure 2. Window of program for numerical modelling of transfer of alloying elements in molten pool and weld in submerged arc welding

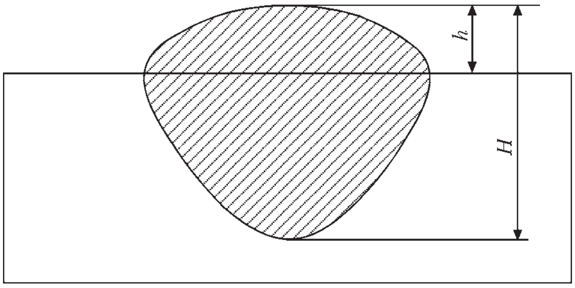

Figure 3. Scheme of weld formation

Compositions of experimental fluxes (Table 1; in general it was 20 variants) were calculated in accordance with optimum mathematical experimental plan. Values of their basicity were calculated by formula

$$BI = \frac{MgO + CaF_2}{SiO_2 + 0.5Al_2O_3}.$$

Table 2 provides for the results of correlation of calculated contents of oxygen and alloying elements in the weld metal with data on their determination in specimens of deposited metal obtained in welding using pilot fluxes. Content of these elements is given in Table 3.

Observed differences between calculation and experimental data are caused by processes of formation of NMI in wed metal in two-phase zone, located in interdendritic volumes at temperatures below equilibrium solidification temperature. Besides, they one more time underline that prediction of content and composition of NMI in metal of formed weld can not

Table 2. Calculation (in weld pool) and experimental (in weld metal) content of elements

Flux number	Experimental data, wt.%				Calculation data, wt.%			
	O	Mn	Al	Si	O	Mn	Al	Si
3	0.035	0.71	0.0108	0.637	0.1426	1.1474	0.2025	0.8445
9	0.029	0.67	0.0128	0.668	0.0548	1.1904	0.3877	0.6750
14	0.046	0.65	0.0154	0.676	0.0618	1.1904	0.4312	0.7145
20	0.028	0.63	0.0080	0.688	0.0581	1.1818	0.4059	0.8680
19	0.024	0.75	0.0182	0.583	0.3370	1.1732	0.0020	0.4831

Table 3. Content of oxygen and alloying elements in base metal and wire

Material	Content, wt.%			
	O	Mn	Al	Si
Base metal	0.005	0.87	0.002	0.280
Wire	0.016	0.98	0.002	0.065

be based on data on its chemical composition, being final product of all processes and reactions which took place. Application of calculation data on composition of «virtual» weld pool is more adequate for this purpose.

The similar approaches were performed for other alloying elements (Ti, Si, Al). Thus, the calculation data on content of alloying elements and oxygen in weld metal, obtained with the help of described model, can serve as initial values for modelling integral composition of NMI, such as morphology as well as composition of separate phases, forming these inclusions, based on objective information on initial conditions of their formation.

Proposed approach and developed calculation scheme can be distributed on other methods of arc fusion welding (with coated electrodes, flux-cored wire), which includes metallic, vapor-gas and slag phases.

Conclusions

The method was proposed for calculation of composition of weld pool metal melt. Developed procedure is based on modelling of thermodynamics of interface interaction in metal–gas–vapour phase system in a temperature range typical for existence of weld pool in arc methods of welding. The predicted composition of metal melt can serve as initial base for further modelling of content, size, morphology and chemical composition of non-metallic inclusions in weld metal.

1. Weng, Y. (2003) Microstructure refinement of structural steel in China. *ISIJ Int*., 43(**11**), 1675–1682.
2. Borovikov, A.V. (2003) Production of straight-seam large-diameter pipes made of steel of strength class X80. *Metallurgist*, Vol. 47, 9–10.
3. Kim, Y.M., Kim, S.K., Lim, Y.J. et al. (2002) Effect of microstructure on the yield ratio and low temperature toughness of line pipe steels. *ISIJ Int*., 42(**12**), 1571–1577.
4. Shukla, R., Das, S.K., Kumar, B.R. et al. (2012) Ultra-low carbon, thermomechanically controlled processed microalloyed steel: Microstructure and mechanical properties. *Metallurg. and Mater. Transact. A*, 43(**12**), 4835–4845.
5. Park, J.S., Lee, C., Park, J.H. (2012) Effect of complex inclusion particles on the solidification structure of Fe–Ni–Mn–Mo alloy. *Ibid*., *B*, 43(**12**), 1550–1557.
6. Sarma, D.C., Karasev, A.V., Jonson, P.G. (2009) On the role of nonmetallic inclusions in the nucleation of acicular ferrite in steels. *ISIJ Int*., 49(**7**), 1063–1074.
7. Babu, S.S. (2009) Thermodynamic and kinetic models for describing microstructure evolution during joining of metals and alloys. *Int. Materials Rev.*, **6**, 333–367.
8. Zinngrebe, E., Van Hoek, C., Visser, H. et al. (2012) Inclusion population evolution in Ti-alloyed Al-killed steel during secondary steelmaking process. *ISIJ Int*., 52(**1**), 52–61.
9. Jung In-Ho, Decretov, S.A., Pelton, A.D. (2004) Computer application of thermodynamic databases to inclusion engineering. *Ibid*., 44(**3**), 527–536.
10. Grigoryan, V.A., Stomakhin, A.Ya., Ponomarenko, A.G. (1989) *Physical-chemical calculations of electric steelmaking processes*. Moscow: Metallurgiya.
11. (2007) *CHEMICAL WORKBENCH Vers. 3.5: Description of reactor models*. Moscow: Kinetic Technologies.

Received 27.10.2015

RHEOLOGICAL INVESTIGATIONS OF NON-ISOTHERMAL PRESSURE FLOWS OF COATING MIXTURES FOR WELDING ELECTRODES

A.E. MARCHENKO
E.O. Paton Electric Welding Institute, NASU
11 Kazimir Malevich Str., 03680, Kiev, Ukraine. E-mail: office@paton.kiev.ua

Continuous flow capillary viscosimeter, presented in the form of abruptly narrowing stepped channel, and INSTRON 1251 testing machine were used to model the processes of pressure flow of coating mixtures for welding electrodes in extrusion chamber and in die space of production extruding machine. Thermocouple measurements were used to study the thermal conditions in pre-capillary zone, and visualization method was applied to analyze the structure of flow in it. Mathematical apparatus developed for calculation of rheological characteristics of polymer materials in the state of viscoelastic pressure flow was applied to calculate similar characteristics of the two types of coating mixtures for two types of low-hydrogen electrodes made with application of viscous in one and low-viscous liquid glass in another one. Grain composition of their filler is the same. Values of viscoelastic characteristics of the mixtures were calculated, including shear and longitudinal viscosity, elastic potential, first difference and coefficient of first difference of normal stresses and the relaxation period. Their dependencies on geometrical dimensions of stepped channels and values of volume flow of the mixture at capillary measurements were analyzed and commented upon, allowing for suspension nature of the mixtures, as well as resistance of pressure flows formed in them to viscoelastic instability. 12 Ref., 3 Tables, 12 Figures.

Keywords: *rheology, welding electrodes, mixtures for coatings of low-hydrogen electrodes, viscoelastic characteristics of mixtures, pressure flow instabilities*

As the coating mixture passes from the working cylinder of extruding machine into the sizing die, in which the coating mixture envelops the metal rods, its flow cross-section decreases, and its rate rises by tens of times. Here, the mixture properties, which determine the manufacturing properties and working characteristics of welding electrodes, change essentially. For many years it was not known exactly which of these properties change, to what extent and in which way. Essentially, this is why the very physico-chemical nature of coating mixtures proper remained unclear. The work [1] published 65 years ago, even though it did not disclose this nature, nonetheless, provided objective evidence of the fact that this cannot be done, proceeding just from the concepts of electrode coating mixture viscosity.

Application of colloidal materials science and engineering rheology approaches at PWI for the last 10–15 years allowed establishing that electrode coating mixtures, similar to other kinds of highly-concentrated suspensions of hard particles in viscous liquid medium, are characterized by elastic properties alongside viscosity. Not only shear and longitudinal viscosity, but a number of elasticity characteristics should be used for complete description of their rheological properties.

The elastic component, first of all, essentially improves energy consumption for organizing the mixture pressure flow for their application on electrode rods. Alongside that, certain combinations of mixture viscosity and elasticity cause their unstable flow. At pressing of welding electrodes, it results in different thickness of the coating, markedly impairing the electrode technological properties. The above instability, as a rule, develops at the transition stage of flow formation, while it, passing through the forming channels in the extruding machine or in the measuring cell of the capillary viscosimeter, after change of its section, direction or rate, reaches the steady-state flow mode. It can develop both in the capillary, and in the zone before it [2–4].

Experimental study of the causes for or mathematical modeling of the conditions, provoking appearance of instabilities of coating mixture pressure flows, should be performed, as in polymer rheology, with application of stepped channel model of continuous-flow type in the first case. In it the flow section decreases abruptly (step-like) or more seldom, gradually narrowing, at transition from the tank (mixture container) to the die (or capillary). Here, the flow is accelerated, either by increasing the degree of jet reduction at unchanged tempo of mixture injection into the die, or by increasing the plunger speed at unchanged degree of reduction.

The paper presents the results of PWI investigations of pressure flow of electrode coating mixtures through round continuous-flow stepped channels. The objective of investigations is to clarify the extent of the influence of channel geometry and techniques of regulation of flow modes on the temperature, structure, rheological parameters and of stability characteristics of electrode coating mixture pressure flows.

Methods and objects of investigation. *Rheological properties of electrode coating mixtures* were studied, mainly, with application of capillary viscosimeter OB 1435 — continuous flow extruder with electromechanical drive. Flow quantity is regulated in steps by replacement of gears and capillaries [5]. In factory model of viscosimeter at diameter of standard working cylinder (tank) D_R = 30 mm the flow is regulated in the range from 1 to 25 $cm^3 \cdot s^{-1}$. Using a capillary with diameter d_c = 2–6 mm, average gradient of shear rate can be assigned in the range from 1 to $8 \cdot 10^3$ s^{-1}. It was insufficient to achieve the objectives of planned research. To expand the range of shear rate gradients $\dot{\gamma}_{sh}$ towards creep flow modes ($Q < 1$ $cm^3 \cdot s^{-1}$, $\dot{\gamma}_{sh}$ up to 0.1 s^{-1}), tanks of 15 and 10 mm diameter were used alongside the standard one. Performed rheological measurements included both the entrance and capillary zone. Extruding the mixture through holes of 2, 4 and 6 mm diameter in a flat disc 1 mm thick, entrance zone resistance P_0 was measured. Capillaries of reduced length $L = 10d_c$ were applied to assess the total pressure losses in measuring cell, including the entrance zone and capillary. Values of P_0 and $(P_L - P_0)$ were used to calculate the required rheological parameters of mixtures characterizing their technological properties, namely:

- shear τ, longitudinal σ stresses, as well as the first difference of normal stresses σ_1;
- shear λ and longitudinal η viscosities generated by these stresses and normal stress coefficient ξ;
- angle of natural convergence α_0;
- relaxation period of elastic stresses θ;
- value of first difference of normal stresses σ_1/τ normalized by τ.

Shear rate gradient and stress were calculated by the formulas $\dot{\gamma}_{sh} = 8Q/\pi d_c^3$ and $\tau = (P_L - P_0)d_c/4L$. Above-mentioned procedures of measurement and calculation, as well as other rheological indices used in this study, are described in detail in [2, 4, 5].

Table 1 gives the complete plan and results of experiments.

Non-standard tanks of 50, 70 and 90 mm diameter were used to expand $\dot{\gamma}_{sh}$ range towards greater values, so that maximum possible value of mixture flow per second Q could reach 200 $cm^3 \cdot s^{-1}$. INSTRON 1251 testing machine was used to provide test loads, sufficient for mixture extrusion from tanks of such a large cross-section. In this case, rheological measurements were limited by entrance zone, i.e. by determination of just P_0 parameter.

Thermal conditions in the flow zone were studied with application of chromel-alumel thermocouple, measuring junction of which was placed into a circular recess at capillary output edge $L = 3d_c$,

Table 1. Plan and results of experiments used for calculation of rheological characteristics of S2 and N2 coating mixtures

d_c, mm	D_R/d_c	Q, $cm^3 \cdot s^{-1}$	P_0, MPa	P_L, MPa	D_R/d_c	Q, $cm^3 \cdot s^{-1}$	P_0, MPa	P_L, MPa	D_R/d_c	Q, $cm^3 \cdot s^{-1}$	P_0, MPa	P_L, MPa
	D_R = 10 mm				D_R = 15 mm				D_R = 30 mm			
Mixture S2												
2	5.0	0.11	18	45	7.5	0.25	24	46	15.0	1.0	10	30
		0.57	18	63		1.28	26	50		5.1	15	40
		1.70	27	72		3.82	12	52		15.3	18	54
4	2.5	**0.11**	**27**	**72**	3.75	**0.25**	**12**	**32**	7.5	**1.0**	**8**	**22**
		0.57	27	90		1.28	16	32		5.1	10	34
		1.70	**45**	**99**		**3.82**	**20**	**40**		**15.3**	**11**	**44**
6	1.7	0.11	18	56	2.5	0.25	8	36	5.0	1.0	6	22
		0.57	18	59		1.28	12	36		5.1	8	22
		1.70	36	72		3.82	12	36		15.3	10	32
Mixture N2												
2	5.0	0.11	16	31.5	7.5	0.25	24	32	15.0	1.0	16.5	26
		0.57	16	31.8		1.28	20	36		5.1	16.5	35
		1.70	16	45		3.82	16	46		15.3	19.5	41
4	2.5	**0.11**	**18**	**36**	3.75	**0.25**	**20**	**32**	7.5	**1.0**	**14.5**	**28.5**
		0.57	10	27		1.28	16	32		5.1	14.5	44.5
		1.70	**13.5**	**36**		**3.82**	**14**	**36**		**15.3**	**14.5**	**28.5**
6	1.7	0.11	14.5	54	2.5	0.25	12	40	5.0	1.0	13.5	27
		0.57	14.5	37.8		1.28	12	38		5.1	13.5	32
		1.70	9	22.5		3.82	12	32		15.3	9.5	37

Note. Grey colour denotes anomalous cases characteristic for structured mixtures, bold symbols denote experiments on flow structure visualization.

Table 2. Composition and characteristics of NaK liquid glasses

Mixture index	Liquid glass characteristic		Fraction of liquid glass/water, wt.%	Mixture P_m, MPa	Instrument name; container diameter D_R, mm
	Modulus	Viscosity, mPa·s			
S2	2.95	500	27.0/0	0.10	Capillary viscosimeter OB 1435; 10, 15 and 30
N2	3.15	80	14.5/4.5	0.75	
S3	2.90	1000	26.5/0	0.10	INSTRON testing machine; 50, 70 and 90
N3	3.30	100	24.0/0	0.60	

pressing it tightly to the case by a rubber ring. Temperature was controlled in each experiment. If required, temperature was recalculated to capillaries with $L = 10d_c$, used for measurement of rheological indices, by the values of dissipative function τV [6]. Temperature of thermocouple cold end was equal to 25 °C.

For visualization of mixture flow profile in the entrance zone, the method of mixture painting with phenolphtalein was used. Experiments were performed in OB 1435 viscosimeter. The billet composed of alternating discs was pre-pressed from painted and unpainted mixtures, was extruded from the respective mixture tank of the viscosimeter through a flat disc with hole diameter of 4 mm at minimum and maximum plunger feed rate V_R, equal to 0.15 and 2.15 cm·min^{-1}. Shear rate gradient in the hole here was equal to 40 and 610 (D_R = 30 mm), 0.25 and 3.80 (D_R = 15 mm), as well as 0.10 and 1.70 s^{-1} (D_R = 10 mm). In Table 1 the results of P_0 and P_L measurements taken in these modes are shown in bold. At the right moment the rod was stopped. The rest of the briquette was taken out of the tank, cut along the meridian plane and photographed.

Experimental coating mixtures with filler material composition similar to that of UONI 13/55 electrode coating were studied. In the dry mixture composition, the fraction of particles smaller than 0.063 mm was equal to 30 %, and fraction ratio is close to the one, which provides minimum share of intergranular voids in the compacted layer. NaK was used as liquid glass to prepare the coating mixtures. Table 2 gives its characteristics and application conditions. In S2 and S3 mixtures made with glasses with viscosity of 500 and 1000 mPa·s, the viscous component of pressure losses prevails over the elastic one. Owing to low viscosity of the binder, N2 and N3 mixtures are characterized by a sufficient degree of structuredness and, therefore, relatively high elasticity. This is indicated by their high plastic strength P_m. Mixtures, indexed as S2 and N2, were studied with application of OB 1435 viscosimeter, and S3 and N3 mixtures — in INSTRON testing machine.

1 % of powder-like Na-KMTs of 85SO grade was added to coatings with S index, and 1.5 % of it was added to those with N index. Coating plastic strength P_m was determined by conical plastometer. Coating mixtures were prepared in laboratory intensive mixer.

Test results. Thermal conditions in the flow zone can be judged by the results of measurements given in Figure 1. They show that N2 mixture in the condition of pressure flow, formed in stepped channels with different tank sections, is heated to lower temperature than S2 mixture, in view of its higher structuredness.

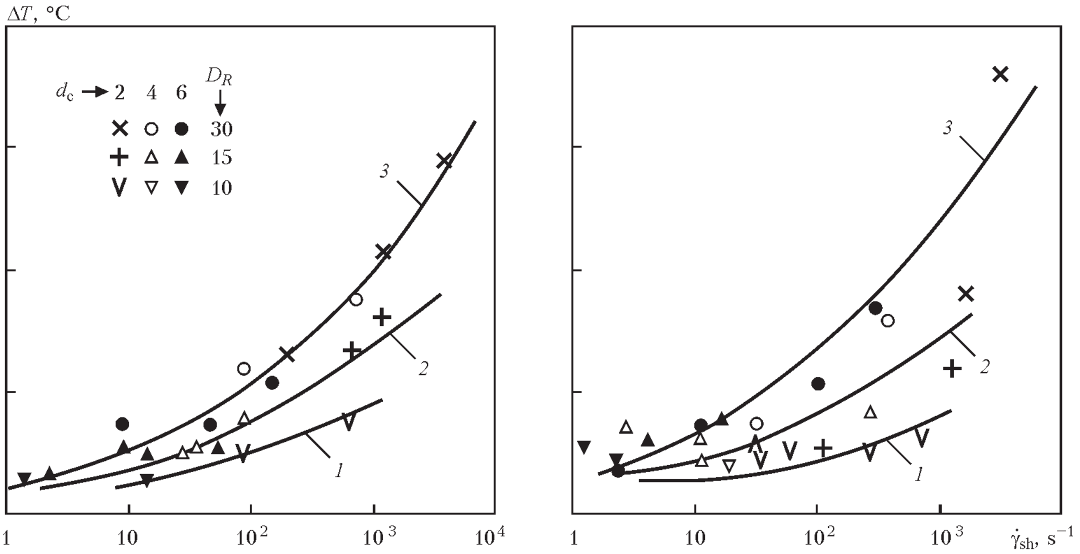

a *b*

Figure 1. Change of temperature of S2 (*a*) and N2 (*b*) coating mixture jet as a result of their viscous heating, depending on average gradient of shear rate at D_R = 10 (*1*), 15 (*2*) and 30 (*3*) mm and d_c = 2, 4 and 6 mm

Maximum temperature of the flow of both the mixtures rose progressively with $\dot{\gamma}$ increase and reached 55–65 °C, respectively. It decreased with reduction of tank diameter the greater, the higher $\dot{\gamma}_{sh}$. As follows from the above graphs, $\Delta t = f(\dot{\gamma}_{sh})$ dependencies were stratified in three levels. Located above all the others are the results obtained at $D_R = 30$ mm (curve *3*), in the middle are the results found at $D_R = 15$ mm (curve *2*), and the lowest ones are those obtained at $D_R = 10$ mm (curve *1*). Jet temperature rises under the influence of Q flow increase and decreases with increase of the degree of jet reduction $\beta = D_R/d_c$. At $\beta = \text{const}$ and $V_R = \text{const}$ jet temperature was higher, when larger section tank was used, and the more so, the higher V_R. This is related to increase of the flow, greater in the second case than in the first one.

Similar regularity was observed also in our previous research, in which the jet temperature was recorded at $D_R = 30$ mm, changing just the flow and diameter of the capillary [5].

A significant influence of jet heating on mixture viscosity can be anticipated in experiments with $D_R = 30$ mm, conducted at maximum flow per second. Temperature of the jet flowing out of the nozzle in creep flow mode ($D_R = 10$ mm) cannot influence the coating viscosity, even if capillaries with $L = 10d_c$ are used.

Flow profile. Results of visualization of patterns of S2 and N2 mixture pressure flow are shown in Figure 2. The given photos reflect the flow condition at the moment of rod stopping. They demonstrate that under the conditions of laminar flow, the mixture flows by the mechanism of mutual telescopic displacement of the layers, which is complicated by large, non-uniform and non-monotonic deformations. Judging by the shape of flow lines in the entrance zone, flow structures of the compared mixtures, differing essentially by the degree of structuredness, react differently to change of outflow rate and diameter of the tank.

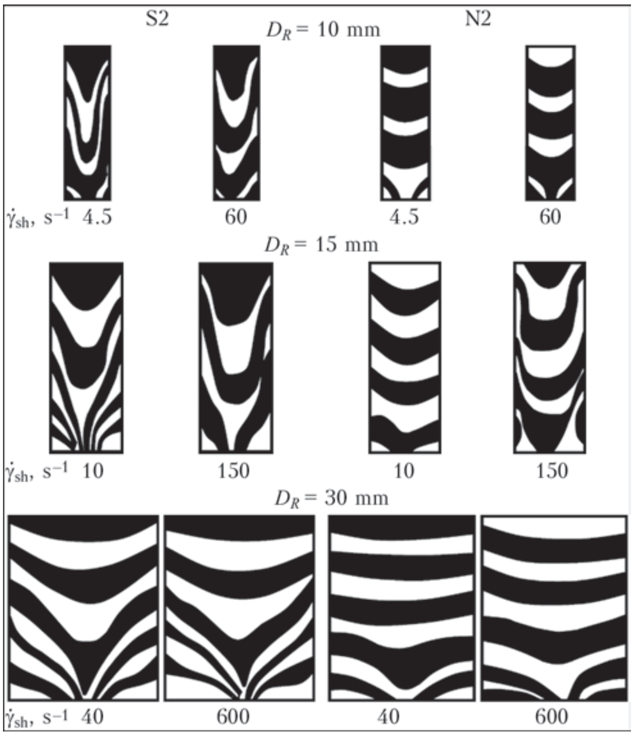

Figure 2. Flow profile of S2 and N2 mixture in the tank of capillary viscosimeter with $D_R = 10$, 15 and 30 mm through hole of 4 mm diameter

Let us first consider the flow of S2 mixture with viscous liquid glass in the container of $D_R = 10$ mm at minimum flow ($\dot{\gamma}_{sh} = 4.5$ s^{-1}). Here slow (creep) flow is in place. Long time before coming to outlet hole the central longitudinal layers of the billet, the least affected by the braking action of the tank cylindrical wall, are significantly accelerated, and, moving by the shear mechanism, form, together with other layers, a flow profile close to the parabolic one, as in an infinite pipe. The profile is almost flat in its core, with the same thickness as that of the initial layer. On the boundary with the tank wall, the layer thickness is minimum. With increase of the flow up to the maximum one (60 s^{-1}) there are indications of coating sliding along the tank wall, so that the initial layer thickness on the wall is preserved for a longer time at this rate.

In the tank of 15 mm diameter ($\dot{\gamma}_{sh} = 10$ s^{-1}) dissipative heating of the coating begins to affect its flow, and its pattern becomes more complicated. Layer thickness decreases closer to the outlet hole. This should be promoted also by «pressing» action of stagnation zones, created in the solid angle, formed by the tank cylindrical and end walls. This is confirmed by the horn shape of the flow closer to the outlet hole. In the experiment with $\dot{\gamma}_{sh} = 150$ s^{-1} a cohesion stalling of the flow is observed, which can be regarded as the result of discharging of elastic energy, accumulated in the mixture in the previous deformation period. Indications of pressing action of elastic stresses were more clearly manifested here than in other experiments. A very narrow convergent angle at the entrance to the hole most probably forms under their influence. A similar flow pattern was observed in the pressure flow of plasticine, used to simulate the pattern of metal billet flow in work [7]. The deformation zone still is of quite considerable extent.

At container diameter of 30 mm, the flow, irrespective of its rate, acquires the horn shape almost immediately after its movement starts, and the space, in which deformation occurs, still takes a quite large volume.

N2 mixture in narrow containers demonstrates the cork profile of the flow. Compared to S2 mixture, its deformation is concentrated in the short zone, directly adjacent to outlet nozzle. Apparently, under the influence of accumulated elastic stresses, the magnitude of which for this type of mixture is anticipated to be higher than that of S2 mixture, at container diameter of 15 mm and $\dot{\gamma}_{sh} = 150$ s^{-1} signs of its sticking to container side wall appear (deformed volume of the mixture rises significantly at the same time). In this case, an obvious jet stalling is recorded, resulting from relieving of elastic stresses, which, apparently, is accompanied by its heating. When breaking through to the outlet hole, the flow overcame the pressing action of the stagnation zone. The photo shows its circular residue, adjacent to container edge surface.

In the container of 30 mm diameter, the deformation zone with weakly pronounced horn-shaped flow profile, directly adjacent to the outlet hole, was again reduced in volume.

In all the photos, indications of flow non-monotonic nature are also visible, alongside the above-described manifestations of its non-uniformity. The former, in our opinion, are manifested, primarily, as deviations of deformed layers profile from the axially symmetric shape. It is important to note that flow profile formation in viscous mixture starts a long way before the capillary mouth, which the mixture enters with an already formed profile. In low-viscosity mixture this process just begins on approach to the capillary. It is completed, apparently, in the capillary initial section. This is exactly where pulsation of the coating mixture jet [2] and of polymer melts [8] begins.

Reaction of low-viscosity mixture flow to capillary elongation is also unusual that is described below.

Extrusion curves. Similar to experiments, conducted with application of capillary viscosimeter with working cylinder with $D_R = 30$ mm, the results of which are published in [2–4], it was found that the nature of extrusion curves depends on the consistency of coating mixtures and their pressure flow modes. In S2 mixtures with viscous liquid-glass binder, all of them, irrespective of the container section, have a smoothed shape, which is little affected by the flow rate. This means the tempo of pressure rise at initial deformation stage, its surge at the moment of flow beginning, and tempo of subsequent lowering, right up to reaching the steady-state stage. Increase of deformation rate smoothes all the starting peaks, as accumulation of elastic stresses in the flow is essentially accelerated [2]. In the experiments with working cylinder with $D_R = 15$ mm and $d_c = 4$ mm, curves of very interesting shape were observed, characterized by slow pressure build-up and its lowering after achievement of peak value (Figure 3). Such a shape is indicative of low and approximately equal rates of elastic stress accumulation and relaxation that is characteristic for completion of the creep flow stage. It was exactly in this experiment that visualization revealed the profiles, characteristic of flow stalling. In the extrusion curves they are manifested in the form of falling of the descending branch of pressure evolution below the level, recorded in the previous, less fast flow mode. As follows from the data, given in Table 1, this kind of stalling in viscous S2 mixture was recorded in this experiment only for curve $P_0 = f(t)$. This is also confirmed by its shape in Figure 3. In $P_L = f(t)$ curve no elastic pressure relief was observed. This leads to the conclusion that the capillary inner surface in the absence of near-wall slipping is capable of containing elastic stress relaxation up to a certain moment.

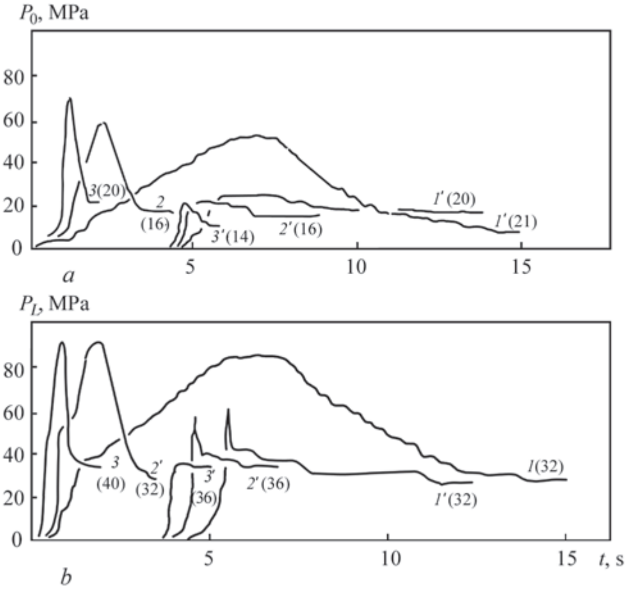

Figure 3. Shape of extrusion curves $P_0 = f(t)$ (*a*) and $P_L = f(t)$ (*b*) recorded at testing coating mixtures S2 (*1*, *2*, *3*) and N2 (*1´*, *2´*, *3´*) at shear rate gradient of 10, 50 and 150 s^{-1}, respectively, at $D_R = 15$ mm and $d_c = 4$ mm (pressure values are given in brackets)

In N2 coating mixture, made with low-viscous liquid glass, the tempo of rising, as well as lowering of peak pressure is, as a rule, essentially higher, particularly, when it concerns $P_L = f(t)$ curves. Judging by the number of shaded cells in Table 1, there are many more such anomalous cases, characteristic for structured mixtures [2–4], than in its viscous analog under the same flow conditions. In two experiments out of six, it was found for $P_0 = f(t)$ and $P_L = f(t)$, in three experiments — just for $P_0 = f(t)$, and in two cases — just for $P_L = f(t)$. This leads to the conclusion that the capillary surface is capable of not only delaying, but under certain conditions provoking an instantaneous relaxation of elastic stresses, for instance, under the influence of dissipative heating, as well as a result of near-wall slipping of the jet by the adhesion, or, less frequently, by the cohesion mechanism [8].

Such pressure releases are one of the indications of flow stability disturbance under the influence of elastic stress relaxation.

Flow curves. $P_0 = f(\dot{\gamma}_{sh})$ and $\tau = f(\dot{\gamma}_{sh})$ flow curves are presented in the graphic form results of simultaneous analysis of visualized patterns and synchronously recorded mode parameters of pressure flow of coating mixtures. In compared mixture flows through stepped channels they, similar to other viscoelastic materials, have the form of curves in logarithmic homology, inclined to rate gradient axis to a larger or smaller degree. Flow curves of S2 mixture are characterized by a larger angle of inclination than in N2 mixture, as the first is closer as to its properties to the Newtonian fluid than is the second one.

In such a systematized and convenient for consideration form, they, in our opinion, provide documented confirmation of the following important points.

The structure and rheological parameters of pressure flow of coating mixtures in stepped channel form under the influence of disturbing action of the tank edge wall, abrupt reduction of the jet at the entrance to the capillary, adhesion braking of the flow by tank and capillary walls, its viscous heating in the zone of maximum shear deformation, accumulation and relaxation of elastic stresses. Some of the above factors influence the mixture indices adiabatically relative to each other. Mixture flows react to the above-mentioned kinds of disturbances by changing the balance of energy consumption for flow both in the tank, and in the capillary. For instance, if viscosity of S2 and N2 mixtures prevails over elasticity, and this is in place at D_R = 30 mm, their flow curves $P_0 =$ $= f(\dot{\gamma}_{sh})$ are invariant, i.e. independent on volume flow and capillary section. In experiments with smaller containers, figurative points move down as a result of elastic stress relaxation to more favourable energy levels of the flow.

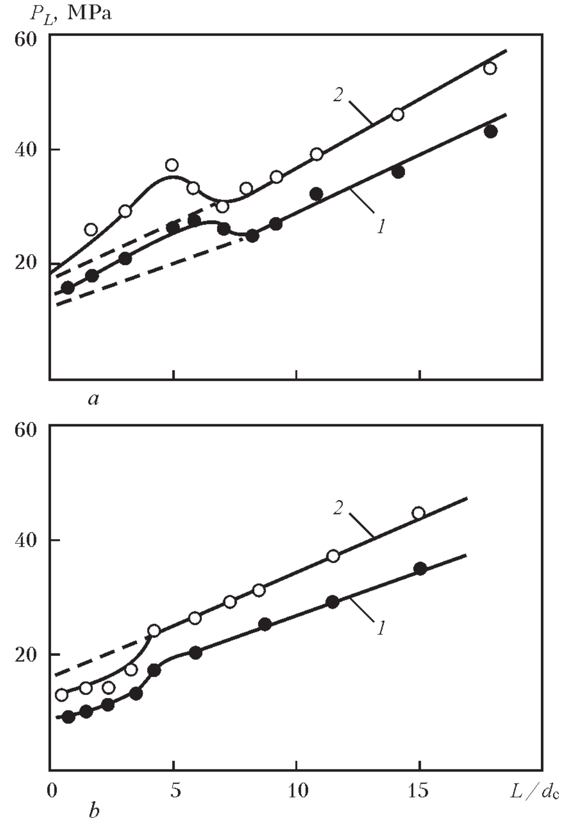

Figure 4. Dependence of total pressure gradient on channel L/d_c ratio at low-viscosity mixture flow rates of 1 (*1*) and 15.3 cm^3·s^{-1} (*2*) atnd d_c = 2 (*a*) and 6 (*b*) mm

Results, obtained in experiments with smaller diameter tanks, were stratified due to downward individual or group displacements of figurative points, reflecting lowering of flow resistance. Initial invariant flow curve is here stratified into two or three straight lines (by the number of capillaries used).

So, at D_R = 15 mm one result, which was obtained at d_c = 2 mm, shifted from invariant curve $P_0 = f(\dot{\gamma}_{sh})$; at D_R = 10 mm the results were stratified by three levels, appearing on three mutually parallel lines. Points reflecting the results obtained at d_c = 2 mm shifted to the lowest curve. Two results obtained at d_c = 4 mm moved to the middle curve (third one was obtained at d_c = 6 mm); two results obtained at d_c = 6 mm, appeared on the upper curve (third one was obtained at d_c = 4 mm).

As was noted above, stratification of $P_0 = f(\dot{\gamma}_{sh})$ flow curves is caused by relaxation pressure relieving and viscous heating of the jet, recorded on descending branches of the respective extrusion curves. Parallel displacement of flow curve logarithmic monologues is indicative of unchanged flow structure.

In low-viscosity N2 mixture the initial $P_0 = f(\dot{\gamma}_{sh})$ flow curve was also stratified but now not only by height, but also by inclination to the axis of shear rate gradients, particularly at D_R = 15 mm, that is indicative of the change of not only energy state of the system, but also of flow structure.

The path of $\tau = f(\dot{\gamma}_{sh})$ flow curves of S2 and N2 mixtures is even more complicated. This is related to a greater number of disturbing factors, the action of which depends not only on mode parameters, but also on the structure of mixtures being compared. For instance, in more structured N2 mixture, dissipative heating is less pronounced, but effects of near-wall slipping are more intensively manifested. It can be assumed that the stage of hydrodynamic, temperature and relaxation stationarity of the flow, not completed in pre-capillary zone of the measuring cell, shifts to the initial section of capillary cannel.

As follows from Figure 4, the total pressure gradient at gradual increase of reduced capillary length for low-viscosity mixture increases non-monotonically. At achievement of certain L/d_c value, relieving of accumulated elastic stress takes place, and rectilinear branch of $P_L = f(L/d_c)$ curve begins only after that. The smaller the capillary diameter, and the larger the mixture flow per second, the greater the pressure relief after the maximum has been achieved. No such anomaly is found in large-diameter capillaries. At passing of high-viscosity mixture even through capillaries with small channel cross-section, transition to proportional section of $P_L = f(L/d_c)$ curve also proceeds without any pressure surge, as in the lower graph of Figure 4 [4].

Even though the non-invariant path of flow curves reflects the presence of nonstationary phenomena in the deformation zone, this did not exclude the possibility of application of experimental results for calculation of rheological indices of electrode coating mixtures. Derived results were used in analysis of possible causes for emergence of the above phenomena.

On total pressure losses. At total pressure losses $P_L = P_0 + P_c$ its components P_0 and P_c are not only summated, but also significantly influence P_L value, due to their mutual influence. Mutual influence of complex function arguments is usually taken into account as their product, i.e. $\dot{\gamma}_R\dot{\gamma}_{sh}$. Proceeding from dimensional considerations, their geometrical mean is used (in our case, $\omega = \sqrt{\dot{\gamma}_R\dot{\gamma}_{sh}}$).

If $\dot{\gamma}_R = 2V_R/D_R$, $\dot{\gamma}_{sh} = 2V_R/d_c(D_R/d_c)^2$, then their product can be presented in the following form: $2V_R/D_{Rdc}(D_R/d_c)^2 = 4\beta^2V^2{}_R/D_Rd_c$. In logarithmic modification the expression for geometrical mean has the following form: $\lg\omega = \lg\sqrt{4\beta^2V_R^2/D_Rd_c}$.

It is seen that pressure losses for forming the pressure flow of coating mixture are a complex function of the speed of the plunger, injecting the mixture into the flow zone, container and capillary diameters, as well as their ratio determining the degree of capillary jet reduction. Under non-isothermal conditions the influence of viscous heating of the mixture makes an additional contribution, which is concentrated in the zone of the highest gradient of the shear rate.

Calculations showed that in our experiments, $\dot{\gamma}_R$ fraction in the product of $\dot{\gamma}_R\dot{\gamma}_{sh}$ varied in the range from 0.03 up to 21.5 %.

When $D_R \geq 30$ mm, the gradient of shear rate in the container is much smaller than that in the capillary, and its influence on P_L can be neglected. At $D_R \leq$ ≤ 10 mm the influence of shear rate gradient becomes quite noticeable, and it should be taken into account.

Figure 5 shows P_L dependence on ω in the pressure flow of S2 and N2 mixtures. In Figure 5, *a* (S2 mixture) three sections can be singled out. Left and right rectilinear sections are slow (creep) and fast steady-state flow, respectively. They are invariant to complex index of deformation mode. Located between them is the instability zone, resembling «stick-slip» flow mode. This kind of instability is often encountered in the technology of processing polymer materials and it is presented in the form of $\tau = f(\dot{\gamma}_{sh})$ or $\dot{\gamma}_{sh} = f(\tau)$ graphs [9], and in one of the first publications [10] devoted to it — in the form of $s = f(\tau)$, where s is the elastic, i.e. recoverable, strain.

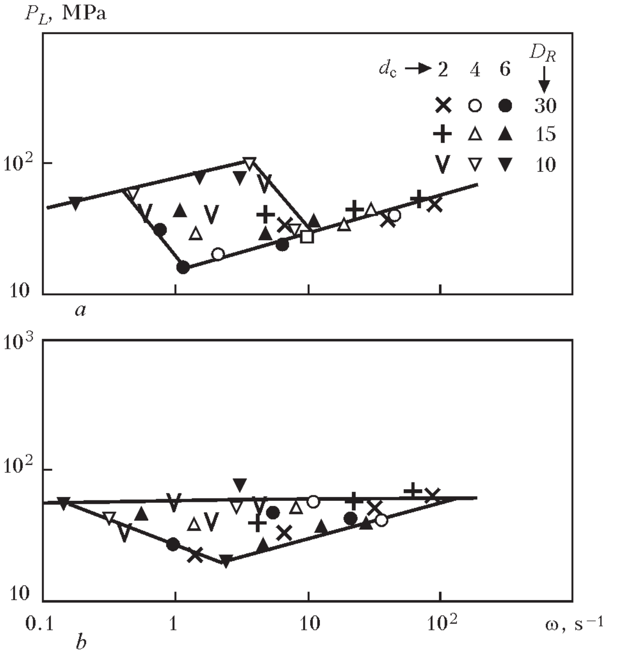

Figure 5. Dependence of total pressure losses in entrance zone and in capillary on ω value for S2 (*a*) and N2 (*b*) mixture

It is believed that flow instability, recorded in the form of flow mode transition from the upper to lower, less energy-intensive flow mode, is associated with competition of the elastic and viscous forces.

In Figure 5, *b* (N2 mixture) a rheogram of similar meaning has the form of a very narrow triangle, reflecting a noticeable scatter of results only in the case of application of small mixture containers. At D_R increase up to 15 mm scatter is reduced, and when $D_R = 30$ mm no scatter is found.

P_0 dependencies on ω have similar, but not as pronounced form.

In Figure 6 the results, obtained when studying S2 mixture, are represented by $Q = f(P_L)$ dependence, characterizing the process of electrode manufacturing in the extruding machines with hydraulic drive, without Q and P recalculation to consistent variables τ and $\dot{\gamma}_{sh}$. It is seen that in such an interpretation they are quite similar to pressure-flow characteristic, described in [1].

It can be explained as follows. At low pressures (at $Q < 1$ cm^3·s^{-1}) the coating is in the state of creep flow, in which the rate of its coagulation structure destruction

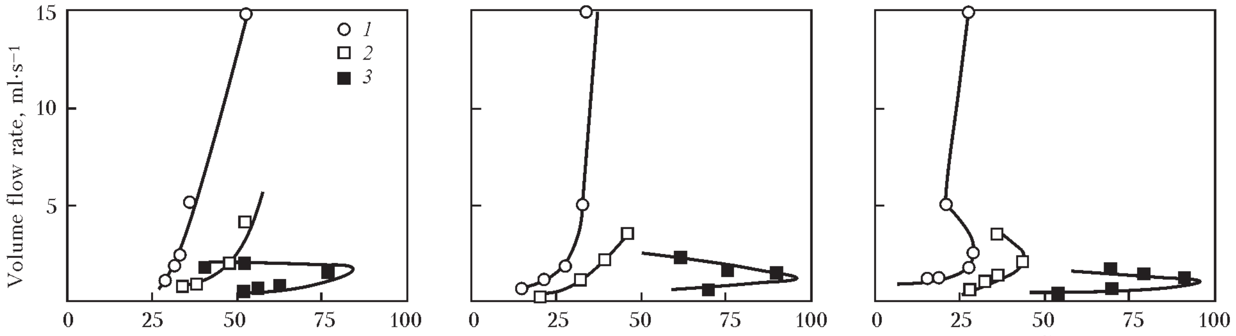

a *b* *c*

Figure 6. Pressure of mixture outflow from the container through capillary with channel diameter of 2 (*a*), 4 (*b*), 6 (*c*) mm and $L = 10d_c$ at $D_R = 30$ (*1*), 15 (*2*) and 10 (*3*) mm

is close to the value of elastic stress relaxation rate. The role of mixture self-heating at this flow stage is insignificant. The flow rate rises with P_L increase, and ever greater part of elastic stresses, not having enough time to relax, accumulates in the jet. After achievement of $Q = 1$ cm^3·s^{-1} the quantity of accumulated elastic energy is sufficient for flow stalling, which results in mixture structure breaking-up, its viscosity abruptly lowering, P_L value decreasing, and further acceleration of the jet proceeds at smaller pressure built-up. No doubt that it is exactly the jet temperature that plays an important role in facilitating the jet stalling under the influence of elastic stresses and after it. It, similar to the rate, promotes destruction of the structure and lowering of mixture viscosity in the flow. Elasticity indices only slightly change here. Viscosity decreases to a much greater extent, together with the mixture ability to smooth the adverse influence of mixture elasticity on pressure flow stability.

Results presented in Figure 5 were obtained at application of constant flow viscosimeter with step-like flow regulation and discrete increase of flow rate by variation of jet cross-section. As a result, temperature and rate conditions of the flow changed in a step-like manner from experiment to experiment, resulting in pressure-flow curves also taking an intermittent shape.

Influence of the method of mode regulation on flow curves. The mixture flow in pre-capillary zone is deformed by shear and tension. Shear deformation in the tank before the capillary $\dot{\gamma}_R$ can be presented by expression $\dot{\gamma}_R = \dot{\gamma}_{\text{sh}}/\beta^3$, where $\dot{\gamma}_{\text{sh}}$ is the gradient of shear rate in the capillary, and $\beta = D_R/d_c$ is the degree of jet reduction. Stretching of mixture flow, achieved during reduction and called Hencky strain, is presented as [11]:

$$\varepsilon \equiv \int_0^{+\infty} \dot{\varepsilon} dt = \int_{v_z(-\infty)}^{v_x(+\infty)} \frac{dv_z}{v_z} = \ln(\beta^2),$$

where $\dot{\varepsilon}$ is the tensile deformation rate.

In its turn, $\dot{\gamma}_{\text{sh}}$ is related to Deborah number (or, which is the same, to elastic turbulence criterion Re_e) by expression $\text{De} = \theta\dot{\gamma}_{\text{sh}}$.

We can see that the gradient of shear rate in the capillary and total extent of flow stretching are functions of one and the same argument β. Nonetheless, they react differently to its change. At one and the same β value, $\dot{\gamma}_R$ increase should promote greater shear destruction of the mixture structure in the capillary, whereas with β increase at De = const, greater stretching of the flow should be expected.

This follows from the results of work [11], in which β and De influence on pressure flow structure of the so-called Boger fluid, was studied. Its composition, as a mixture of three polymer solutions, features specific rheological properties, namely, its elasticity index ξ decreases essentially with increase of shear deformation rate, whereas shear viscosity η remains almost unchanged. This may be the reason, why an almost complete range of instabilities, encountered in industrial processing of polymers, namely cyclic, quasiperiodic and vortex-like flow with formation of incoming, pulsed or rotating vortex, was found when studying Boger fluid in the region of comparatively small changes of β and De.

Experiments were conducted with application of pneumatic capillary viscosimeter. To avoid undesirable vibrational impact of viscosimeter on investigation results, the controlled liquid was fed from the mixture tank to viscosimeter measuring cell through regulating valves, solely under the influence of static pressure. Circulation pump did not operate during measurements. To maintain the correct proportion of capillary and tank cross-sections, i.e. β, respective inserts were placed into the standard tank. The region of used flow modes was limited by Deborah number values in the range from 2 to 5, and that of β index — in the range from 2 to 6. Laser Doppler speedometer was used for jet speed measurement. Flow profile was recorded onto videotape by speed high-resolution TV camera. Experimental results are given in Figure 7. It shows the zones of instabilities revealed during the experiments.

As follows from the given graph, stable flow in the tank pre-capillary space is achieved in zone *1* at relatively low De values, and irrespective of Hencky strain magnitude used to create the flow.

Boundary of stability zone is limited by curve *2*. Its shape is indicative of the fact that at $\beta < 4$, flow instability is in place already at quite limited increase of Deborah number. Contrarily, if $\beta > 4$, flow modes can be used, which are characterized by ever higher De values, which are the higher, the greater β.

In our experiments, the range of β value variation is by an order of magnitude higher, and that of De is by 2 orders higher than in study [11]. Nonetheless, as follows from Figure 5, dimensions of instability zone are also quite limited, particularly for S2 mixture.

Let us assume that the regularities revealed when studying Boger fluid as a model of viscoelastic material can be transferred to electrode coating mixtures. Then, judging by the graph in Figure 7, the only method to go around the instability zone at extrusion of electrode coating mixtures is applying flow forming mode with high values of the degree of jet compression, i.e. working with tanks of large enough diameter.

At very high values of β, providing sufficient distance from the right, steeply ascending branch of boundary *2*, it will, apparently, be possible to increase the mixture deformation rate by the method of its ever faster injection by the plunger into the flow zone, without the risk of crossing the above boundary. For S2 mixture, this distance will be smaller than that for N2 mixture, in which this zone is of a much greater extent.

The validity of this assumption was verified by conducting experiments with S3 and N3 mixtures, extruded through holes in the locking disc of 2, 4 and 6 mm diameter from tanks of 30 to 90 mm diameter.

To reliably eliminate the influence of mixture column friction in the container on pressure losses, so-called back pressing was used, which is applied for the same purpose in metal extrusion technology [7]. In this case, the required series of measurements was performed, when extruding one billet in modes with flows, gradually increasing from experiment to experiment. The total range of changing of shear rate gradient was from 0.1 to 10^5 s^{-1}. Figure 8 gives the results.

It is seen that for high-viscosity S3 mixture the results are invariant in the entire range of $\dot{\gamma}_{sh}$ measurement. Therefore, at $D_R \geq 30$ mm its pressure flows are not prone to instability in a very broad range $(\dot{\gamma}_R)$.

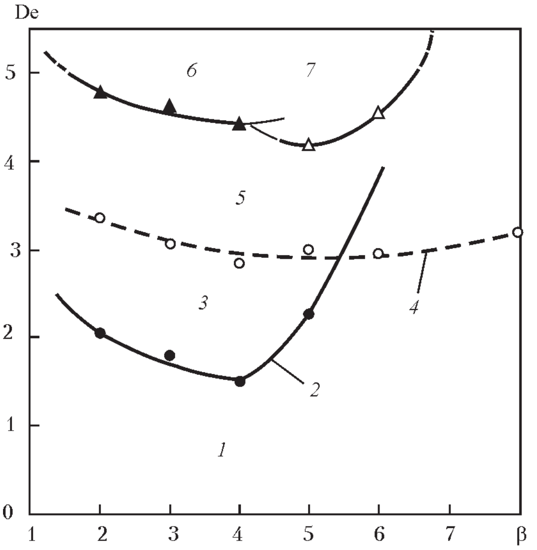

Figure 7. Kinds of flow instabilities in axially symmetric abruptly narrowing channel depending on ratio of the degree of flow contraction and elastic turbulence criterion: *1* — steady flow; *2*, *4* — boundaries of steady and vortex-like flow; *3*, *5*, *6* — cyclic, quasiperiodic, pulsed flow, respectively; *7* — rotating vortex [11]

Low-viscosity N3 mixture is prone to flow instability, caused by unrelaxed elastic stresses. Invariance of its $P_0 = f(\dot{\gamma}_{sh})$ flow curves is in place until D_R has reached 70 mm. The higher D_R, the smaller is the section of flow curve non-invariance. At $D_R = 70$ mm the non-invariance disappears.

The higher D_R, the smaller the flow index n_0, that is indicative of increase of the degree of Newtonian behaviour of the coating mixtures, and, therefore, of the increase of coating fluidity, as a result of greater destruction of their structure and resulting smaller accumulation of elastic energy in the flow. The greater the container cross-section, the lower is the flow rate, at which the curve reaches the saturation section. In S3 mixture the curves were eventually completely flattened.

Based on the data, which we have, the influence of initial viscosity of extruded material on jet temperature gradually decreases with increase of the degree of pressing, and at sufficiently high β values it becomes insignificant.

By the results of studying S3 mixtures, values of extrusion forces and pressures P_0 were calculated after the flow curve has reached the saturation section. Calculation results are given in Table 3. They show that at increase of container cross-section area 3.2 times, the pressing force increased just 2.2 to 2.8 times. Pressing pressure decreased to the greatest extent at maximum value of jet compression: 1.2–2.1 times at hole diameter $d_{C0} = 2$ mm. The greater d_{C0}, the weaker is the influence of β parameter on P_{C0}.

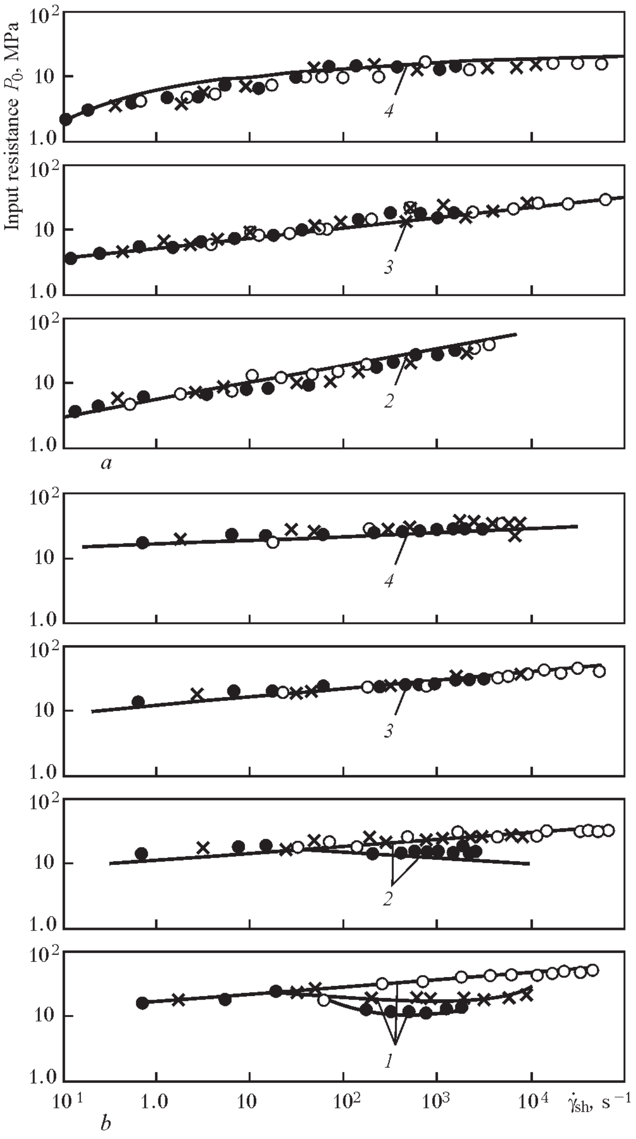

Figure 8. Pressure-flow characteristics of coating mixtures S2 (*a*) and N3 (*b*) obtained with application of mixture containers with D_R = = 50 (*1*), 70 (*2*), 90 (*3*) (*a*) and 30 (*1*), 50 (*2*), 70 (*3*), 90 (*4*) mm (*b*)

Characteristics of viscoelasticity of the compared coating mixtures. Figure 9 gives the dependence of S2 and N2 mixture relaxation period on shear rate gradient, and Figure 10 — the influence of shear rate gradient on shear viscosity and normal stress coefficients, as well as influence of average tensile deformation rate on longitudinal viscosity of S2 and N2 mixtures.

As follows from Figure 9, the compared mixtures are little different from each other by the influence of deformation rate on characteristic time (relaxation period θ). Values of $\dot{\gamma}_{sh}$, at which functions $\theta(\dot{\gamma}_{sh})$ cross horizontal θ = 1, are approximately the same ($\dot{\gamma}_{sh} \approx 40$–60 s^{-1}) for the compared coatings. However, scattering of experimentally found θ values is greater in N2 mixture than in S2 mixture. So, in S2 mixture ratio θ = η/*G* was close to 1 only in two experiments (β = 2.5, $\dot{\gamma}_{sh}$ = 50 s^{-1} and β = 2.5, $\dot{\gamma}_{sh}$ = 35 s^{-1}).

Table 3. Mixture extrusion characteristics

D_R, mm	d_{C0}, mm	Pressing force, t	P_0, MPa
50	2	47.8	0.330
	4	45.1	0.230
	6	34.3	0.180
70	2	98.2	0.255
	4	84.7	0.220
	6	69.3	0.180
90	2	101.7	0.160
	4	98.6	0.155
	6	95.4	0.155

Testing low-viscosity mixture revealed five such cases (β = 7.5, $\dot{\gamma}_{sh}$ = 40; β = 3.75, $\dot{\gamma}_{sh}$ = 40, β = 7.5, $\dot{\gamma}_{sh}$ = 40; β = 5, $\dot{\gamma}_{sh}$ = 50; and β = 2.5, $\dot{\gamma}_{sh}$ = 22 s^{-1}).

Works [2, 3] showed that θ = η/*G* = 1 is a necessary, but not always sufficient condition for formation of positive pulsed modes of mixture flow through the capillary. Whether they actually originate in the system of the tank and capillary, and whether they are in place for a long time after that, will be determined by ratio η/ξ, which is reached at moment θ = 1. As follows from Figure 10, mixture structure destruction results in $\eta(\dot{\gamma}_{sh})$ and $\xi(\dot{\gamma}_{sh})$ functions decaying with $\dot{\gamma}_{sh}$ increase, the second one more steeply than the first one, so that they cross each other. To the left of crossing point ξ > η, so that mixture viscosity is not capable of damping the influence of elastic stresses. Such ratio will be in place right down to zero flow rates, as $\xi_0 = (\eta_0)\theta$ [12]. To the right of the crossing point ξ < η, so that such an ability of the mixtures is the greater, the higher $\dot{\gamma}_{sh}$.

It also follows from Figure 10 that relative position of $\eta(\dot{\gamma}_{sh})$ and $\xi(\dot{\gamma}_{sh})$ straight lines is not the same, because of lower viscosity of N2 mixture. Therefore, the point of crossing of competing functions in S2 mixtures lies much more to the left than does $\dot{\gamma}_{sh}$ critical value (designated by vertical arrow), at which condition θ = 1 is fulfilled. Consequently, there is sufficient margin of $\eta(\dot{\gamma}_{sh})$ excess over $\xi(\dot{\gamma}_{sh})$, so as to counteract initiation of pressure flow pulsed mode.

In N2 mixture the point of crossing of compared functions $\eta(\dot{\gamma}_{sh})$ and $\xi(\dot{\gamma}_{sh})$ also lies to the left of $\dot{\gamma}_{sh}$ critical value, but much closer to it. As a result, excess of damping function $\eta(\dot{\gamma}_{sh})$ over $\xi(\dot{\gamma}_{sh})$ function, capable of causing elastic disturbances, can be regarded to be sufficient to prevent the possibility of pulsed flow initiation, but not always enough for completely suppressing such a possibility. This is confirmed by the shape of extrusion curves, partial relaxations of elastic stresses in the form of pressure relieving, as well as essential scattering of results.

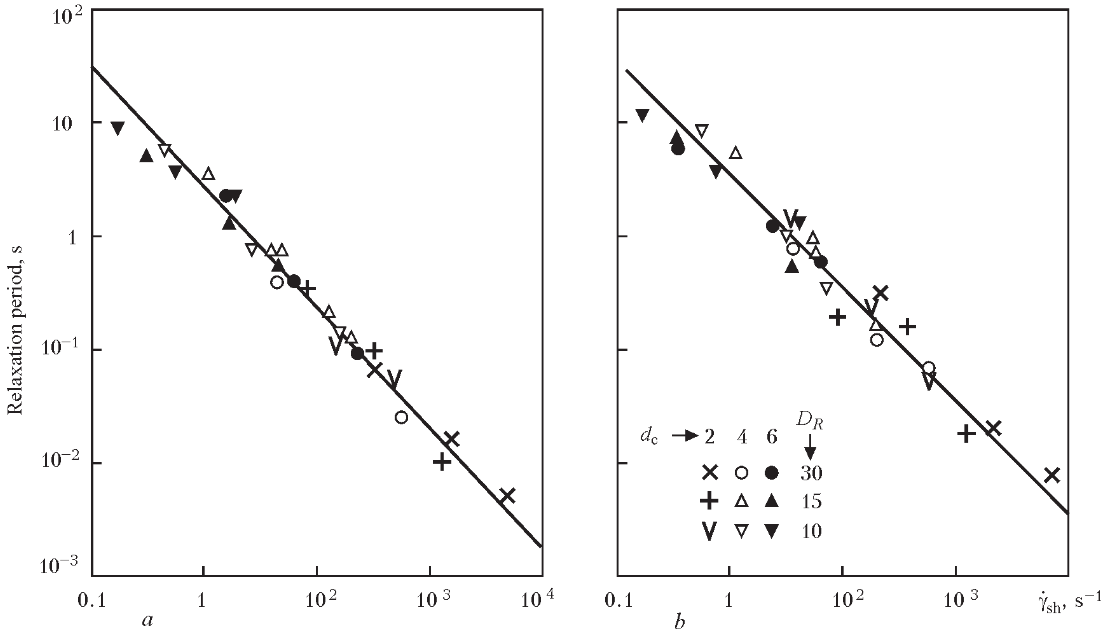

Figure 9. Dependence of relaxation period of coating mixtures S2 (*a*) and N2 (*b*), extruded from tanks with D_R = 10, 15 and 30 mm through capillaries with d_c = 2, 4 and 6 mm, on shear rate gradient

Accumulation of elastic stresses is accompanied by reduction of the angle of natural convergence of flow α_0. Figure 11 shows the influence of the criterion of elastic turbulence in flows of S2 and N2 mixtures on α_0 value. It is seen that viscous mixture is characterized by much smaller scatter of elastic turbulence characteristic and associated α_0 value, compared to the low-viscosity mixture. This is confirmed by statistical estimate of the obtained results given in Figure 12.

Thus, it is anticipated that approaches applied for achievement of similar purposes in the technology of polymer material extrusion can be beneficial in terms of increasing flow stability of mixtures, designed for coating welding electrodes. They are based on the concepts of existence of an inextricable

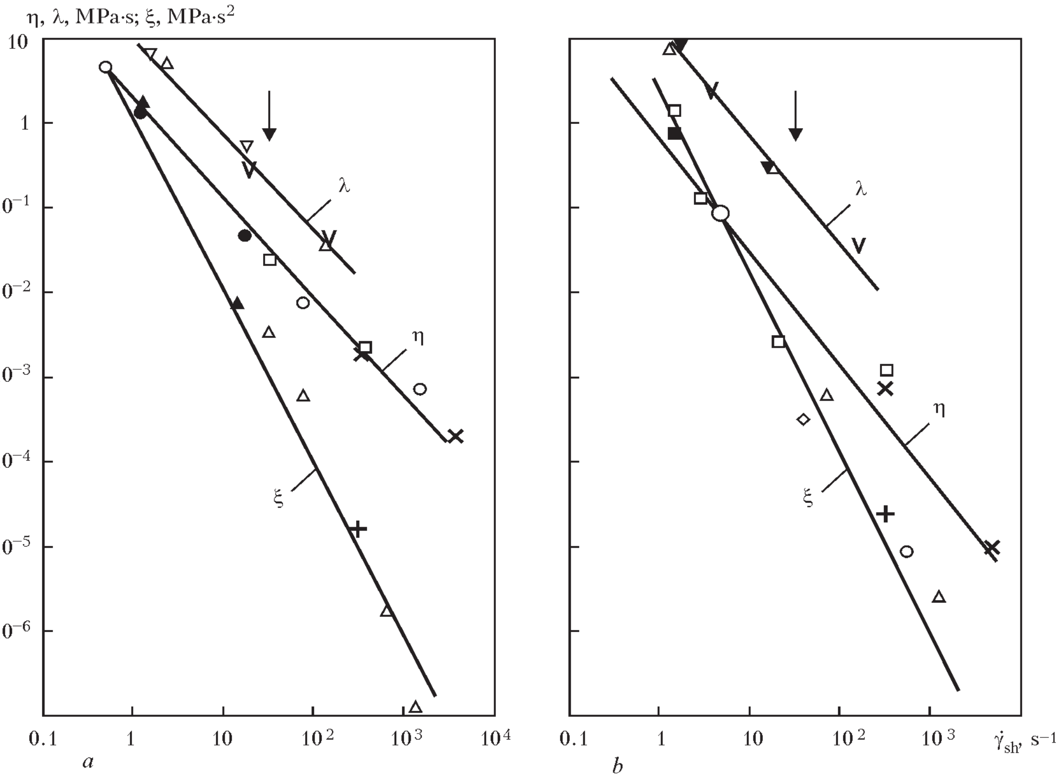

Figure 10. Dependence of η, ξ and λ on shear and longitudinal flow for S2 (*a*) and N2 (*b*) mixture (arrows indicate $\dot{\gamma}_{sh}$ value, at which condition θ =1 is fulfilled)

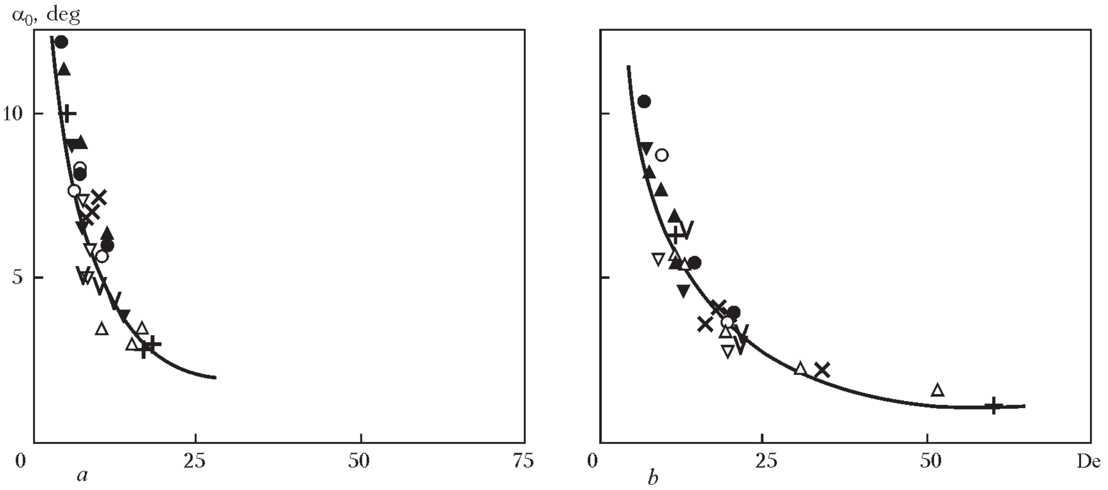

Figure 11. Influence of Deborah number on angle of natural convergence of coatings mixtures S2 (*a*) and N2 (*b*) extruded from tanks with D_R = 10, 15 and 30 mm through capillaries with d_c = 2, 4 and 6 mm

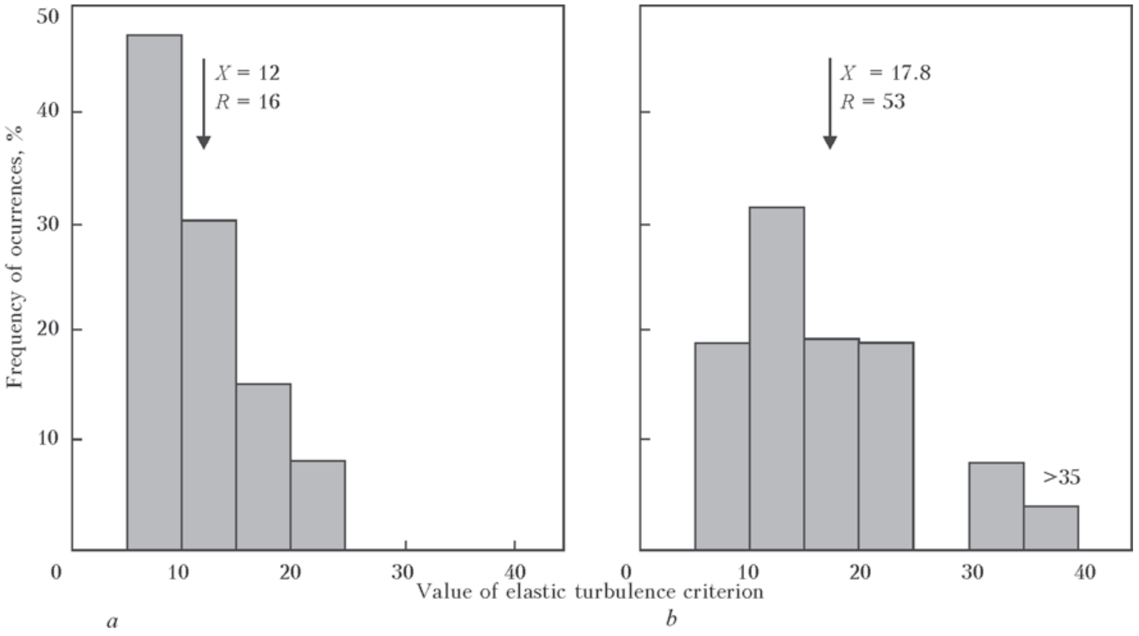

Figure 12. Statistical distribution of Deborah number as characteristic of angle of natural convergence of pressure flows of coating mixtures S2 (*a*) and N2 (*b*) extruded from tanks with D_R = 10, 15 and 30 mm through capillaries with d_c = 2, 4 and 6 mm: *X* — average sample value; *R* — sampling scope

link between the two effects, specific for polymer systems, namely appearance of the so-called viscosity anomaly at flowing with increase of deformation rate, on the one hand, and generation of normal stresses, caused by accumulation of recoverable strains, on the other. Normal stresses in a certain range of rather slow deformations are capable of provoking various kinds of flow instabilities. Their appearance can be prevented, if normal stresses are damped by system viscosity. Such a possibility exists due to the fact that effective viscosity decreases slower with increase of deformation rate than does the coefficient of normal stresses [12].

Conclusions

1. Model of continuous-flow stepped channel simulating the conditions of electrode coating mixture flow in measuring cell of capillary viscosimeter or forming head of electrode extrusion machine was used to study the structure and rheological characteristics of non-isothermal mixture flow for low-hydrogen electrodes. Mixtures, one with viscous, and another one with low-viscosity liquid glass, differed significantly by the degree of structuredness, viscosity and elasticity ratio and resistance to instability appearance in pressure flows.

2. It is established that the compared mixtures react differently to capillary testing modes, which were adjusted by changing the flow rate or degree of jet reduction. Mixture with low-viscosity glass is more structured and, therefore, it is less prone to dissipative heating than its viscous analog, as part of the energy spent for flowing is consumed by structure

destruction. On the other hand, the above-mentioned methods of flow mode regulation are inadequate to each other, either: speed increase by jet reduction causes its lower heating than does increase of mixture flow rate, irrespective of the method of reduction; be it by increase of tank cross-section or reduction of capillary cross-section.

3. Competition of elastic and viscous elements provokes all kinds of irregularities in coating mixture pressure flows. They are revealed by visualization (as a change of flow pattern), on recorded extrusion curves (as flow irregularities and stalling), on flow curves (as different degree of their non-invariance) and as a change of total pressure losses, caused by elastic stress relaxation. Here, elasticity can be regarded as a provoking, and viscosity — as a damping factor. Viscous heating increases the probability of instability development, as, similar to flow rate, it lowers mixture viscosity, while breaking up its structure.

4. Tank and capillary are the sites of instability development. In the work, it is proposed to allow for the role of each stage in appearance, for instance, of instability of total pressure losses in the tank and the capillary, in the form of the function of complex argument ω as geometrical mean of gradients of shear rate in the tank and in the capillary. Such an approach allowed establishing the critical range of pressure flow modes, within which function $P_L(\omega)$ is exclusively non-invariant. Beyond this range $P_L(\omega)$ flow curves have an invariant form.

5. Ratio of viscous and elastic properties in the compared mixtures should be evaluated by comparing shear viscosity η with modulus of elasticity G, on the one hand, and shear viscosity with the coefficient of first difference of elastic stresses ξ, on the other hand. Equality of η and G characteristics in the first ratio is the mandatory condition for appearance of disturbances in the capillary flow. Whether they actually arise and will be prolonged, is determined from the value of η/ξ ratio at moment of time, when $\eta = G$. If $\eta > \xi$, the disturbances, even the arisen ones, for instance, in the form of flow pulsations, cannot be prolonged as dynamic viscosity damps elasticity, represented by coefficient ξ of similar meaning. Values of coefficients η and ξ decrease with increase of shear rate gradient, steeper for the second of them than for the first one. In the graphic form $\eta(\dot{\gamma}_{sh})$ and $\xi(\dot{\gamma}_{sh})$ functions cross. To the right of the crossing point, condition $\eta > \xi$ is fulfilled to the greater extent, the higher $\dot{\gamma}_{sh}$, and even when $\eta = G$, the arisen disturbance will be short-term, or will be implemented in the form of individual jet stalling. To the left of crossing point of $\eta(\dot{\gamma}_{sh})$ and $\xi(\dot{\gamma}_{sh})$ functions, condition $\eta < \xi$ is satisfied, and this opens up broad possibilities for emergence of prolonged disturbances.

6. Kinds and, particularly, intensity of disturbances in pressure flows of coating mixtures depend on the method of their speed regulation: by jet reducing β or by the rate of mixture injection into zone of reduction by the plunger. Increase of β, owing to large tank diameters together with smaller heating of the mixture, weakens the influence of peripheral elastic zones on pre-capillary space, in which the jet forms, lowers the level of stored elastic energy and, therefore, the flow curve invariance. Moreover, the share of material deformation by tension is increased that facilitates maintaining the flow stability. The larger the tank diameter, the lower the pressure required for ensuring a stable pressure flow of coating mixtures.

7. Coating mixtures based on low-viscosity liquid glass are more prone to emergence of disturbances in pressure flows than their viscous analogs.

1. Sokolov, E.V. (1950) Electrodes with quality coating and their production. *Avtogen. Delo*, **11**, 26–29.
2. Marchenko, A.E. (2014) Thickness difference of electrode coating caused by elastic turbulence of electrode compounds under the conditions of nonisothermal pressure flow. *The Paton Welding J*., **6/7**, 177–189.
3. Marchenko, A.E. (2014) Effect of charge grain composition on rheological characteristics of coating mixtures for low-hydrogen electrodes. *Ibid*., 163–171.
4. Marchenko, A.E. (2015) Examination of viscoelastic behavior of electrode coating mixtures in the state of pressure flow through cylindrical forming orifices. In: *Proc. of St.-Petersburg Int. Sci.-Techn. Conf. on Welding Consumables* (15–17 Oct. 2015), 79–89.
5. Marchenko, A.E., Gnatenko, M.F. (1980) *Specifics of flow of electrode coating mixtures, detected by capillary plastometer*: Inform. Doc. of SMEA, Issue 1, 106–117.
6. Marchenko, A.E. (2015) About thermal conditions, generated by viscous heating of electrode coating mixture in the zone of pressure flow formation. In: *Proc. of St.-Petersburg Int. Sci.-Techn. Conf. on Welding Consumables* (15–17 Oct. 2015), 65–78.
7. Perlin, I.L. (1964) *Theory of pressing of metals*. Moscow: Metallurgiya.
8. Yankov, V.I., Glot, I.O., Trufanova, N.M. et al. (2010) *Flow of polymers in die holes. Theory, calculation, practice*. Moscow, Izhevsk.
9. Georgios, G. (2005) Stick-slip instability. In: *Polymer melts instabilities, control and understanding*. N.Y.: Dekker, 176–221.
10. Philippoff, W., Gaskins, F.H. (1958) The capillary experiment in rheology. *Transact. Soc. Rheol. II*, 263–284.
11. McKinley, G.H., Raiford, W.P., Brown, R.A. et al. (1991) Nonlinear dynamics of viscoelastic flow in axisymmetric abrupt contractions. *J. Fluid Mech*., **223**, 411–456.
12. Vinogradov, G.V., Malkin, A.Ya. (1977) *Rheology of polymers*. Moscow: Khimiya.

Received 30.11.2015

INFLUENCE OF THERMOPHYSICAL PROPERTIES OF CORES OF SELF-SHIELDING FLUX-CORED WIRES ON WELDING AND TECHNOLOGICAL PROPERTIES

A.S. KOTELCHUK
E.O. Paton Electric Welding Institute, NASU
11 Kazimir Malevich Str., 03680, Kiev, Ukraine. E-mail: office@paton.kiev.ua

In the paper the comparison of effectiveness of gas shielding of molten metal in welding with self-shielding flux-cored wires of carbonate-fluorite type was carried out considering the properties of their cores investigated by thermal analytical methods. It is shown that to improve reliability of gas shielding in welding using such wires it is important not only to ensure generation of large volume of shielding gases at thermal destruction of the wire core, but also to control this process, providing sufficient gas evolution at all stages of heating and melting of the wire. Using the data of differential scanning calorimetry of charge of the flux-cored wire of carbonate-fluorite type containing lithium carbonate, the evaluation of heat losses for heating and melting of powder core, accompanied by the development of energy-intensive processes of thermal destruction of core components, was carried out. It is proposed to limit the carbonate content in the wire at the level of 1–2 % of its weight, that allows keeping the values characterizing the stability of welding process at an acceptable level and, thus, providing a sufficient gas shielding of metal and good separation of slag crust. The control of thermochemical reactions in the core is achieved by selecting its necessary composition to ensure a favorable melting of flux-cored wire and electrode metal transfer to the weld pool. 5 Ref., 3 Tables, 5 Figures.

Keywords: *arc welding, flux-cored wire, melting and metal transfer stability, thermal comprehensive analysis, thermophysical properties, welding and technological characteristics*

Flux-cored wires for electric arc welding combine the advantages of two processes: welding using solid wire in shielding gases and manual arc welding with coated electrodes. As a rule, the flux-cored wires are composed of the components for alloying and deoxidation of weld metal, gas- and slag-forming components that provide protection of molten metal, its refining and the required chemical composition of weld metal, as well as easily ionizing additions, stabilizing the arc discharge to ensure a high efficiency of the process [1, 2].

The welding and technological properties of flux-cored wires determine the possibilities of their application for welding of different metal structures in various conditions, such as at the open areas exposed to wind (or uncontrollable air flows). These properties, in their turn, are mainly determined by the composition of flux-cored wires filler (core). The design of the composition of core allows controlling the processes of molten electrode metal transfer and its protection from exposure to the surrounding atmosphere (which is important, in particular, in using self-shielding flux-cored wires), as well as formation of weld metal and ensuring its required properties.

Self-shielding flux-cored wires represent a welding consumable, the application of which does not require shielding gas supply (for example, when performing welding and erection works, where the supply of shielding gas is complicated). In the self-shielding flux-cored wires of carbonate-fluorite type the protection of transferred molten electrode metal and weld pool from harmful interaction with oxygen and nitrogen of ambient air, that can lead to porosity and deterioration of mechanical properties of weld metal, is realized by thermochemical reactions of decomposition of carbonates and fluorine-silicates being components of the core of such wires, with the formation of protective atmosphere.

During welding under the site conditions, where the welding zone is inevitably exposed to uncontrollable air flows, there is a very urgent problem of reliability of molten metal protection. In this case, the effectiveness of protection in practice, as accepted, is evaluated as to the possibility of elongation of the arc ΔU_a [2, 3]:

$$\Delta U_a = U_a^{\max} - U_a^{\min}, \tag{1}$$

where $U_a^{\min}$ is the minimum arc voltage, at which welding for the preset current (electrode wire feed rate) is possible, and $U_a^{\max}$ is the maximum arc voltage, at which it is possible to produce solid welds, i.e. the

Table 1. Gas-forming composition of flux-cored wires

Gas-forming components	Content of components, wt.%							
	In wire				In core			
	KF1	KF2	KF3	KF4	KF1	KF2	KF3	KF4
$CaCO_3$	2.8	2.6	3.7	3.9	16.1	16.2	22.4	21.2
Na_2CO_3	2.1	1.6	–	1.5	12.1	9.9	–	8.1
Na_2SiF_6	–	1.2	2.1	2.3	–	7.5	12.8	12.5

welds where the pores caused by supersaturation of metal with nitrogen are absent.

Using the procedure described in work [3], the evaluation of resistance of the formed gas shielding in welding with self-shielding flux-cored wires of carbonate-fluorite type of 2.2 mm diameter against the effects of wind in the welding zone was carried out. The compositions of gas-forming part of cores of the wires are shown in Table 1.

As the slag-forming components fluorite (CaF_2), rutile (TiO_2), perovskite ($CaTiO_3$), wollastonite ($Ca_3(Si_3O_9)$) and alumina (Al_2O_3) were also introduced to the wire core. Deposition of the reference beads on low-alloyed steel plates were carried out at welding current of 280 A. All the four wires showed good shielding properties in welding under the influence of the wind flows in the zone of arcing at speed of up to 5 m/s. However, the deterioration in the efficiency of gas shielding of molten metal formed by them (reduction in the allowable elongation of the arc) with increase in wind speed higher than 5 m/s is more noticeable in flux-cored wires KF1 and KF3 than in KF2 and KF4. The gas analysis of specimens, cut from the central part of the six-layer deposits, showed that with increasing the wind speed in the welding zone the nitrogen content in weld metal is increased, moreover, the rate of increment of nitrogen content is comparable to the rate of narrowing the range of operating voltages at the arc (Figures 1 and 2).

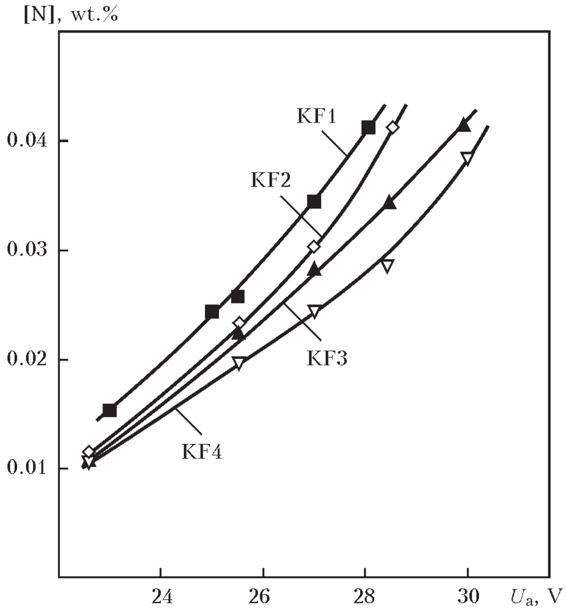

Figure 1. Effect of arc voltage on nitrogen content in metal deposited using flux-cored wires of carbonate-fluorite type

The explanation for this fact can be found through investigation of thermophysical properties of models of wire cores at the dynamic heating to temperatures of about 1500 °C, using the methods of complex thermal analysis, including thermal gravimetric, differential thermal gravimetric analysis and differential scanning calorimetry, as well as mass spectroscopy of the evolved gases [4].

Such investigations were conducted using combined thermal analyzer TGA/ DSC Q600 STD (TA Instruments, USA) and mass spectrometer VG ProLab (Thermo Scientific Fisher, Great Britain). Before conducting the investigations all the necessary calibrations of thermal analyzer were performed in accordance with the instructions: temperature, heat flow and mass signal in the entire investigated temperature range. The investigations were carried out in the 50 ml/min air flow at linear heating rate of 10 °C/min. The mass of specimens in all the experiments was about 20 mg. For investigations ceramic crucibles (made of Al_2O_3) were used.

During thermal destruction of core materials the gases are evolved, different as to their molecular mass (in particular, SiF_4, CO_2), therefore, the data of thermal gravimetric analysis do not fully reflect the volumes of the evolved shielding gases. As far as 1 mole of any gas at the identical conditions (pressure and temperature) occupies the same volume, then it seems

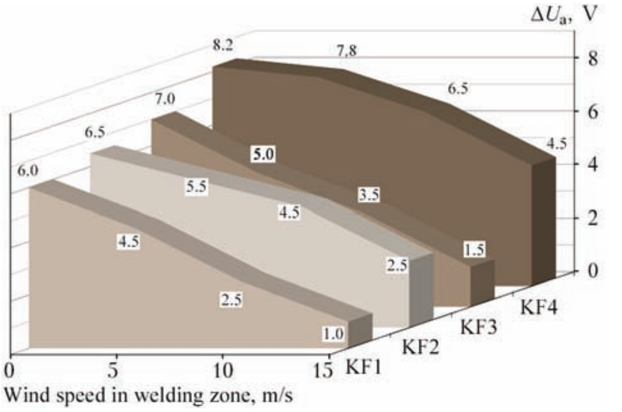

Figure 2. Possibility of arc elongation $\Delta U_a = \Delta U_a^{max} - \Delta U_a^{min}$ during welding using self-shielding flux-cored wires of carbonate-fluorite type exposed to wind flow

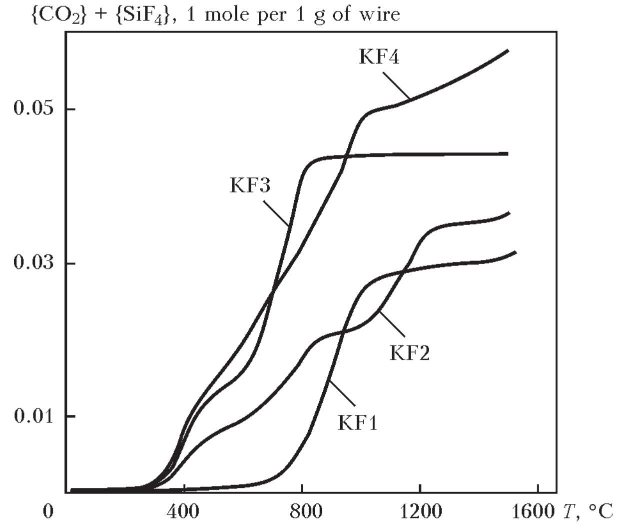

Figure 3. Total amount of shielding gases (CO_2, SiF_4) evolved from the cores of flux-cored wires of carbonate-fluorite type at continuous heating at 10 °C/min rate of 1 g of flux-cored wire

to be rational to evaluate the formation of gas shielding during thermal destruction of core components of flux-cored wire in molar volumes. During calculations of molar volume of shielding gases the compositions of wires were taken into account. The data on temperature dependences of molar amounts of shielding gases formation, referred to the mass of wire, are shown in Figure 3. These data can confirm that shielding properties of flux-cored wire composition during welding in the absence of external influence of air flows on the welding zone directly depend on the volume of shielding gases formed during heating and melting of core.

So, the best characteristics of the four considered wires are provided by the composition of wire KF4, and the worst — by KF1. But this approach cannot explain the difference in composition shielding characteristics of wires KF3 and KF2 during welding under the influence of air flows. At speed of air flow higher than 5 m/s, wire KF2 is characterized by a more stable protection to the effects of wind than KF3, although the volume of shielding gases formed during heating and melting of the KF3 core is higher than that of KF2. The formation of protective atmosphere during heating the charge of KF3 occurs in a comparatively narrow temperature range.

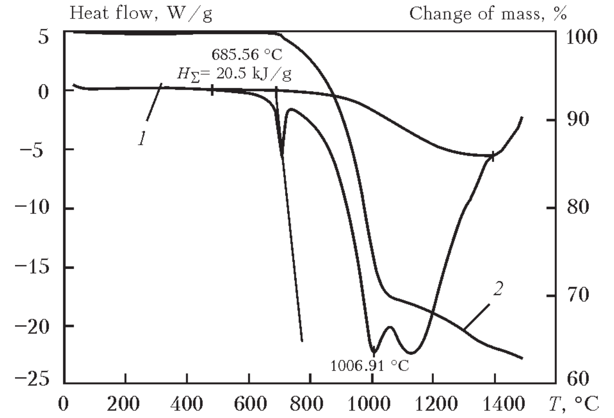

Figure 4. Thermal analysis of model charge of flux-cored wire, containing Li_2CO_3, using methods of differential scanning calorimetry and thermal gravimetry: *1* — heat flow; *2* — change of mass

Considering the quasi-steady state of temperature distribution during heating of flux-cored wire at the stickout, it results in narrowing the sizes of gas formation zone in the stickout. The bulk of shielding gases for the KF1 core (over 75 wt.%) is evolved in the temperature range from 600 to 800 °C, and the whole process of gas formation is completed already before reaching 900 °C. For the KF2 charge a more uniform distribution of shielding gases (CO_2 and SiF_4) is characteristic in the temperature range from 400 to 1400 °C, that is predetermined by using a mixture of carbonates and a higher share of fluxes in the charge. Before melt is formed in the charge composition, sodium carbonate facilitates the beginning of dissociation reaction of calcium carbonate, and after formation of the melt it inhibits the evolution of shielding gases (see Figure 3).

Thus, the obtained data evidence that to ensure the high efficiency of gas shielding during welding with self-shielding flux-cored wires it is important not only to ensure the generation of a large amount of shielding gases, but also to control the processes of gas evolution to create a protective atmosphere at all stages of heating and melting of the flux-cored wire, electrode metal transfer and weld pool formation.

The heat losses for heating and melting of powder core can significantly affect the welding and technological properties of the flux-cored wire [1]. The evaluation of these losses can be carried out using the data of differential scanning calorimetry on the example of charges of flux-cored wires of carbonate-fluorite type containing lithium carbonate (Figure 4). During heating the model charge of flux-cored wire the heat is consumed on melting and thermal dissociation of Li_2CO_3 leading to formation of Li_2O in the slag phase and evolution of CO_2 gas phase. Moreover, the total thermal effect H_Σ (see Figure 4) can reach 20.5 kJ/g of the model core.

These data allow evaluating the heat balance during heating and melting of flux-cored wire, the core of which contains lithium carbonate. Thus, for example, in welding using flux-cored wire of 1.6 mm diameter, containing 1 wt.% of Li_2CO_3, at $U_a \approx 24$ V and $I_w \approx 250$ A ($v_{w.f} \approx 3.5$ m/min) up to 2.4 % of input energy will be consumed for heating, melting and thermal dissociation of core components, resulting in a noticeable deterioration of welding and technologi-

Table 2. Statistical data on welding process using pilot self-shielding flux-cored wires

Li_2CO_3 content in wire, wt.%	Arc voltage			Welding current			Short-circuit average time, μs	Frequency of short-circuits, s^{-1}
	Mean value, V	Standard deviation, V	Variation coefficient	Mean value, A	Standard deviation, A	Variation coefficient		
0	23.1	2.3	0.10	289.1	28.0	0.10	112.5	4
1	21.8	1.6	0.07	296.4	24.9	0.08	159.7	15
2	22.9	2.4	0.10	283.0	36.0	0.15	225.0	26
3	22.0	3.8	0.17	294.5	49.4	0.17	532.0	75

Table 3. Values of technological properties of flux-cored wires containing different amounts of carbonates in the core

Li_2CO_3 content in wire, wt.%	Arc voltage, V	Welding current, A	Losses for spattering, %	Separation of slag crust, point	Presence of defects
0	19–22	220–270	5.1	3	No
	23–26	250–300	4.8	3	Pores
1	19–22	220–250	5.2	5	No
	23–26	250–300	4.9	5	Same
2	19–22	250–300	7.2	5	»
	23–27	310–350	6.9	5	»
3	18–22	240–290	11.3	4	»
	22–24	300–350	9.3	4	»

cal properties, i.e. decrease in stability of the arc and increased spattering of the electrode metal.

The evaluation of welding and technological properties of self-shielding flux-cored wire with different content of lithium carbonate in the core was carried out on the example of 1.6 mm diameter wire of a tubular design. Welding was carried out at direct current of straight polarity. The results of statistical processing of the values of current and voltage of arc welding using these flux-cored wires obtained applying the system with high-speed analog-to-digital converters for monitoring and processing of electrical signals of arc welding at frequency of 50 kHz [5], are shown in Table 2 and Figure 5.

The obtained data show that the content of lithium carbonate in the wire core does not affect the technological characteristics of the process significantly, when its content amounts up to 2 % of wire mass. The exceeding of this value leads to increased spattering of the electrode metal (Table 3).

In general case, the introduction of carbonates facilitates the improvement of separation of slag at the edges of weld metal. This improvement is explained by the influence of oxides, formed during decomposition of carbonates, on homogenization of the slag. The increase in the content of carbonates in the wire core to higher than 2 wt.% does not improve the gas shielding significantly, but leads to significant changes in the chemical composition of the weld metal, i.e. to somewhat reduced content of deoxidizing and alloying elements in the weld metal, and the oxygen content increases.

Thus, it can be concluded that it is rational to limit the carbonate content in the wire at level of 1–2 % of its mass, that allows preserving the values, characterizing the stability of welding process at the acceptable level, and providing effective gas shielding of metal and good separation of slag crust.

In conclusion it should be noted that investigations of physical and chemical properties of powder materials and their mixtures, which model the cores of flux-cored wires, carried out using the methods of complex thermal analysis (differential thermal, thermal gravimetric, differential thermal gravimetric analysis and scanning calorimetry), as well as the method of mass spectroscopy of gas phase during dynamic heating up to the melting point of steel, showed that the process of heating the mixtures of the powder materials, containing gas- and slag-forming components together with metal powders, is accompanied by proceeding of dissociation reactions with gas evolution, oxidation,

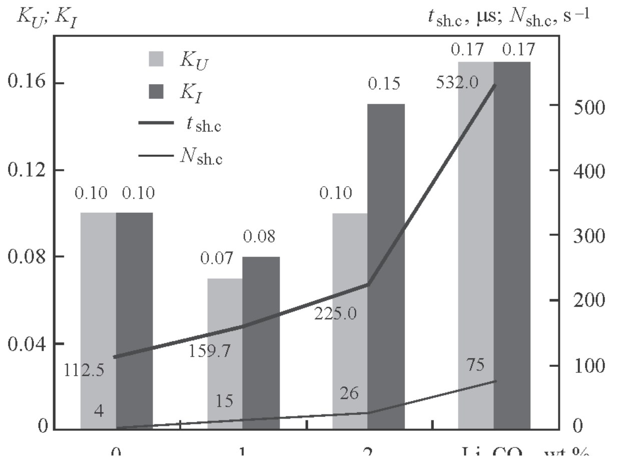

Figure 5. Variation coefficients of arc voltage K_U and welding current K_I, average time $t_{sh.c}$ and frequency $N_{sh.c}$ of short circuits in welding using pilot self-shielding flux-cored wires depending on lithium carbonate content in the wire core

melting of mixtures and formation of primary melt of metal and slag phases. The formation of slag melt already at the stage of heating the powder core before melting of the wire sheath and evolution of gases (CO_2, SiF_4) facilitates the improvement of shielding features of flux-cored wires in welding without additional protection. The thermal effects of thermochemical reactions, which accompany the process of heating, run simultaneously (endothermal processes of destruction, melting and exothermal oxidations and formations of complex compounds). The control of these reactions due to the changes in the mixture composition allows regulating the rate of core melting, facilitates the formation of favorable characteristics of flux-cored wire melting and electrode metal transfer to the weld pool.

As the components of flux-cored wire, which reduce the temperature of beginning of fusion of the core, it is rational to use the metal powders based on aluminum and its alloys, non-metallic slag- and gas-forming components such as carbonates, oxides and fluorides of alkali metals.

1. Widgery, D. (2005) Tubular cored wire welding. In: *New developments in advanced welding*, 21–39. Cambridge: Woodhead Publ.
2. Pokhodnya, I.K., Yavdoshchin, I.R., Shvachko, V.I. et al. (2004) *Metallurgy of arc welding. Interaction of gases with metals*. Ed. by I.K. Pokhodnya. Kiev: Naukova Dumka.
3. Shlepakov, V.N., Suprun, S.A., Kotelchuk, A.S. (1990) Estimating of the characteristics of flux-cored wire welding under the wind flow effect. In: *Proc. of Int. Conf. on Welding under Extreme Conditions* (Helsinki, Finland, 4–5 Sept., 1989), 171–179. N.Y.: Pergamon Press.
4. Shlepakov, V.N., Kotelchuk, A.S. (2011) Investigation of thermochemical characteristics of mixtures of dispersed materials by differential thermal analysis methods. *The Paton Welding J.*, **12**, 13–16.
5. Ponomarev, V., Al-Erhayem, O., Apps, R.L. et al. (1997) *Arc welding process statistical analysis. Methodical approaches, analysis conceptions, experiences*: Manual-guide. DTU-Helsingor: JOM-Institute.

Received 29.10.2015

INVESTIGATION OF CONDITIONS FOR PROVIDING LOW CONTENT OF DIFFUSION HYDROGEN IN WELDING USING ELECTRODES OF BASIC TYPE

A.P. PALTSEVICH
E.O. Paton Electric Welding Institute, NASU
11 Kazimir Malevich Str., 03680, Kiev, Ukraine. E-mail: office@paton.kiev.ua

In this work the mechanisms for prevention of hydrogen absorption at the participation of CaF_2 and SiO_2 in submerged arc welding and welding with covered electrodes resulting in formation of HF, based on thermodynamic calculations, are considered. The formation of SiF_4 and HF was experimentally established in the air samples in the arc zone. In the opinion of researchers, HF is a thermally resistant compound in the arc gap and, thus, it facilitates the decrease of P_H in the arc zone. As the criterion for the efficiency of this mechanism the reduction and elimination of weld porosity in submerged arc welding were served. The further works and accurate data on thermal properties of HF, H_2, H_2O, N_2 and other gases at high temperatures, as well as the results of experiments with measurement of $[H]_{diff}$ content in welds showed that the above-mentioned mechanism does not provide the ultra-low $[H]_{diff}$ content. In the present work the investigations on the influence of CaF_2 and moisture content in the coating on $[H]_{diff}$ content were carried out, the content of water impurities was determined in the components of electrode coatings at heating up to 1000 °C. It is shown that the preliminary heat treatment of the components provides reduction of the level of $[H]_{diff}$ to ≤ 3–2 ml/100 g depending on the coating composition. 19 Ref., 3 Tables, 5 Figures.

Keywords: *arc welding, covered electrodes, potential hydrogen, diffusion hydrogen, silicon fluoride, hydrogen fluoride, dissociation of gases, components of electrode coatings, chromatographic analysis of hydrogen, investigations*

Hydrogen is the undesirable impurity in the weld metal, because it leads to formation of porosity and is one of the causes for cold crack formation in welded joints of high-strength low-alloyed steels.

In accordance with the IIW standards, the electrodes are classified according to the content of hydrogen introduced to the deposited metal or diffusion hydrogen $[H]_{diff\ d.m}$: up to 5 ml/100 g as very low, up to 10 ml/100 g — low hydrogen, up to 15 ml/100 g — middle hydrogen ones. In accordance with the AWS standards, the levels of $[H]_{diff\ d.m}$ amount to 2, 4, 8, 16 ml/100 g. The following methods of analysis are used: according to standard ISO 3690-2000E, mercury-vacuum (primary) chromatography (express) due to reduced time of the analysis to 6 h at temperature of 150 °C; according to standard ANS/AWS-A.4–93, chromatographic analysis for 6 h at 150 °C. It should be noted that the use of alcohol or glycerin samples does not give a real idea of the $[H]_{diff\ d.m}$ content, because these procedures give lowered results.

The problem of providing the level of $[H]_{diff\ d.m} <$ < 5 and, moreover, ≤ 3 and 2 ml/100 g is not solved completely and is urgent. A number of measures taken to the electrodes used in welding, namely recalcination including also at elevated temperature, storage of electrodes in the thermal boxes and also providing the cleanliness of edges of joints to be welded, not always can provide the low levels of hydrogen content.

As is known, according to the Sieverts law the content of hydrogen dissolved in iron is determined by the partial pressure of hydrogen in the gas phase. The source of hydrogen in the weld metal is the electrode coating and the water vapor of ambient atmosphere. As the gas- and slag-forming components the electrode coating includes carbonates $CaCO_3$ and $MgCO_3$ providing protection of the arc zone from ambient atmosphere, fluorspar, quartz sand, rutile, aluminosilicates, etc., as well as alloying components, deoxidizers and processing additives. The mineral components contain different amounts of water impurities in different form [1, 2], alloying components — hydrogen [2] in their composition. Together with the moisture of dry residue of liquid glass the total content of hydrogen in the coating is defined as the potential hydrogen $(H)_p$.

During heating of the coating, in the zone of arcing the process of slag formation together with the dissociation of carbonates, a number of reactions in the gas phase and the absorption of hydrogen by the weld pool metal occur [3]. As was established by the experiments and thermodynamic calculations [4, 5], in welding under silicon-manganese fluxes the reaction CaF_2 and SiO_2 with formation of SiF_4 followed by the

Table 1. Data on thermal dissociation of gas molecules and energy of bonds break

Dissociation of molecules	Degree of dissociation α at $T = 3500$ K	Binding energy D_0, kJ/mol
$H_2 = H + H$	0.282	438
$H_2O = OH + H$	0.331	484
$O_2 = O + O$	0.236	494
$HF = H + F$	$7.2 \cdot 10^{-2}$	565
$N_2 = N + N$	$1.1 \cdot 10^{-4}$	941
$CO = C + O$	$\sim 1.0 \cdot 10^{-10}$	1071

reaction of SiF_4 with H_2O and H_2 with formation of fluoride hydrogen gained the noticeable development.

Initially, it was suggested that HF is a very stable compound in the arc gas phase up to ~6000 °C, which allows binding hydrogen and thus reducing the tendency of welds to pores formation caused by hydrogen. Using the new thermodynamic data on the properties of substances, Prof. Frumin [5] noted that HF is thermally more resistant to dissociation than H_2, H_2O and OH, and, thus, may lead to reduction of hydrogen content in the weld pool. Applying the mass-spectral method [6], Prof. Pokhodnya and the colleagues established the presence of SiF_4 and HF in the samples of gases evolved during welding using flux-cored wires, and the formation of HF in the arc discharge in vacuum using the electrode containing CaF [7]. In work [8] the analysis of influence of temperature of the arc on the strength of diatomic HF, O_2, H_2 molecules to the dissociation was carried out and it was shown that at $T_a > 3000$ K HF dissociates and is resistant at the arc periphery, where binding of hydrogen can occur.

The data on the thermal dissociation of gas molecules, calculated on the basis of spectroscopic measurements from work [9] and on the energy of bonds break D_0 from work [10], are presented in Table 1. It follows from them that the degree of thermal dissociation of HF depending on the temperature is somewhat lower as compared to the molecules of O_2 and H_2, but significantly higher than that of N_2 and CO.

The molecule N_2 is more resistant to dissociation as compared to HF. However, both nitrogen and hydrogen are dissolved in iron to a greater extent starting from ≈600 °C. According to the data of studies [11, 12], during the collision of molecules H_2 and N_2 against the surface at the appropriate orientation due to the force field of unsaturated bonds of the surface atoms of iron, the dissociation of molecules and transition of H and N to the dissolution in the lattice are considerably facilitated. Thus, at the periphery of arc column the process of dissolution of hydrogen, located in compound with fluorine, is also possible, if to compare the energies of bonds break D_0 and the dependences of dissociation HF and N_2 on the temperature.

According to the data given in Table 1, the most robust molecule is the carbon oxide. The degree of its dissociation at $T = 6000$ K amounts to $\alpha \approx 9.59 \cdot 10^{-2}$, i.e. at the arc column temperature CO is almost not dissociated [13]. The experiments in CO arc welding [14] showed that the coefficient of elements transition to the weld metal is equal to 0.9–1.0, i.e. the high energy of C–O bond practically ensures its neutrality to the weld pool metal similar to Ar or He.

The thermodynamic analysis of SiF_4 formation and its further reaction with water vapors and hydrogen show the possibility of reducing the hydrogen content in the weld metal. The efficiency of $[H]_{diff\,d.m}$ reduction was investigated by introducing of CaF_2 and muscovite mica containing ~4.5 % of H_2O to the composition of coating of experimental electrodes at the content of 46–50 % of marble, quartz sand and muscovite mica in sum of 28 %. The calcination of electrodes was carried out at $T = 420$ °C for 1 h. Welding of specimens was performed at 160 A direct current of reverse polarity. The content of $[H]_{diff\,d.m}$ was measured according to GOST 23338 using the chromatographic method. The results of the experiments are given in Figure 1.

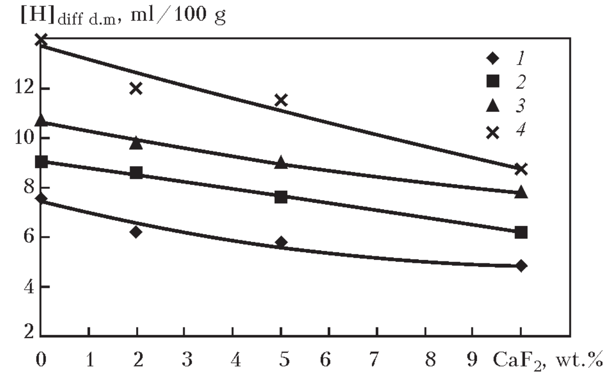

Figure 1. Dependence of $[H]_{diff\,d.m}$ content on content of CaF_2 in coating composition: *1* — 0; *2* — 2; *3* — 5; *4* — 10 % of CaF_2

According to the obtained data it is seen that with increase in CaF_2 content in the composition of coating at the different levels of introduced moisture the content of $[H]_{diff\,d.m}$ decreases. The degree of reduction of $[H]_{diff\,d.m}$ with the growth in CaF_2 content is decreased. Such a character of dependence of $[H]_{diff\,d.m}$ content on CaF_2 content was obtained in studies [15, 16] and is explained by decrease in activity of silica with the growth of CaF_2 content.

In the absence of muscovite mica and CaF_2 in the composition of coating the content of $[H]_{diff\,d.m}$ amounted to 8.5 ml/100 g. The partial pressure of hydrogen P_H (H_2, H, OH, H_2O) in the gas phase of arc gap was caused by the presence of $(H)_p$ in the

Table 2. $(H)_p$ content in electrode coating components, ml/100 g

Component	$(H)_p$ as-delivered	$(H)_p$ after calcination at 950–1000 °C
Quartz sand	175	~10
Fluorspar concentrate	340	~15
Rutile concentrate	490	~10

electrode coating, the products of $CaCO_3$ dissociation and also vapors of the slag melt components. At the introduction of 10 wt.% of CaF_2 to the composition of coating the decrease in the content of $[H]_{diff\ d.m}$ to 4.8 ml/100 g occurs. In this case P_H is additionally reduced due to SiF_4 formation through the reaction of CaF_2 and SiO_2, and HF formation, which reduces the ability of hydrogen to dissolve in the molten metal as compared to H_2 and H_2O coming from D_0 values. However, it should be noted that in the reaction of SiF_4 formation only a small fraction of the initial amount of CaF_2 and SiO_2 is involved [17].

To study the possibility of reducing $(H)_p$ of electrodes coating and $[H]_{diff\ d.m}$ the hydrogen thermal desorption from a number of components of electrode coatings was investigated using chromatographic method [18]. In Figures 2–5 the results of investigations of thermal desorption of hydrogen from quartz sand, fluorspar concentrate, rutile concentrate and dry residue of Na glass with modulus equal to 3, are shown. Heating rate of specimens was 5–7 °C/min. The content of $(H)_p$ in the components of electrode coating is presented in Table 2.

The content of $(H)_p$ in dry residue of liquid glass, obtained after its drying and calcination at 400 °C, amounted to 530 ml/100 g. The content of $(H)_p$ in marble of two fields is given in [19]. Obviously, the water content in the minerals can depend on the fields and technological processing.

The content of $(H)_p$ in the minerals forms a considerable fraction of $(H)_p$ of dry residue of liquid glass. The temperature of electrodes calcination is limited as a rule to 400–450 °C, therefore, from the data in Figures 2–5 it is seen that high-temperature component of $(H)_p$ will also serve as a source of hydrogen. The heat treatment of components at 900–1000 °C allows reducing $(H)_p$ content (see Table 2).

Table 3. Influence of heat treatment of electrode coating components on reduction of $[H]_{diff\ d.m}$ content

Electrode	State of components for manufacture of electrodes	$[H]_{diff\ d.m}$, ml/100 g
48KhN-5AN	As-delivered	(4.8, 4.8, 4.8); 4.8
	After heat treatment	(3.3, 3.7, 3.6, 2.9); 3.3
Pilot 1	As-delivered	(3.9, 3.9, 3.7); 3.8
	After heat treatment	(2.9, 2.9, 3.1); 3.0
Pilot 2	As-delivered	(2.7, 2.6, 2.6); 2.6
	After heat treatment	(2.0, 2.0, 2.3); 2.1

Note. In brackets the results of separate measurements are given, without brackets — average value.

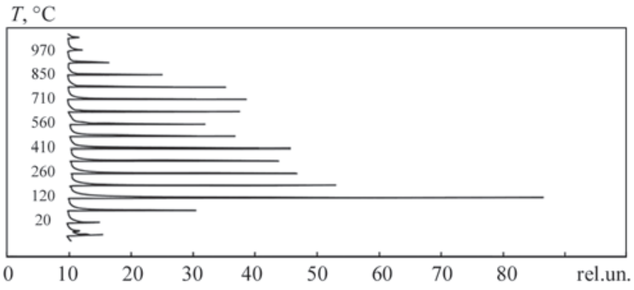

Figure 2. Thermal desorption of hydrogen from fluorspar concentrate

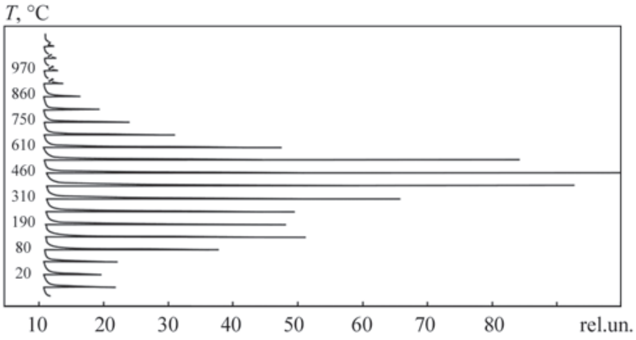

Figure 3. Thermal desorption of hydrogen from rutile concentrate

The efficiency of heat treatment of the components was tested during the development of electrodes designed for welding of high-strength low-alloyed steels. The test results are given in Table 3. Welding

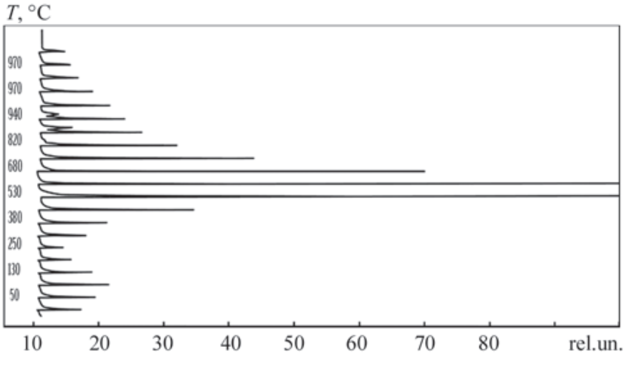

Figure 4. Thermal desorption of hydrogen from quartz sand

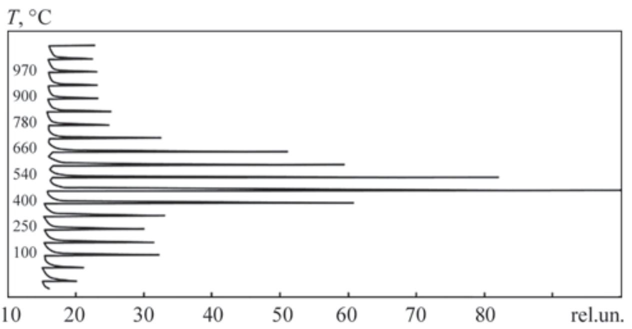

Figure 5. Thermal desorption of hydrogen from Na glass dry residue

was performed at 150–160 A direct current of reverse polarity. Temperature of electrodes calcination was 450 °C during 1 h. The presented results show the influence of heat treatment of components on the reduction of $(H)_p$ content and the ability to provide $[H]_{diff\ d.m} = 2–3$ ml/100 g depending on the composition of coatings.

Conclusions

1. The efficiency of reducing the $[H]_{diff\ d.m}$ content in the welds by introducing CaF_2 to the composition of electrode coating decreases with the increase in its content and decrease in $(H)_p$ content in the electrode coating.

2. The energy of bond D_0 of HF molecule can be insufficient to prevent dissolution of hydrogen in the compound with fluorine from the arc gap.

3. The water impurities in the components are not removed completely during calcination of electrodes and they impede the formation of ultra-low hydrogen contents in the weld metal.

4. The reduction of $[H]_{diff\ d.m}$ content in the welds to 3.2 ml/100 g is possible by decrease in $(H)_p$ components of electrode coatings using heat treatment.

1. Betekhtin, A.G. (1950) *Mineralogy*. Moscow: Gosgeologoizdat.
2. Lushkov, N.A., Razduj, F.I., Shpejzman, V.M. (1959) *Hydrogen in welds and its prevention*. Leningrad: Sudpromgiz.
3. Pokhodnya, I.K., Gorpenyuk, V.N., Milichenko, S.S. et al. (1990) *Metallurgy of arc welding. Processes in arc and melting of electrode*. Ed. by I.K. Pokhodnya. Kiev: Naukova Dumka.
4. Kirdo, I.V., Podgaetsky, V.V. (1949) On effect of fluxes on automatic weld porosity caused by rust. *Trudy po Avtomatich. Svarke pod Flyusom*, **6**, 36–62.
5. Frumin, I.I. (1956) Pores prevention in welding and submerged arc surfacing. *Avtomatich. Svarka*, **6**, 1–30.
6. Pokhodnya, I.K., Shvachko, V.I., Ustinov, V.G. et al. (1972) Mass-spectrometric analyses of gaseous fluorides evolving in arc welding. *Ibid.*, **6**, 10–12.
7. Pokhodnya, I.K., Shvachko, V.I. (1981) Formation of hydrogen fluoride in arc discharge. *Ibid.*, **2**, 11–13.
8. Pokhodnya, I.K., Shvachko, V.I., Utkin, S.V. (1998) Calculated evaluation of hydrogen behavior in arc discharge. *Ibid.*, **9**, 4–7, 11.
9. (1964) *Reference book of chemist*. Vol. 3. Moscow; Leningrad: Khimiya.
10. Gurvich, L.V. (1974) *Energy of breaking of chemical bonds. Ionization potentials and electron affinity*. Moscow: Nauka.
11. Gerasimov, Ya.I., Dreving, V.P., Eremin, E.N. et al. (1966) *Physical chemistry*. Moscow: Khimiya.
12. Lakomsky, V.I. (1998) Phenomenological theory of diatomic gases sorption of metal from electric arc plasma. In: *Actual materials science of 21st century*. Kyiv: Naukova Dumka.
13. Pentegov, I.V. (2004) Generalization of formula of K.K. Khrenov for determination of temperature of welding arc plasma. *The Paton Welding J.*, **8**, 48–50.
14. Zameryakin, L.K., Galaktionov, A.T. (1967) CO_2-shielded electric arc welding. *Avtomatich. Svarka*, **6**, 74–75.
15. Pokhodnya, I.K., Yurlov, B.V., Shvachko, V.I. et al. (1990) Effect of gaseous fluorides on hydrogen content in welds made by high-efficient electrodes with basic type coating. *Ibid.*, **11**, 1–6.
16. Demchenko, E.L., Snisar, V.V., Lipodaev, V.N. et al. (1991) Ways of hydrogen content decrease in weld metal of 03Kh12N8M2GST type in arc welding. *Ibid.*, **10**, 23–27.
17. Kuzmenko, V.G. (1980) Peculiarities of reaction of interaction between calcium and silica at 800–1900 °C. *Ibid.*, **6**, 33–35.
18. Paltsevich, A.P. (1999) Chromatographic method for determination of hydrogen content in components of electrode coatings. *Ibid.*, **6**, 46–48.
19. Pokhodnya, I.K., Yavdoshchin, I.R., Paltsevich, A.P. et al. (2004) *Metallurgy of arc welding. Interaction of metals with gases*. Ed. by I.K. Pokhodnya. Kiev: Naukova Dumka.

Received 29.12.2015

INFLUENCE OF FILLER METAL ON STRUCTURE AND PROPERTIES OF WELDED JOINTS OF HIGH-STRENGTH TWO-PHASE TITANIUM ALLOYS PRODUCED USING ARGON ARC WELDING

S.V. AKHONIN, V.Yu. BELOUS, I.K. PETRICHENKO and **R.V. SELIN**
E.O. Paton Electric Welding Institute, NASU
11 Kazimir Malevich Str., 03680, Kiev, Ukraine. E-mail: office@paton.kiev.ua

The welded joints of high-strength titanium alloys, produced using arc welding, have, as a rule, unsatisfactory values of mechanical properties, especially those of ductility in the as-welded state as compared to the base metal. In the work the effect of thermal welding cycle, type of filler metal and the post-weld heat treatment on the structure and properties of welded joints of two-phase high-alloyed titanium alloys having $\sigma_t > 1000$ MPa, were evaluated. The properties and structure of welded joints of high-strength titanium alloys VT23, T110 and experimental alloy Ti–6.5A1–3Mo–2.5V–4Nb–1Cr–1Fe–2.5Zr, made by argon arc welding applying the filler wires, differing by their composition from the base metal, were studied. It is rational to produce the joints of complex-alloyed titanium alloy Ti–6.5A1–3Mo–2.5V–4Nb–1Cr–1Fe–2.5Zr using argon arc welding applying filler wire VT1-00sv at modes, providing the through penetration and the content of wire components in the weld metal at level of 10 % in combination with the subsequent high-temperature annealing. 6 Ref., 1 Table, 6 Figures.

Keywords: *titanium alloys, argon arc welding, filler wire, properties, structure*

The welded joints of high-strength titanium alloys, produced using arc welding, have, as a rule, unsatisfactory values of mechanical properties, especially those of ductility in the as-welded state as compared to the base metal. Therefore, it is often recommended to produce such joints applying filler metal for improvement of mechanical properties of the weld metal. However, due to the limited choice of filler materials for welding of high-strength two-phase titanium alloys, there is urgent problem of selecting the type of filler material, when developing the technology for welding of new high-strength titanium alloys.

In welding of titanium alloys with high tensile strength it is rational to change either the degree, or the system of weld metal alloying [1, 2]. It is the easiest to make this during fusion arc welding applying the filler wires, differing by chemical composition from the base metal. The thermal cycle of arc welding of high-alloyed titanium alloys leads to the substantial change in the structure of both the near-weld zone as well as weld metal, and, as a consequence, in deterioration of mechanical characteristics of the welded joint. Therefore, when developing the technology for welding of high-strength titanium alloys, and selecting or developing the filler material, it is necessary to pay attention to the possibility of producing welded joints with high impact toughness, moreover, the strength of the joints should be at least 0.9 of the strength of base material. Furthermore, to improve the properties of welded joints in the area of HAZ and to relieve welding stresses it is rational to use the postweld heat treatment (PWHT).

The aim of the work is the evaluation of effect of thermal welding cycle, type of filler metal and PWHT on the structure and properties of welded joints of two-phase high-alloyed titanium alloys having $\sigma_t >$ > 1000 MPa. The properties of high-strength titanium alloys VT23, T110 and experimental alloy Ti–6.5A1–3Mo–2.5V–4Nb–1Cr–1Fe–2.5Zr welded joints [3], produced using argon arc welding applying tungsten electrode (TIG) with application of filler metal to the groove and without the edge preparation, were compared.

The joints of alloys VT23 [4] and T110 were produced using TIG welding of plates of 8 mm thickness, welding was carried out to the edge groove applying filler wire SP15sv (Ti–4.5A1–2.5Mo–2.5V–3.5Nb–1.5Zr) designed for welding of high-strength titanium alloys VT23 and VT22 (Figure 1, *a*).

The high-strength alloy of grade T110 of system Ti–5.5A1–1.2Mo–1.2V–4Nb–2Fe–0.5Zr was developed at the PWI together with the O.K. Antonov ASTC [5].

The welded joints of experimental high-alloyed 8-component system Ti–6.5A1–3Mo–2.5V–4Nb–

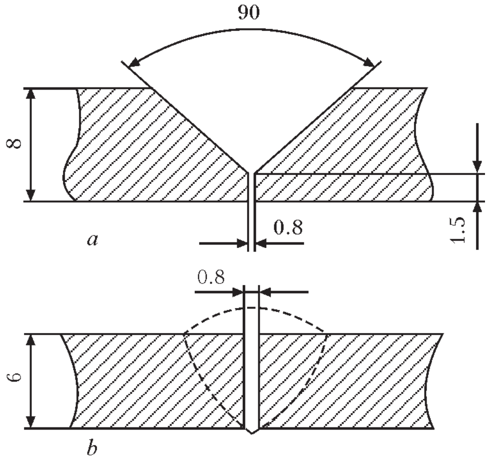

Figure 1. Scheme of edge preparation for TIG welding: *a* — one-sided welding with edge preparation and feeding of filler wire SP15sv; *b* — one-sided welding without edge preparation with feeding of filler wire VT1-00sv

1Cr–1Fe–2.5Zr were produced with thickness of 6 and 8 mm. Moreover, the joints of 8 mm thickness were produced using multilayer TIG welding to the edge groove applying filler wire SP15sv (see Figure 1, *a*) and the joints of 6 mm thickness were made with through penetration applying filler wire VT1-00sv (Figure 1, *b*). Alloy Ti–6.5A1–3Mo–2.5V–4Nb–1Cr–1Fe–2.5Zr contains more alloying elements as compared to T110 alloy and in the as-annealed state it has tensile strength exceeding 1200 MPa.

One-side TIG welding was performed using electrode of 5 mm diameter. Welding current amounted to 250–350 A, welding speed was 10 m/h. After welding, all the welded joints were subjected to annealing. The temperature of annealing for experimental alloy Ti–6.5A1–3Mo–2.5V–4Nb–1Cr–1Fe–2.5Zr was selected in order to provide the highest impact toughness of weld metal and, according to the results of work [3], it amounted to 900 °C (1 h) in combination with the subsequent furnace cooling. The examples of produced welded joints are given in Figure 2.

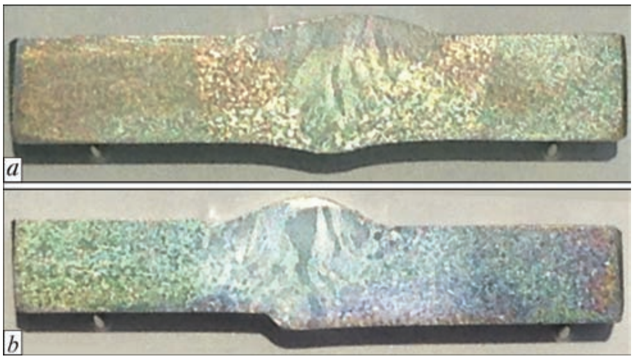

Figure 2. Type of TIG-welded joints of alloy Ti–6.5A1–3Mo–2.5V–4Nb–1Cr–1Fe–2.5Zr: *a* — to edge groove; *b* — without edge preparation with feeding of filler wire VT1-00sv

The investigations showed that the TIG-welded joint of alloy Ti–6.5A1–3Mo–2.5V–4Nb–1Cr–1Fe–2.5Zr with through penetration applying filler wire VT1-00sv, which was fed in the welding process at rate of 60 m/h, has content of filler metal in weld at level of 20 %, and the joint, produced using VT1-00sv wire, fed at rate of 30 m/h, has content of filler in weld metal at level of 10 %. The joint, welded to V-shaped groove applying wire SP15sv, was performed in 3 passes and the weld consists mainly of filler metal.

The properties of produced welded joints in the state after welding and annealing are given in the Table. The application of filler wire in TIG welding of alloys VT23 and T110 to the edge groove provides the strength of welded joints at level of 90 % of strength of the alloy itself. This condition is not fulfilled in case of TIG welding to the edge groove of the joints of alloy Ti–6.5A1–3Mo–2.5V–4Nb–1Cr–1Fe–2.5Zr applying wire SP15sv.

The width of welds in the upper part amounts to about 14 mm and in the root part it is about 3 mm. The macrostructure of metal of welds, produced both to the groove as well as without the groove, is composed of non-equiaxial grains elongated in the direction of heat dissipation. The coarsest grains are located in the weld upper part. The angle between the grain axis and the weld axis amounts from 0 to 30°. The

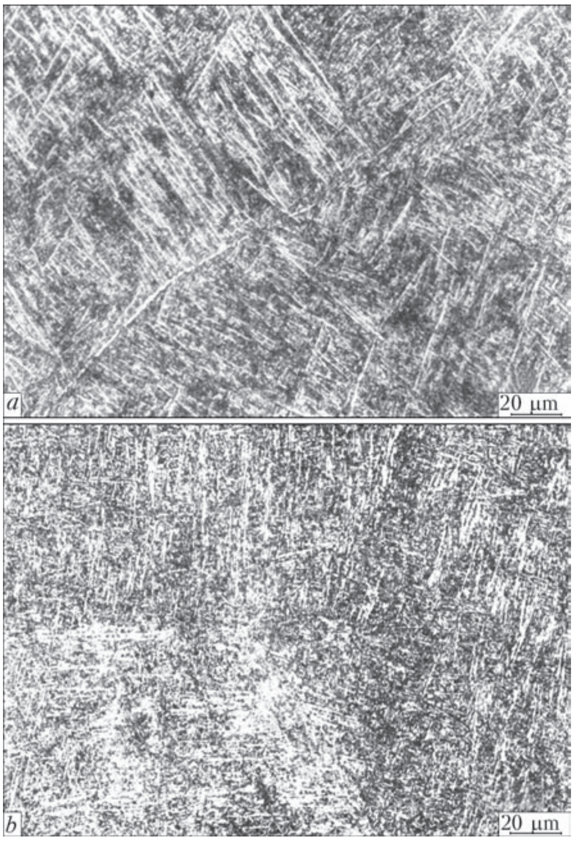

Figure 3. Microstructure of weld metal produced using TIG welding with filler wire SP15sv in the state after annealing at 750 °C for 1 h: *a* — alloy VT23; *b* — T110

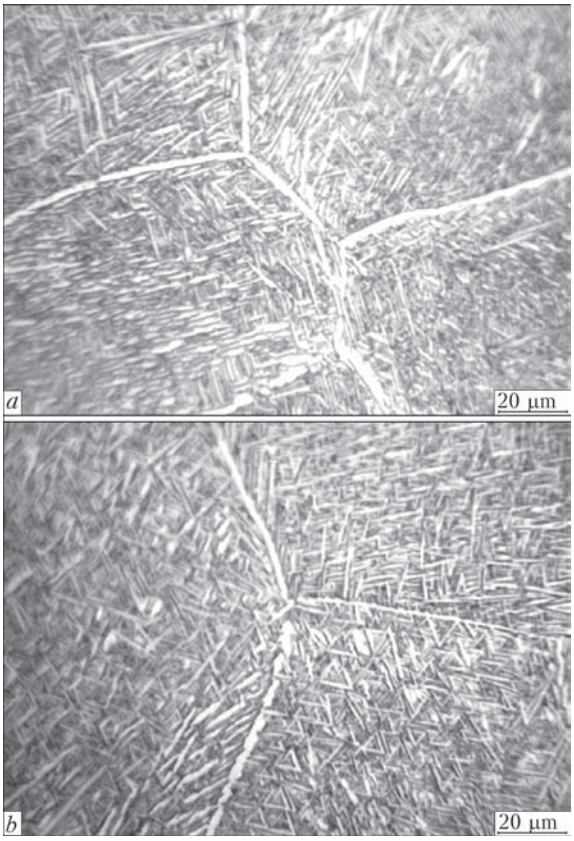

Figure 4. Microstructure of base metal (*a*) and HAZ (*b*) of TIG-welded joints of alloy Ti–6.5A1–3Mo–2.5V–4Nb–1Cr–1Fe–2.5Zr, produced applying filler wire VT1-00sv, in the state after annealing at 900 °C for 1 h

base and HAZ metals consist of the equiaxial grains corresponding to No. 3–4 at the comparison with the reference scales.

The investigations of the structure of produced welded joints showed that in TIG welding of alloy VT23 applying wire SP15sv a negligible decrease in alloying level of weld metal occurs. In the as-welded state the structure is formed in the weld, consisting mainly of metastable α´-(α´´) phase. As a result of annealing the stable laminar α-phase and the dispersed mixture of α- and β-phases are formed (Figure 3, *a*). Also in the weld of alloy T110 as a result of annealing at 750 °C the decomposition of metastable phases with formation of laminar α-phase and fine-dispersed mixture of α- and β-phases occur (Figure 3, *b*).

8-component alloy Ti–6.5A1–3Mo–2.5V–4Nb–1Cr–1Fe–2.5Zr in the initial state had fine-dispersed structure in the ranges of primary β-grains [3]. The morphology of α-phase in the base metal after annealing at 900 °C during 1 h and furnace cooling is laminar, and the plate width amounts to 1–1.5 mm (Figure 4, *a*). Along the boundaries of the primary β-grains the α-fringe is present. In HAZ after the same annealing the metal structure has also laminar character (Figure 4, *b*), but the plates are finer than in the metal of weld produced applying wire VT1-00sv (20 %), that is connected with higher alloying of HAZ metal than that of weld metal. The delayed furnace cooling from 900 °C was performed to prevent fixing of the metastable phases.

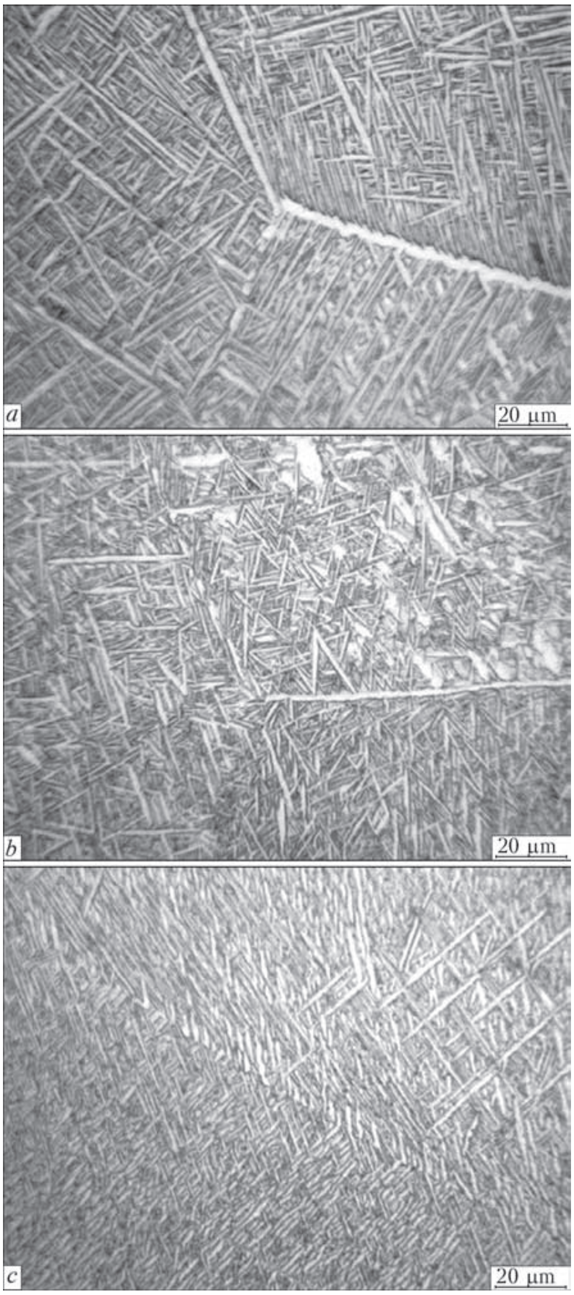

Figure 5. Microstructure of weld metal of TIG-welded joint of alloy Ti–6.5A1–3Mo–2.5V–4Nb–1Cr–1Fe–2.5Zr after annealing at 900 °C for 1 h: *a* — wire VT1-00sv content of 20 % in weld metal; *b* — of 10 %; *c* — welding to groove with wire SP15sv

The weld metal of alloy Ti–6.5A1–3Mo–2.5V–4Nb–1Cr–1Fe–2.5Zr produced applying wire VT1-00sv at the presence of 20 % of filler in the weld is characterized by a larger laminar structure (Figure 5, *a*). In the weld metal the plates have a greater length and thickness of 1.5–2 μm, and in the gaps between the plates the (α + β) structure is dispersed. As compared to annealing at 750 °C, when the metal structure of all the zones of welded joints remained

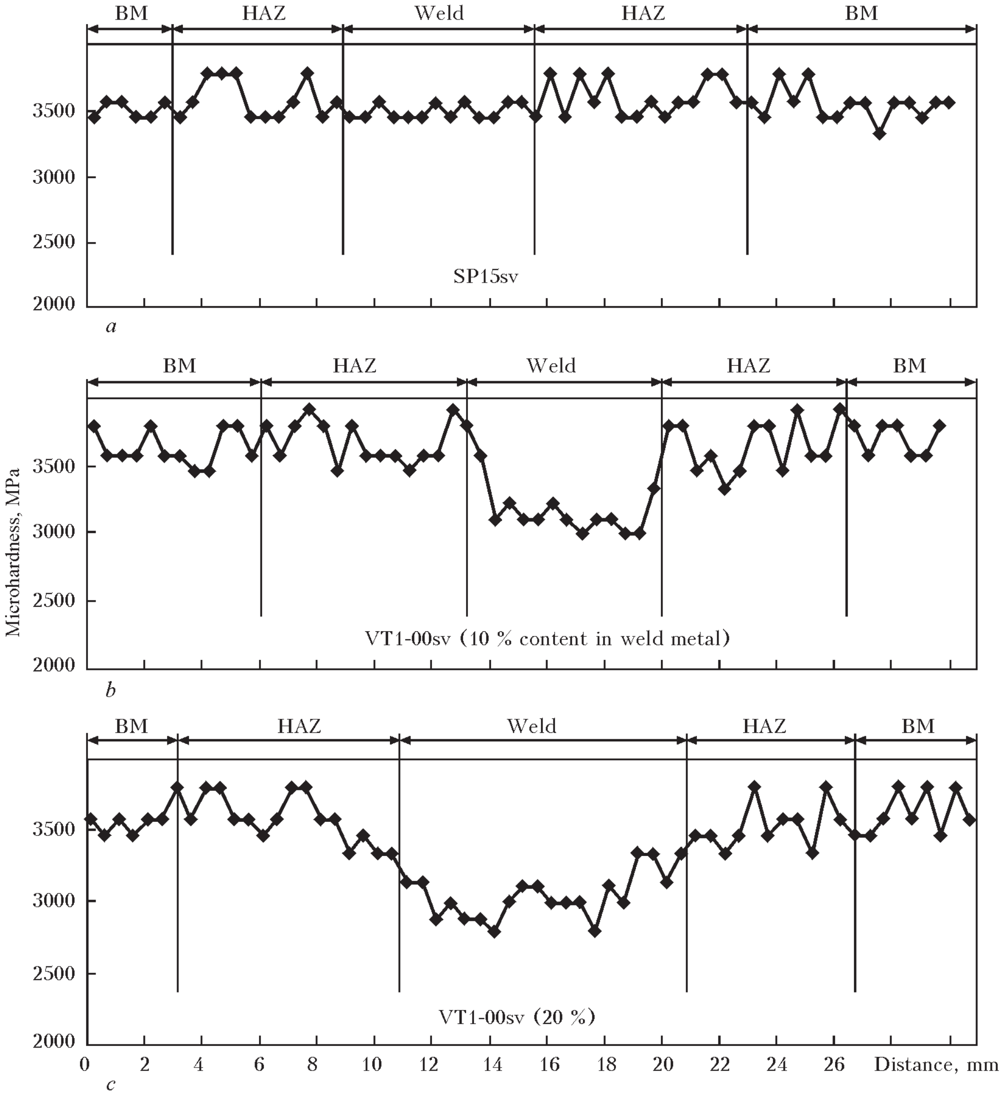

Figure 6. Microhardness of TIG-welded joint of experimental alloy Ti–6.5A1–3Mo–2.5V–4Nb–1Cr–1Fe–2.5Zr, produced applying different filler wires in the state after annealing at 900 °C for 1 h

fine-dispersed [3], the coagulation of α-phase after annealing at 900 °C can provide some increase in the ductile properties.

When introducing 10 % of wire VT1-00sv to the weld, the dilution degree of weld metal will be lower than in the previous case, therefore the microstructure of weld metal is finer, the plates of α-phase are shorter and have thickness of 1.0–1.5 μm (Figure 5, *b*).

In TIG welding to the edge groove a significant amount of filler gets to the weld metal, in case with wire SP15sv, alloying system of which differs from the alloying system of base metal, the weld metal has a structure differing from the structures produced in the case with applying of wire VT1-00sv. The microstructure of weld metal of alloy Ti–6.5A1–3Mo–2.5V–4Nb–1Cr–1Fe–2.5Zr, produced to the edge groove using wire SP15sv, after annealing at 900 °C, is presented in Figure 5, *c*. The microstructure of metal of the considered weld as compared to the microstructure of welds produced with wire VT1-00sv is characterized by a higher dispersity of the α-phase particles. The plates of α-phase have a smaller length and their thickness amounts to 0.5–1.5 μm.

The distribution of microhardness in weld metal of alloy Ti–6.5A1–3Mo–2.5V–4Nb–1Cr–1Fe–2.5Zr in the as-annealed state (Figure 6) showed a great heterogeneity in the joints with 20 % of VT1-00sv filler.

Thus, it is rational to produce the joints using TIG welding for complex-alloyed titanium alloy Ti–6.5A1–3Mo–2.5V–4Nb–1Cr–1Fe–2.5Zr with filler wire VT1-00sv on the modes, providing the through penetration and content of wire in the weld metal at level of 10 %. As a result of subsequent annealing at 900 °C a finer-dispersed structure is formed than that at 20 % content of the filler , that provides good values of strength and impact toughness of welded joints.

Conclusions

1. Use of high-alloy filler wire SP15sv in TIG welding to the edge groove of alloys VT23 and T110 with the

Mechanical properties of TIG-welded joints of titanium alloys produced applying different filler wires

Titanium alloy	Filler wire (content in weld metal)	Plate thickness, mm	State of welded joints	σ_t, MPa	Impact toughness of weld metal *KCV*, J/cm^2
VT23	SP15sv	8	As-welded	1010	21
VT23	SP15sv	8	Annealing at 750 °C, 1 h, air cooling	1090	22
T110	SP15sv	8	As-welded	1030	20
T110	SP15sv	8	Annealing at 750 °C, 1 h, air cooling	1020	35
Ti–6.5Al–3Mo–2.5V–4Nb–1Cr–1Fe–2.5Zr	VT1-00sv (20 %)	6	As-welded	1226	15
Ti–6.5Al–3Mo–2.5V–4Nb–1Cr–1Fe–2.5Zr	VT1-00sv (20 %)	6	Annealing at 900 °C, 1 h, furnace cooling	1048	27
Ti–6.5Al–3Mo–2.5V–4Nb–1Cr–1Fe–2.5Zr	VT1-00sv (10 %)	6	As-welded	1287	11
Ti–6.5Al–3Mo–2.5V–4Nb–1Cr–1Fe–2.5Zr	VT1-00sv (10 %)	6	Annealing at 900 °C, 1 h, furnace cooling	1110	24
Ti–6.5Al–3Mo–2.5V–4Nb–1Cr–1Fe–2.5Zr	SP15sv	8	As-welded	1208	18
Ti–6.5Al–3Mo–2.5V–4Nb–1Cr–1Fe–2.5Zr	SP15sv	8	Annealing at 900 °C, 1 h, furnace cooling	1047	25

subsequent annealing at 750 °C provides the required level of mechanical properties of welded joints.

2. Use of high-alloy filler wire SP15sv for producing the joints using TIG welding to the edge groove of high strength 8-component alloy Ti–6.5A1–3Mo–2.5V–4Nb–1Cr–1Fe–2.5Zr does not provide the required level of strength of welded joints.

3. Application of postweld annealing at 900 °C of high-strength alloy of system Ti–6.5A1–3Mo–2.5V–4Nb–1Cr–1Fe–2.5Zr provides a complete decomposition of metastable phases, as a result of annealing the equilibrium finer-dispersed structure is formed, providing satisfactory values of impact toughness of the joints.

4. High values of strength (σ_t = 1110 MPa) at good impact toughness (*KCV* = 24 J/cm^2) of welded joints of alloy Ti–6.5A1–3Mo–2.5V–4Nb–1Cr–1Fe–2.5Zr were obtained applying filler wire VT1-00sv at welding modes providing the through penetration and 10 % content of filler in the weld metal.

1. Gurevich, S.M., Kushnirenko, N.A., Topolsky, V.F. (1980) Search of filler material for welding of titanium alloys. In: *Actual problems of welding of nonferrous metals*, 234–236. Kiev: Naukova Dumka.
2. Zamkov, V.N., Topolsky, V.F., Tyapko, I.K. (1993) Peculiarities of metallurgy and arc welding technology of heat hardenable titanium alloys. In: *Welding Technology of Paton Institute at TWI Proc*. (Abington, Cambridge, 13–14 Oct., 1993).
3. Akhonin, S.V., Belous, V.Yu., Selin, R.V. et al. (2015) Structure and properties of EB- and TIG-welded joints of high-strength two-phase titanium alloys. *The Paton Welding J.*, **8**, 14–17.
4. Khorev, A.I. (2008) High-strength titanium alloy VT23 and its application in advanced welded structures. *Svarochn. Proizvodstvo*, **9**, 3–8.
5. Zamkov, V.M., Topolsky, V.P., Trygub, M.P. et al. *High-strength titanium alloy*. Pat. 40087 Ukraine. Publ. 16.06.2003.

Received 13.10.2015

ELECTRON BEAM WELDABILITY OF DAMAGE-TOLERANT TITANIUM ALLOY TC21

YUAN HONG, ZHANG GUO-DONG, WANG JIN-XUE, YU HUAI and **ZHU ZHI-SHOU**
Beijing Institute of Aeronautical Materials
100095, Beijing, China. E-mail: hong.yuan@biam.ac.cn

In China TC21 alloy represents itself α + β titanium alloys with tensile strength of 1100 MPa, high fracture toughness and low fatigue crack growth rate. The study of EBW of thick-section TC21 alloy was carried out and mechanical properties of welded joints were evaluated. Testing of fracture toughness and resistance to fatigue crack reveal that their damage tolerance is comparable to that of base metal. The high cycle fatigue strength of the EB-welded joints is 643 MPa, reaching 98.3 % of that of base metal. The microstructure of weld metal consists of coarse columnar dendritic prior β-grains and finer acicular α-martensite, which accounts for the difference of crack growth rate and fracture toughness between base metal and metal of welded joints. These results indicate that TC21 titanium alloy has excellent EB weldability. 8 Ref., 1 Table, 9 Figures.

Keywords: *electron beam welding, damage tolerance, fracture toughness, fatigue crack propagation*

Titanium alloys are widely used in the airframe and critical systems because of their specific strength, resistance to fatigue, high temperature and environmental effects [1]. The design methods change markedly influenced titanium alloy development direction and promoted development of high damage-tolerant titanium, which possesses high fracture toughness and low crack propagation rate [2, 3].

In China TC21 alloy represents itself α + β titanium alloys with tensile strength of 1100 MPa, which has the excellent damage tolerance, high fracture toughness exceeding 90 $MPa\cdot m^2$ and low fatigue crack propagation rate da/dN up to $9\cdot 10^{-6}$ mm/cycle at $\Delta K = 11$ $MPa\cdot\sqrt{m}$ ($R = 0.1$). The alloy underwent manufacturing processing for composition optimizing, melt purifying, as weld as quasi-β forging and heat treatment to achieve specific strength and fracture toughness of not less than thouse of alloy Ti-1023. This indicates that alloy can be selected as the first-class material to manufacture the important support structures of airframes for advanced aircraft, where EBW technology will be of great necessity to assemble the airframe components of damage-tolerant titanium alloy.

In present work, the thermal simulation experiments, simulated EBW thermal cycles with various welding speed, were carried out for evaluation of dependencies of properties of welded joints on different welding line energy and various cooling rates. So we could acquaint with the EB weldability of TC21 alloy whether or not sensible to welding heat input. Results of the research will be directed to optimization of EBW parameters and postweld heat processing. The comparison of mechanical properties of EB-welded joints gained by varying welding speed symbolizing welding heat input character corresponds to the thermal simulation experiments. EBW conditions for 60 mm thickness TC21 alloy were studied, and the damage tolerance properties of the joints, such as fracture toughness and resistance to fatigue crack propagation, were evaluated.

Materials and experimental procedure. The base material used for simulation and welding experiments in this work is TC21 titanium alloy forged by quasi-β forging process with subsequent solution heat treatment (900 °C, 2 h, air cooling). Chemical compositions of the material was as follows, wt.%: 5.8Al–2.0Sn–2.0Zr–2.8Mo–2.0Nb–1.7Cr–0.1Si, and Ti — balance.

EBW simulation experiments conducted in Gleeble 1500 thermal simulator system were carried out by imposing thermal cycles on a series of square-section specimens. The specimens were cut from the forgings and machined up to 10×10×55 mm size. The simulation tests were performed at rapid heating rate of 1000 °C/s to preset peak temperature of 1200 °C for constant holding time of 40 s, followed by different cooling rate of 0.1, 0.5, 5, 25, 80 °C/s (air cooling), and 160 °C/s (water cooling) individually. The dimension of isothermal zone (or working zone) is about 8–10 mm across the middle of the specimen. The specimens simulated were machined to the samples for tensile strength and impact toughness tests at room temperature according to standard ISO

9016:2001. Charpy impact fracture toughness tests were performed in full-scale U-notch specimens.

Full penetration EBW was performed on KL106 machine, imported from E.O. Paton Electric Welding Institute, with medium accelerating voltage of 60 kV. The EBW parameters used given in the Table. The welding speeds for TC21 alloy 14 mm thick were selected from 4 to 25 mm/s that matched with suitable beam current in order to obtain the diversity of heat input. After welding, non-destructive testing was carried out to detect possible defects in the welded joints. The defect-free plates were selected to prepare specimens for evaluation their metallographic and mechanical properties.

The specimens for metallographic and tensile tests, which were cut from the EB-welded joints 14 mm thick, were prepared to evaluate the effect of welding heat input on their microstructure and mechanical properties. The 60 mm thick base metal and EB-welded joints were heat treated by duplex annealing (900 °C, 2 h, air cooling + 590 °C, 4 h, air cooling). Subsequently, the specimens for tests on tensile, Charpy U-notch impact, fracture toughness, high cycle fatigue and fatigue crack growth rate were machined according to ISO standards to compare the degradation of damage-tolerant properties of the EB-welded joints and base metal. The notch root of all the EB-welded joint specimens was located at the weld metal centre.

Specimens for metallurgical tests were grinded, polished, etched and examined by Olympus GX51 optical microscope. A more detailed microstructural characteristic study was carried out by using FEI Quanta600 scanning electron microscope.

Tensile and Charpy U-notch impact tests were carried out on Instron-5887 electron universal test machine and ANS ZBC2302 impact test machine, respectively. Plane strain fracture toughness testing was carried on MTS-370 electro-hydraulic servo machine employing compact tension (CT) specimens of 25 mm thickness and 60 mm width. Stress-amplitude controlled high-cycle fatigue tests were performed using a sinusoidal waveform at stress ratio $R = 0.06$. Plain cylindrical specimens were tested on QBG-50 electro-magnetic resonance testing machine at frequency of 115 Hz. Tests were terminated either by failure or not failing when 10^7 cycles were achieved. Fatigue crack growth (FCG) tests were conducted at constant $R = 0.06$ and frequency of 10 Hz on CT specimens with dimensions of 62.5 (length) × 50 (width) × × 12.5 (thickness) mm.

EBW parameters at $U_{acc} = 60$ kV and $l_{work} = 150$ mm

Plate thickness, mm	Beam current, mA	Welding speed, mm/s	Focus current, mA	Heat input, J/mm
14	165	25	830	396
	110	12	830	550
	70	4	830	1050
60	290	6	855	2900

Results and discussion. *Thermal simulation.* The stable simulating procedure was stable and was repeated while more than 3 samples were performed at the same thermal simulation parameters. Figure 1 shows the tensile and impact properties of the Gleeble-simulated specimens at different cooling rate. The strength values increase monotonously with the increasing of cooling rate, while the ductility and impact toughness change in the opposite way. Specimens at v_{cool} = = 0.1 and 0.5 °C/s have excellent ductility and impact toughness, whereas their tensile strength is relatively low. The mechanical properties change dramatically, when cooling rate increase from 0.5 to 5 °C/s, especially it is characteristic for impact toughness, which decreased from 42 to 9 J/cm^2. In particular, with increasing cooling rate from 5 to 160 °C/s, the degradation of ductility and impact toughness is not obvious.

It is clear that the approving cooling rate is controlled by less than 0.5 °C/s to achieve high comprehensive mechanical properties at EB processing, whereas the cooling rates of less than 0.5 °C/s is impossible to put into practice in fusion welding. Therefore, the conclusion was drawn that TC21 alloy is not sensitive to welding heat input and postweld weld cooling rates, especially in EBW — high energy density welding method. The microstructure and mechanical properties of the joints can't be improved evidently by the methods of meliorating the welding parameters and welding line energy, such as to solve the problem of getting back the missing ductility and toughness, and so on.

Effect of heat input on macrostructure and mechanical properties of EB-welded joints. The micro-

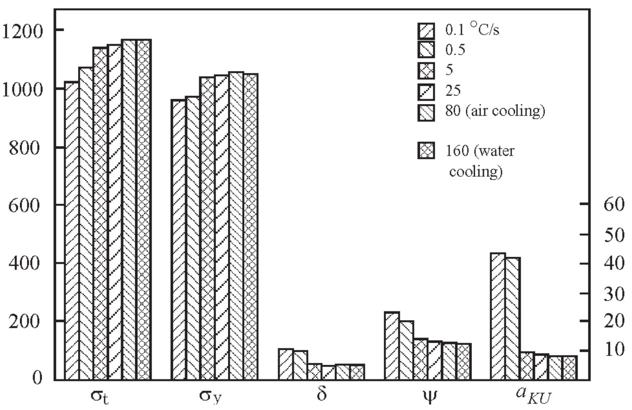

Figure 1. Tensile and impact properties of the Gleeble-simulated specimens at different cooling rate

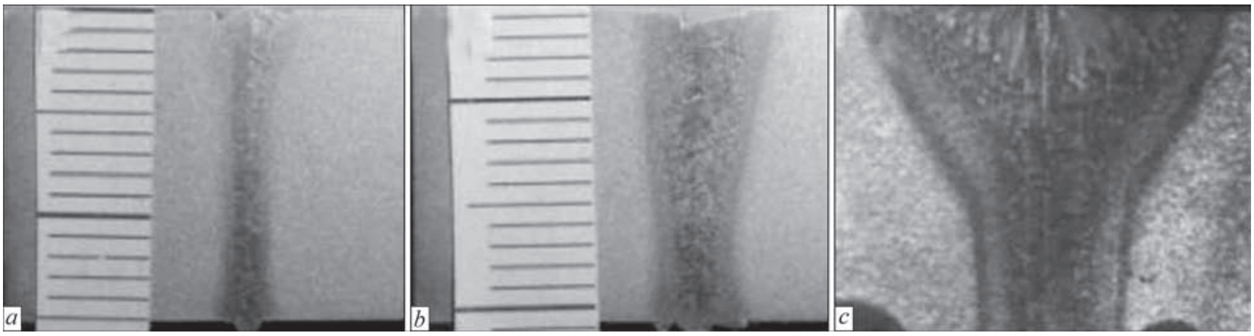

Figure 2. Cross-sectional macrographs of EB-welded joints at heat input of 396η (*a*), 550η (*b*) and 1050η (*c*) J/mm

structures and mechanical properties of joints are primarily determined by the results of phase transformation, such as arrangement, volume fraction and individual properties of two phases, allowing for welding thermal cycles. In EBW experiments the beam currents matched at 3 groups of welding speeds under condition of the invariable focus position, vacuum degree and accelerating voltage: I_b = 65, 110 and 165 mA at v_w = 4, 12 and 25 mm/s; welding line energy was 1050η, 550η and 396η J/mm, respectively (where η is the efficiency factor, identified the same condition). The cross-sectional macrographs of the EB-welded joints at different heat input are shown in Figure 2. The width of weld metal increases with increasing of heat input from 396 to 1050 J/mm. It can be seen that all the fusion zones consist of coarse columnar dendritic grains, which are perpendicular to the fusion zone boundary. The reason is that during molten metal solidification, grains tend to grow in the direction of maximum heat extraction.

The effect of heat input on mechanical properties is presented in Figure 3. The test results expressed that the regular mechanical properties are of little difference, in despite of welding parameters differentiated in heat input and cooling rates. The correlation between mechanical properties of the TC21 alloy EB-welded joints and heat input is negligible. As so high power density, EBW excels in the ability to strict the heated region in no time. The rate of temperature and cooling raise has distinct difference, despite of welding at varying parameters. Thus, the excellent mechanical properties of TC21 alloy EB-welded joints could be based on wide range of EBW parameters. This is in agreement with the Gleeble- simulated results.

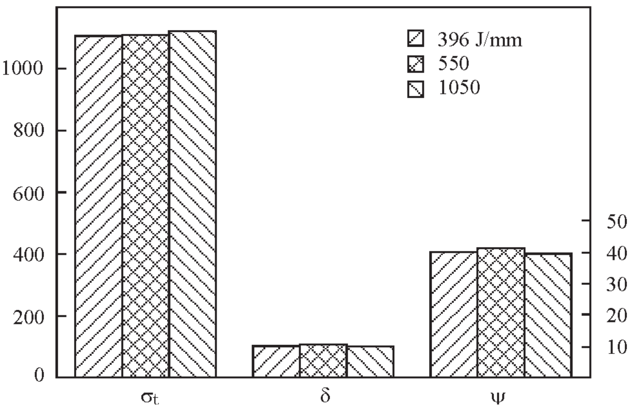

Figure 3. Mechanical properties of EB-welded joints at different heat input

EBW of 60 mm thick TC21 titanium alloy. For 60 mm thick TC21 alloy, the optimized EBW parameters were achieved using adequate trial welds with varying the parameters involved effecting weld character and defects. The beam focus position at 0.6*t* beneath the surface and 400 Hz circular oscillation proved to be the most suitable for v_w = 5 mm/s, accompanied by increased with more beam current and adjusting the slope-in/slope-out rates. At that, root spiking was suppressed [4], and satisfactory full penetration was achieved. Cross-sectional macrograph is shown in Figure 4. It can be seen that two sides of the weld boundary are parallel to each other, and the depth-to-width ratio is higher than 20:1.

The ultrasonic C-scan detection as a newly advanced method was used for NDT of welds, which has the advantage of high detection rate and high sensitivity for defects, such as lacks of penetration, lacks of fussion and pores. The ultrasonic C-scan direction and image are shown in Figure 5. It can be seen that the quality of welds was satisfying, except for such defects as end crater and bead reinforcement.

The tensile, impact and fracture toughness properties of the duplex annealed joints and base metal are illustrated in Figure 6. Results indicate that the

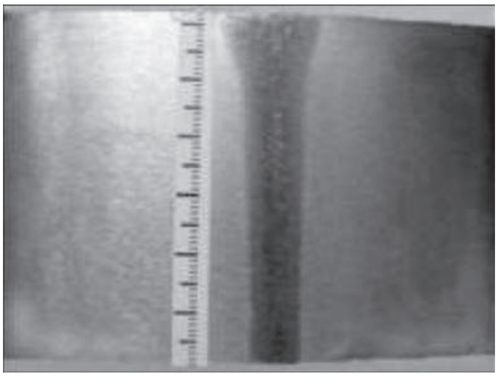

Figure 4. Cross-sectional macrograph of EB-welded joint 60 mm thick

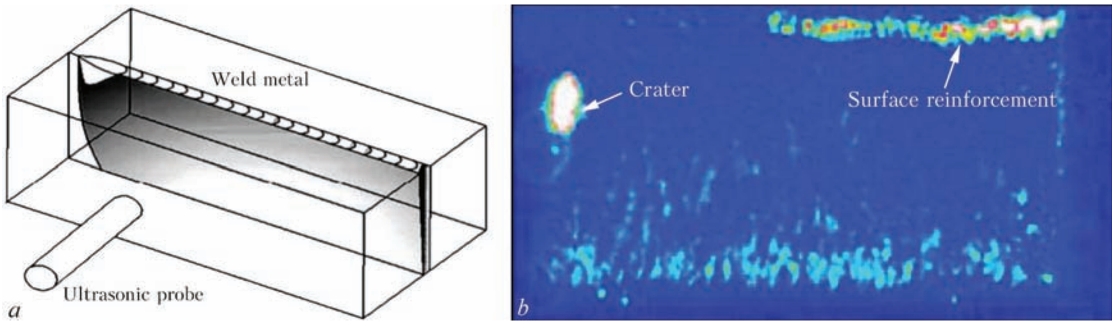

Figure 5. Ultrasonic C-scan of TC21alloy EB-welded joints 60 mm thick: *a* — schematic diagram; *b* — C-scan image

strength of welded joints is higher, while the ductility, impact and fracture toughness are slightly lower than those of base metal. It is noticeable that EB-welded joints show attractive fracture toughness. Their fracture toughness is 88.6 MPa·√m, reaching 92.5 % of that of base metal.

In this study, high cycle fatigue strength was determined by staircase method and then, stress-life (*S–N*) curves were obtained by grouping test method. *S–N* curves for rupture probability of 0.5 and scatter of experimental data are presented in Figure 7. Experimental results were described as the maximum stress amplitude level versus the number of cycles. Both base metal and joints show a similar trend of increasing fatigue life with decreasing stress amplitude. The fatigue life of the welded joints appeared to be slightly higher than that of base metal at high stress amplitude ($\sigma_{max} > 690$ MPa), whereas this situation alternated at low stress amplitude ($\sigma_{max} < 690$ MPa). It can be seen that the conditional fatigue strength ($N_f = 10^7$) of the welded joint is 643 MPa, which is ≈98.3 % of that of base metal (654 MPa), indicating that the fatigue endurance of the welded joints is excellent.

The *da*/*dN*–Δ*K* curves in Figure 8 show that both the base metal and the joint in possession of lamellar structure gain the inferior crack propagation behavior. The fatigue crack growth rate *da*/*dN* versus stress intensity factor range Δ*K* for EB-welded joints and base metal is shown in Figure 9. It is apparent that *da*/*dN*–Δ*K* curves have three regions: threshold, linear and unstable fracture ones. When Δ*K* < 21 MPa·√m, the fatigue crack growth rate of joint is lower than that of base metal at the same Δ*K* values. However, this tendency is reversed at high Δ*K* level.

Microstructures of TC21 duplex annealed alloy and weld metal are shown in Figure 9. The basketweave microstructure is characteristic for TC21

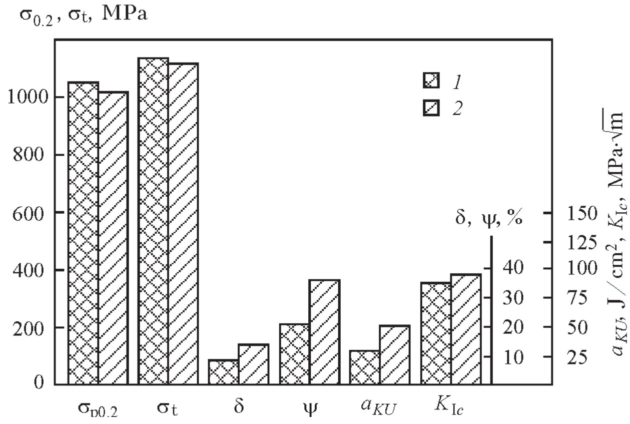

Figure 6. Tensile, impact and fracture toughness properties of Eb-welded annealed joints (*1*) and base metal (*2*)

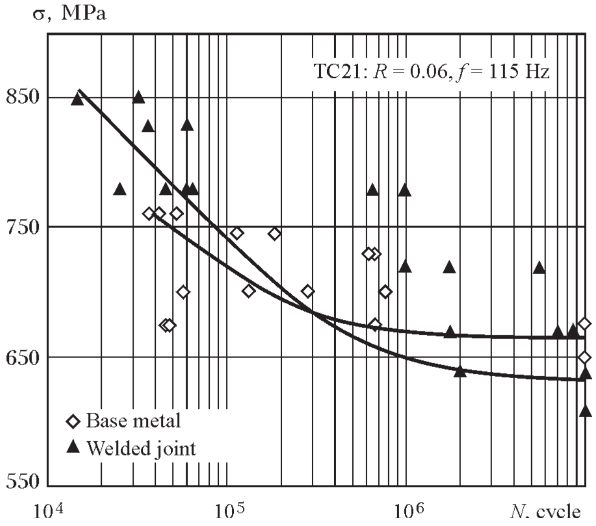

Figure 7. Fatigue test results and *S–N* curves for WB-welded joints and base metal

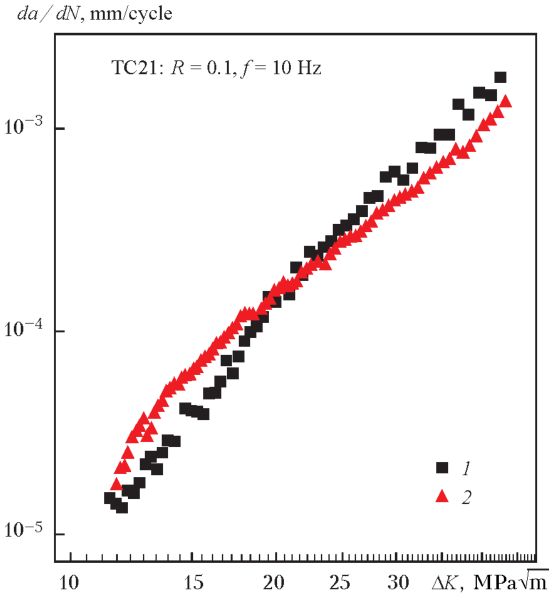

Figure 8. *da*/*dN*–Δ*K* curves for EB-welded joints (*1*) and base metal (*2*)

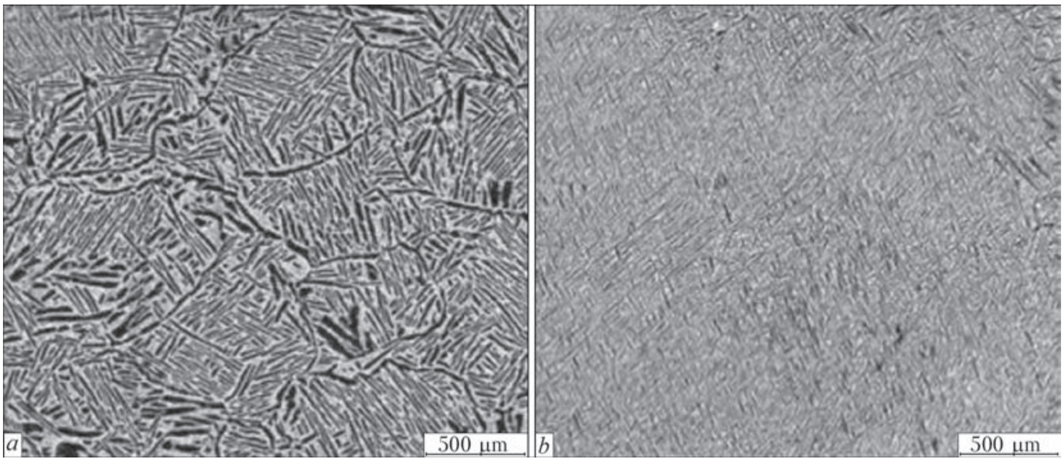

Figure 9. Microstructure of TC21 base (*a*) and weld (*b*) metal

titanium alloy at quasi-β forging and duplex annealing. Due to high heating and cooling rate, the weld metal mainly consists of coarse columnar dendritic prior β-grains, which were made up of numerous finer acicular α-martensite.

Compared with the base metal structure with relatively thick α-lamellar, the finer acicular α-martensite in the fusion zone possesses superior crack growth resistance at low $\Delta K < 21$ MPa·√m level, that is in good agreement with data of work [5]. At high ΔK, the thick α-lamellar and large grain boundary area in base metal can offer more resistance to fatigue crack growth. That is because of crack branching or crack deflection, at which secondary crack occurs easily at α-lamellar phase and grain boundaries. The crack growth path deflection changes the crack surface direction to the perpendicular direction of external force, that decreases the stress intensity factor at the crack tip and increases the length of the crack growth path. The crack branching or crack deflection as well as present of secondary crack made fracture surface more rough, and crack closure occurring at low loading increased the resistance to fatigue crack growth [6–8]. The difference in high cycle fatigue endurance and fracture toughness of the base metal and EB-welded joint can also be explained by the description above.

Conclusions

On the base of resuls obtained the following conclusions can be drawn from this study:

1. TC21 alloy is not sensitive to welding heat input and postweld cooling rates. The microstructure and mechanical properties of EB-welded joints can't be improved evidently by meliorating the welding parameters and welding line energy. The excellent mechanical properties of joints of TC21 alloy could be based on wide range of welding parameters.

2. The tensile strength of joint is equal to that of base metal. The damage-tolerant properties of the joint, such as fracture toughness and resistance to fatigue crack propagation, are excellent, and fatigue behavior of joints is comparable to that of base metal.

3. The basketweave structure of two-phase α + + β titanium alloys compensates for the ability to improve resistance to crack initiation or short crack growth, and deflects its propagation path at the grain boundaries, on the stage of macrocrack or long crack propagation obviously, that decreases the crack propagation rate and improves fracture toughness and fatigue strength. The extent of thickness of lamellar microstructure and the dimension of grains account for difference of crack growth rate between base metal and EB-welded joints.

1. Ji-kui Zhang, Xiao-quan Cheng, Zheng-neng Li (2010) Total fatigue life prediction for Ti-alloys airframe structure based on durability and damage-tolerant design concept. *Materials and Design*, **31**, 4329–4335.
2. Zhi-shou Zhu, Xin-nan Wang, Lu Tong et al. (2010) Research and application of damage tolerance titanium alloys for aeronautical use. *Materials China*, 29(**5**), 14–17.
3. Chun-xiao Cao (2002) Change of material selection criterion and development of high damage-tolerant titanium alloy. *Acta Metallurg. Sinica*, **38**, 4–11.
4. Schiller, S., Heisig, U., Panzer, S. (1982) *Electron beam technology*, 315–318. John Wiley Publ.
5. Xin-nan Wang, Zhi-shou Zhu, Lu Tong et al. (2008) The influence of forging processing on fatigue crack propagation rate of damage-tolerant titanium alloy. *Rare Metals Letters*, 27(**7**), 12–16.
6. Nakajima, K., Terao, K., Miyata, T. (1998) The effect of microstructure on fatigue crack propagation of α + β titanium alloys in-situ observation of short fatigue crack growth. *Materials Sci. and Eng. A*, 243(**1/2**), 176–181.
7. Xiong, Y., Hu, X.X. (2012) The effect of microstructures on fatigue crack growth in Q345 steel welded joint. *Fatigue & Fracture of Eng. Mater. & Structures*, 35(**6**), 500–512.
8. Leyens, C., Peters, M. (2003) *Titanium and titanium alloys*, 160–161. John Wiley Publ.

Received 26.11.2015

MECHANISMS OF FORMATION OF WELDING AEROSOL SOLID COMPONENT AND PATHS OF ITS PENETRATION INTO THE LIVING ORGANISM (Review)

I.P. GUBENYA and **I.R. YAVDOSHCHIN**
E.O. Paton Electric Welding Institute, NASU
11 Kazimir Malevich Str., 03680, Kiev, Ukraine. E-mail: office@paton.kiev.ua

The paper presents a review of current state of the issue of studying the mechanism of welding aerosol (WA) formation, dispersity of welding aerosol solid component and its ability to penetrate into the human body, as an important toxicological factor. It is established that there exist two main mechanisms of WA formation — due to condensation of high-temperature evaporation products and due to formation of volatile oxides on molten metal surface. Here, the molten metal drop is the main evaporation source, but weld pool and metal spatter also participate in the evaporation process. It is known that penetrability depends, chiefly, on dimensions of particles and their agglomerates: the smaller their size, the higher the penetrability. In addition to the already known paths of WA particle penetration into the body through the respiratory tract and digestive organs, nanosized particles can penetrate directly into the brain through nerve endings in the sinuses, as well as penetrate into the blood-vascular and lymphatic systems. This results in their accumulation in the bone marrow, lymph nodes, spleen and heart. Issue of searching for the methods to lower the emissions in coated-electrode welding is still urgent, chiefly due to improvement of their coating composition, as well as the ability to control particle dispersity in WA. 25 Ref., 1 Figure.

Keywords: *particle, welding aerosol, solid component, toxicity, penetrability, sanitary-hygienic characteristics*

Coated electrodes for manual arc welding (MAW) have for a long time been the object of investigations, which were initially aimed at improvement of welding-technological characteristics, while the next stage was lowering their production cost. At present, electrode sanitary-hygienic characteristics and searching for ways of reducing the negative influence of welding process on workers in this sector, are one of priority directions of electrode research.

As manganese is the main toxic component of welding aerosol (WA) in welding low-alloyed low-carbon steels, it was and still is one of the main objects of research [1]. This is confirmed by the Bulletin published by IIW, which actualizes the issue of WA investigation and gives several recommendations [2]:

- influence of WA and dust magnesium-containing compounds in welding and related technologies should be minimized, at least, within the respective national norms;
- it is worthwhile to perform further investigations to improve the understanding of absorption of these compounds (welding products); their behaviour in the human body; dose-effect interaction and any possible neurological and neurobehavioural manifestations.

On the other hand, American Conference of Governmental Industrial Hygienists (ACGIH) in 2013 revised their recommendations on manganese and proposed lowering the maximum allowable concentrations (MAC) of manganese: for WA solid component (WASC) with particle size below 2.5 μm — to 0.02 mg/m^3, and for WASC with more than 2.5 μm particle size — to 0.1 mg/m^3 [3]. Over the next several years, the above innovations can acquire the normative status that makes welding consumable manufacturers look for ways for adaptation to the new conditions. Such interest is due to the need to solve the questions concerning WASC adverse influence and consequences for the human body, as legal proceedings between welders, who acquired occupational diseases and welding consumable manufacturers are in progress in many countries, particularly, in the USA. The above data indicate that work aimed at improvement of sanitary-hygienic characteristics is carried on interstate level.

This paper analyzes published sources, concerning modern concepts of the mechanisms of WA formation and paths of their penetration into the human body.

MAW involves heating and melting of the electrode and base metal, and as metallic materials are a potential vapour source at heating, these processes of high-temperature heating are accompanied by evaporation of part of base metal and electrode material (1–3 % in coated-electrode welding) [4].

After melting, the molten metal passes the stages of drop and pool. It is believed that there exist three sources of WA formation [5]: molten drops, both present at the electrode tip and at the moment of their transition through the arc into the weld pool; weld pool; and spatter.

The drop is the main source of high-temperature vapour, as it is characterized by high specific surface (by an order of magnitude larger that that of the weld pool) and higher overheating level [6, 7]. Value of drop temperature at the moment of their detachment from electrode tip reaches 2500 K. Moreover, melt temperature in active spot zones is sometimes higher than boiling temperature. After the drop detachment from the electrode tip, its contribution into WA formation decreases [8]. At penetration of the formed vapour-gas mixture (the Figure) beyond the boundaries of the arc shielding atmosphere, intensive oxidation of some condensation products takes place under the influence of ambient oxygen. At cooling of the formed vapours, the condensation centers can be both the atoms of elements proper, and the finest metal drops, which are removed from the arc zone [1].

Work by Heile and Hill [9] gives two mechanisms of aerosol formation. The first consists in evaporation of electrode and base metal components, their subsequent condensation and oxidation. The second mechanism is formation of volatile oxides on molten metal surface in the case of oxygen penetration into the arc atmosphere. The contribution of each of these mechanisms depends on the welding process, composition and oxidizing potential of the arc atmosphere, at lowering of which the role of the second mechanism becomes smaller.

In the case of short-circuiting metal transfer and globular metal transfer, at the end of short-circuiting period, as well as at the moment of drop detachment from the electrode tip, breaking up and explosive evaporation of the formed bridge (neck) of metal between the electrode and base metal takes place, resulting in molten metal spatter. Rather fine spatter, which can remain suspended in the air flow, is called «microdrops». Technically, these microdrops are not aerosol, but all the WASC suspended in the air flow are assumed to be WA.

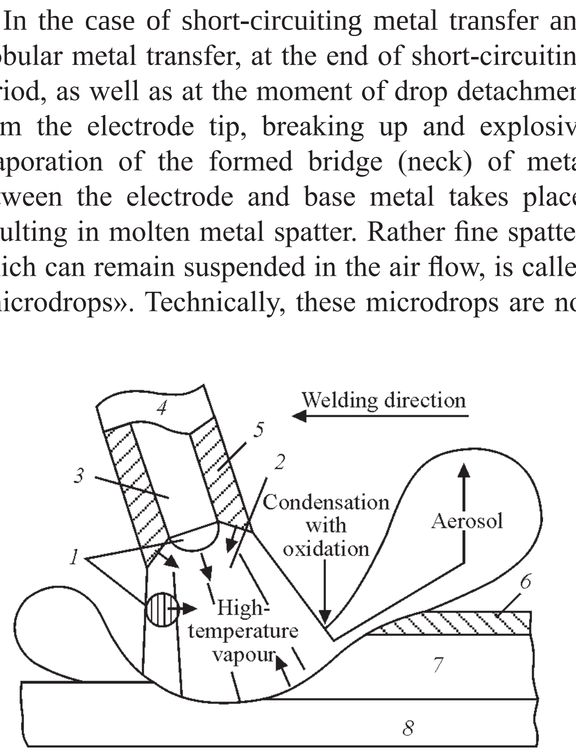

Mechanism of welding aerosol formation [1]: *1* — drop; *2* — arc; *3* — electrode rod; *4* — electrode; *5* — coating; *6* — slag; *7* — weld metal; *8* — base metal

Microdrops can also be an aerosol source, as penetrating into the ambient atmosphere, they intensively evaporate and oxidize that is accompanied by active evolution of aerosol [10, 11]. Contribution of the above mechanism decreases with reduction of the number of short-circuits, and change of the mode of molten metal transition through the arc.

By the nature of formation, WA belong to condensation aerosols, which are a dispersed system, where nanosized or micron (0.001–10 μm) solid particles — WASC, are the dispersed phase, and gas or a mixture of gases (WA gaseous component — (WAGC) are the dispersion medium. One of the important factors, determining WASC toxicity, is its dispersity. All the WA formed at any arc welding processes, without exception, are harmful to health. The difference is only in the degree of harmfulness and hazard for the welder that, in its turn, depends on WASC and WAGC composition, as well as on the level of effective concentrations and time of such influence [12].

WASC consists of particles of spherical and non-spherical form and their agglomerates. Most of the particles are of heterogeneous structure, consisting of the core and shell [10, 13]. The core consists mainly of iron and manganese compounds, and the shell contains silicon, potassium and sodium compounds. Coalescence of WASC particles (agglomeration and aggregation) results from the impact of electrostatic and adsorption forces. Considering the formation mechanism and size of particles, we can assume that electrostatic forces of interaction of WA particles are approximately the same in different materials. The force of adsorption interaction depends on the quantity of alkali elements (potassium, sodium and lithium) in WA. With increase of these elements content, the quantity of particles in agglomerates rises, and the size of agglomerate proper increases, accordingly. Partially sintered agglomerates, agglomerates with «open» structure, forming as a result of action of Van der Waals forces, adsorption forces of atmospheric moisture and electromagnetic forces, are observed, as well as agglomerates of nanosized particles in the form of chains [14–16].

Dimensions of individual particles and agglomerates vary from several nanometers to tens of micrometers [17–19]. About 70–80 % of particles of up to 0.1–2.0 μm diameter, penetrating into the body through respiratory organs, are removed when exhaling. Larger diameter particles are removed through expectoration [20].

WASC particles of 2.5–10 μm diameter are defined as those, which can penetrate inside the body with the flow of inhaled air – they usually penetrate into the bronchi. Particles of less than 2.5 μm diameter can not only penetrate inside the body, but also reach the finest recesses of the lungs – alveole, where the process of gas exchange with the nearest blood vessels proceeds. Penetrating into the alveole, the particles may dissolve and penetrate into the blood flow, as well as physically penetrate through vessel walls and be transported in the solid state by the blood. More over, they can diffuse into different parts of the respiratory tract, can be transported through epithelial and endothelial cells into the blood vascular and lymphatic systems, resulting in their accumulation in the bone marrow, lymph nodes, spleen and heart [21, 22]. Nanosized WASC can penetrate through the skin [22]. Particularly hazardous is the ability of nanosized particles to penetrate into the brain through nervous endings in the sinuses, overcoming the protective functions of the living organism [23–25]. For comparison: cell size is equal to 1–10 μm, that of viruses — 20–450 nm, and protein molecules — 5–50 nm [22].

Presented data from published sources demonstrate the mechanisms and sources of WA formation, main characteristics of WA particles and its hazard for human health. It is found that penetrability of WASC particles and agglomerates depends on their size: with decrease of the latter their penetrability into the body, either through the respiratory organs, or through the skin, increases. Particles in the nanorange are the most hazardous.

Proceeding from the above data, it is urgent to continue investigation of WASC properties, searching for ways to influence particle dispersity to increase their dimensions, and to lower their penetrability, accordingly, and at the same time, lower their toxic effect on the living organism, and improvement of electrode coating composition to reduce WA emissions.

1. Pokhodnya, I.K., Gorpenyuk, V.N., Milichenko, S.S. et al. (1990) *Metallurgy of arc welding: Processes in arc and melting of electrodes*. Ed. by I.K. Pokhodnya. Kiev: Naukova Dumka.
2. IIW statement on manganese. *https*://app.aws.org/technical/iiw-manganese.pdf
3. Clark, D. (2014) What the recent recommendation on manganese exposure means to you. *Welding J*., 93(**8**), 36–40.
4. Jenkins, N., Moreton, J., Oakley, P. et al. (1981) *Welding fume. Sources, characteristics, control*, Vol. 1–2, 269–329. Cambridge: Abington Hall.
5. Dennis, J.H., Hewitt, P.J., Redding, C.A.J. et al. (2001) A model for prediction of fume formation rate in gas metal arc welding (GMAW), globular and spray modes, DC electrode positive. *Ann. Occup. Hyg*., **45**, 105–113.
6. Erokhin, A.A. (1964) *Kinetics of metallurgical processes of arc welding*. Moscow: Mashinostroenie.
7. Kobayashi, M., Maki, S., Hashimoto, Y. et al. (1978) Some consideration about the formation mechanisms of welding fume. *Welding in the World*, 16(**11/12**), 238–245.
8. Leskov, G.I. (1970) *Electric welding arc*. Moscow: Mashinostroenie.
9. Heile, R., Hill, D. (1975) Particulate fume generation in arc welding processes. *Welding J*., **7**, 201–210.
10. Voitkevich, V. (1995) *Welding fumes: Formation properties and biological effects*. Cambridge: Abington Publ.
11. Jenkins, N.T., Pierce, W.M.G., Eagar, T.W. (2005) Particle size distribution of gas metal and flux cored arc welding fumes. *Welding J*., **84**, 156–163.
12. Sterjovski, Z., Drossier, J., de Thoisy, E. et al. (2006) An investigation of particulate weld fume generated from GMAW of plain carbon steel. *Austral. Welding J*., 51(1st quart.), 21–40.
13. Berlinger, B., Benker, N., Weinbruch, S. et al. (2010) Physicochemical characterization of different welding aerosols *Anal. Bioanal. Chemistry*, **10**, 1773–1780.
14. Zimmer, A.E., Biswas, P. (2001) Characterization of the aerosols resulting from arc welding processes. *Aerosol Sci*., **32**, 993–1008.
15. Zimmer, A.E. (2002) The influence of metallurgy on the formation of welding aerosols. *J. Envir. Monitoring*, **4**, 628–632.
16. Sterjovski, Z., Norrish, J., Monaghan, B.J. (2008) The effect of voltage and metal-transfer mode on particulate-fume size during the GMAW of plain-carbon steel: *IIW Doc. VIII-2092–08*.
17. Sowards, J.W., Lippold, J.C., Dickinson, D.W. et al. (2008) Characterization procedure for the analysis of arc welding fume. Pt 1. *Welding J*., 87(**4**), 76–83.
18. Sowards, J.W., Lippold, J.C., Dickinson, D.W. et al. (2008) Characterization of welding fume from SMAW electrodes. *Ibid*., **4**, 106–112.
19. Sowards, J.W., Lippold, J.C., Dickinson, D.W. et al. (2010) Characterization of welding fume from SMAW electrodes. Pt 2. *Ibid*., 89(**4**), 82–89.
20. Jankovic, J. (2005) Searching for a relationship between manganese and welding and Parkinson's disease. *Neurology*, **64**, 2021–2028.
21. Demetskaya, A.V., Kucheruk, T.K., Movchan, V.A. (2006) Particles of nanorange: Possible contribution to development of occupationally conditioned pathology. *Ukr. Zhurnal Probl. Med. Truda*, **1**, 62–67.
22. Hoet, P.H.M., Brueske-Hohlfeld, I., Salata, O.V. (2004) Nanoparticles — known and unknown health risks. *J. Nanobiotechnology*, 12 (**2**), 15.
23. Glushkova, A.V., Radilov, A.S., Rembovsky, V.R. (2007) Nanotechnologies and nanotoxicology: View of the problem. *Toksikolog. Vestnik*, **6**, 4–8.
24. Raloff, J. (2010) Destination brain. *Sci. News*, 177(**11**), 16–20.
25. Oberdoster, G., Zharp, Z., Atudorei, V. et al. (2004) Translocation of inhaled ultrafine particles to the brain. *Inhal. Toxicology*, **16**, 437–445.

Received 13.11.2015

VISIT OF DELEGATION OF POLAND INSTITUTE OF WELDING TO THE E.O. PATON ELECTRIC WELDING INSTITUTE

Delegation of Poland Institute of Welding (Instytut Spawalnictwa in Gliwice) consisting of A. Pietras, Director of the Institute, and E. Turyk, Deputy of Head of Welding Technology Department, visited the PWI in the period of November 18–20, 2015 on invitation of the Board of Directors. Aim of the visit was familiarization of management of Poland Institute of Welding with the directions of the PWI activities.

Several meetings were held in accordance with visit program.

Head of «Investigation of physical processes, technology and equipment for electron beam and laser welding» Department V.M. Nesterenkov, Corr. Member of the NASU, presented for Poland colleagues the directions of Department activity on manufacture of EBW equipment and developments of new EBW technologies; new 40 m^3 chamber for EBW and unique 100 m^3 chamber for EBW of new chambers were demonstrated. It was a presentation of technological operations on manufacture of all-welded outer part of body of front medium pressure chamber in gas turbine engine from casting titanium α-alloy VT5L, consisting of pillars and blades, using EBW method with computer-regulated technological process.

V.M. Lobanov, PWI Deputy Director, Academician of the NASU, highlighted the main directions of PWI activity in the field of welded structures optimizing as well as non-destructive testing and technical diagnostics of welded parts and structures. He also informed Poland colleagues on development of complex program of the NASU «Resource» directed on extension of safe life of the structures, constructions and machines. At the end, Prof. Lobanov arranged an excursion for the guests to PWI show-room.

In course of the meeting I.V. Krivtsun, PWI Deputy Director, Academician of the NASU, pointed out the issues of modelling of physical processes taking place in welding. The possibilities of increase of efficiency of hybrid processes of welding based on laser irradiation energy were discussed.

One more meeting was held with the Head of Department «Physical-chemical investigations of materials» G.M. Grigorenko, Academician of the NASU, during which it was possible to familiarize with different types of analytical equipment, in particular,

During signing of Agreement on cooperation (*from left to right:* L.M. Lobanov, B.E. Paton, A.T. Zelnichenko and A. Pietras)

Discussion of possibilities of tool for high-frequency mechanical peening (*from left to right:* E. Turyk, A. Pietras and V.V. Knysh)

Gleeble 380 (DSI) unit, optical spectrometer (ICP-Spectrometer) with inductively coupled plasma iCAP 6500 DUO (Thermo Fisher Scientific), Auge-microprobe with field emission cathode JAMP-9500F (JEOL).

Head of Department «Special high-voltage equipment and laser welding» Dr. V.D. Shelyagin presented the guests with Department capabilities in the field of laser welding technologies, in particular, provided detailed description of manual laser tool, developed in PWI, for welding in railway transport.

PWI unique equipment for mechanical tests, including press MP-800 and tool for high-frequency mechanical peening of welded joints, was demonstrated in «Strength of welded structures» Department (Head — Prof. V.V. Knysh).

Also, a meeting was held with Head of Department of V.N. Bakul Institute for Superhard Materials A.L. Majstrenko, Corr. Member of the NASU. The issues related with improvement of friction stir welding technology and manufacture of specialized instruments were discussed in the course of meeting.

Director of the International Association «Welding» Dr. A.T. Zelnichenko familiarized Poland guests with the main directions of the PWI publishing activity and Conference plans for 2016, which are organized by PWI.

The final meeting with PWI Director, Academician Boris E. Paton took place on November 20. It covered the issues of cooperation between the Institutes. Poland experience on training of welders was discussed in details. The final point of the meeting was signing of Agreement on scientific-and-technical cooperation between the E.O. Paton Electric Welding Institute and Poland Institute of Welding.

Dr. A.T. Zelnichenko, PWI

In show-room of PWI (*from left to right:* L.M. Lobanov, E. Turyk and A. Pietras)

Against electron beam chamber (*from left to right:* E. Turyk, V.M. Nesterenkov and A. Pietras)

PATON PUBLISHING HOUSE

www.patonpublishinghouse.com

SUBSCRIPTION

«The Paton Welding Journal» is Published Monthly Since 2000 in English, ISSN 0957-798X.

«Avtomaticheskaya Svarka» Journal (Automatic Welding) is Published Monthly Since 1948 in Russian, ISSN 005-111X.

«The Paton Welding Journal» is Cover-to-Cover Translation of Avtomaticheskaya Svarka» Journal into English.

If You are interested in making subscription directly via Editorial Board, fill, please, the coupon and send application by Fax or E-mail.

The cost of annual subscription via Editorial Board is $348 for «The Paton Welding Journal» and $180 for «Avtomaticheskaya Svarka» Journal.

«The Paton Welding Journal» can be also subscribed worldwide from catalogues subscription agency EBSO.

SUBSCRIPTION COUPON
Address for journal delivery ____________________
____
Term of subscription since ______ 20 ______ till ______ 20 ______
Name, initials ____________________
Affiliation ____________________
Position ____________________
Tel., Fax, E-mail

We offer the subscription all issues of the Journal in pdf format, starting from 2009.

The archives for 2009–2014 are free of charge on *www.patonpublishinghouse.com* site.

ADVERTISEMENT

in «Avtomaticheskaya Svarka» and «The Paton Welding Journal»

External cover, fully-colored:
First page of cover (190×190 mm) — $700
Second page of cover (200×290 mm) — $550
Third page of cover (200×290 mm) — $500
Fourth page of cover (200×290 mm) — $600

Internal cover, fully-colored:
First/second/third/fourth page of cover (200×290 mm) — $400

Internal insert:
Fully-colored (200×290 mm) — $340
Fully-colored (double page A3) (400×290 mm) — $500

- Article in the form of advertising is 50 % of the cost of advertising area
- When the sum of advertising contracts exceeds $1001, a flexible system of discounts is envisaged

Size of journal after cutting is 200×290 mm

Editorial Board of Journal «Avtomaticheskaya Svarka» and «The Paton Welding Journal»
E.O. Paton Electric Welding Institute of the NAS of Ukraine
International Association «Welding»
11 Kazimir Malevich Str. (former Bozhenko Str.), 03680, Kiev, Ukraine
Tel.: (38044) 200 60 16, 200 82 77; Fax: (38044) 200 82 77, 200 81 45
E-mail: journal@paton.kiev.ua; www.patonpublishinghouse.com